Microparticles Focusing Inside Rigid Zigzag Microchannels and Application to Bacteria Enrichment

Ahmed Refaei

A THESIS SUBMITTED TO
THE FACULTY OF GRADUATE STUDIES
IN PARTIAL FULFILLMENT OF THE REQUIREMENTS
FOR THE DEGREE OF MASTER OF APPLIED SCIENCE

GRADUATE PROGRAM IN MECHANICAL ENGINEERING
YORK UNIVERSITY
TORONTO, ONTARIO

Abstract

Sample preparation is vital for biomedical diagnostics, environmental monitoring, and food safety, with enrichment of microparticles and microorganisms essential for reliable detection. Label-free microfluidic enrichment offers a portable alternative to centrifugation and filtration, which require bulky equipment or external forces. Passive inertial microfluidics, particularly zigzag microchannels, enable efficient, high-throughput particle manipulation through Dean flow. However, knowledge gaps remain in understanding micrometer-sized behavior in rigid zigzag channels, evaluating design parameters, and predicting Dean drag velocity and force. This thesis systematically investigates rigid zigzag microchannels for focusing and enrichment. Objective 1 compared rigid (PMMA) and soft (PDMS) devices using microparticles (1-3.9 μm) and *E. coli* bacteria, showing superior focusing in rigid channels. Objective 2 employed COMSOL Multiphysics and Taguchi DOE to optimize geometry, achieving > 80% focusing efficiency. Objective 3 demonstrated enrichment of GFP-labeled *E. coli* with factors of 2.6 and 8 after one and two passes while preserving ~84% viability. This work establishes a robust, biocompatible platform with strong potential for portable diagnostics.

Dedication

To my family, whose love, sacrifices, and unwavering belief in me have shaped every step of this journey and to my beloved fiancée and her wonderful family, thank you for your endless encouragement and kindness. Your presence has brought warmth and purpose to this path. Your strength has been my anchor, and your support, my greatest motivation.

Acknowledgments

First and foremost, I would like to express my earnest gratitude to my supervisor Prof. Pouya Rezai for giving me the opportunity to study at York University and his guidance and patience throughout my MSc studies.

I would like to express my sincere gratitude to Prof. Reza Rizvi for his valuable support and advice during my annual committee meetings and for serving as the Chair of my defense committee. I also extend my thanks to Dr. Rashid Bashir for his insightful feedback and participation as a member of my defense committee.

I am deeply thankful to my colleagues at York University for their continuous support, encouragement, and guidance throughout my MSc studies. My appreciation extends to all the talented and dedicated members of the Advanced Center for Microfluidics Technology and Engineering (ACμTE) lab for their collaboration, insightful discussions, and camaraderie, which greatly enriched my research experience. A special acknowledgment goes to Dr. Arsalan Nikdoost, for his assistance during the early stages of my master's program.

Table of content

ABSTRACT II

DEDICATION III

ACKNOWLEDGMENTS IV

LIST OF TABLES VIII

LIST OF FIGURES IX

ABBREVIATIONS XV

GLOSSARY OF TERMS XVI

1. CHAPTER 1: INTRODUCTION 1

1.1. Introduction and Research Motivation 1

1.2. Research Opportunity and Thesis Objectives 6

1.2.1. Thesis Goals and Objectives 9

1.3. Thesis Organization 11

1.4. Research Contributions 12

2. CHAPTER 2: LITERATURE REVIEW 13

2.1. Conventional Methods for Particle Manipulation and Enrichment 13

2.2. Microfluidic Methods for Particle Manipulation and Enrichment 15

2.2.1. Active Microfluidic Methods 15

2.2.2. Passive Microfluidic Methods 16

2.2.2.1. Experimental Techniques in Microfluidics Microparticle Focusing 16

2.2.2.2. Numerical Techniques in Microfluidics Microparticle Focusing 33

3. CHAPTER 3: MATERIALS AND METHODS 39
3.1. Materials and sample preparation 40
3.2. Design and fabrication of microfluidic devices 41
3.3. Experimental setup and procedures 43
3.3.1. Experimental setup and procedure 43
3.3.2. Quantification of E. coli concentration 43
3.3.3. Establishment of a calibration curve for E. coli GFP 44
3.4. Data analysis 45
3.5. Numerical model and governing equations 47
3.5.1. Fluid flow simulation 48
3.5.2. Particle tracing simulation 48
3.5.3. Boundary conditions 49
3.5.4. Design of experiments 50
4. CHAPTER 4: MICROPARTICLES FOCUSING INSIDE RIGID ZIGZAG MICROCHANNELS 52
4.1. Characterization of hot embossed zigzag microchannels 53
4.2. Effect of channel rigidity on particle focusing in zigzag channels 54
4.3. Effect of particle size to mimic E. coli bacteria focusing behavior 56
4.4. Numerical modelling and particle focusing optimization 57
4.4.1. Mesh independency study 58
4.4.2. Model validation 59
4.4.3. Parametric numerical study on microparticle focusing in zigzag channel 61
4.4.3.1. Effect of number of zigzags (N_z) and zigzag length (L_z) 62
4.4.3.2. Effect of zigzag angle (θ_z) 63

4.4.3.3. Effect of channel width (w) 66

4.4.3.4. Effect of axial velocity (V_x) 67

4.5. Proof of concept E. coli focusing using the optimum device 68

5. CHAPTER 5: ESCHERICHIA COLI ENRICHMENT USING INERTIAL FOCUSING IN RIGID ZIGZAG MICROCHANNELS 71

5.1. Effect of flow rate on particle focusing 72

5.2. Enrichment of particles and E. coli 74

5.3. Effect of bacteria concentration on enrichment 75

5.4. Viability of E. coli after enrichment 77

6. CHAPTER 6: THESIS SUMMARY AND FUTURE WORK 80

6.1. Thesis summary 80

6.2. Thesis limitations and proposed future work 83

REFERENCES 86

List of Tables

Table 3-1 List of materials used and their procurement sources..... 40

Table 3-2 Parameter levels selected for the design of experiments using Taguchi model..... 50

Table 3-3 All the conducted simulations based on Taguchi model..... 51

List of Figures

Figure 1-1 Focusing of 2 μm and 920 nm particles in serpentine channels. The left panel indicates the relative particle sizes along with their associated fluorescence colors. The middle panel displays merged fluorescence images of 2 μm and 920 nm particles tested simultaneously in the same microchannel under identical flow conditions. The right panel shows the fluorescent intensity across the channel width. Channel cross section 20 × 10 μm^2. [13]..... 3
Figure 1-2 Comparison of different channel geometries operated across flow rates ranging from 100 to 500 μL/min. [17] Permission obtained from RSC. 5
Figure 2-1 Demonstration of equilibrium positions in a straight microchannel with (A) circular, (B) square, and (C) rectangular cross section with AR=0.5. (D) The lateral migration speed UL and minimum channel length for particle focusing $Lmin$. [46] Permission obtained from RSC. 17
Figure 2-2 Amplification of inertial focusing for particle separation. (A) Schematic of a straight microchannel with one inlet and three outlets. (B) Larger particles experience inertial lift forces, causing differential migration toward equilibrium positions. (C, D) Top and cross-sectional views show how channel expansion drives red blood cells (RBCs) toward the channel walls. (E) RBCs are collected through the side outlets. [48] Permission obtained from Biotechnology and Bioengineering. 19
Figure 2-3 Particle focusing in low aspect ratio microchannels. (a) In rectangular microchannels with low aspect ratio (b) Triangular microchannels with low aspect ratio exhibit a compressed, asymmetric velocity profile, concentrating particles near the apex. (c, d) Fluorescence images showing top and side views of 15 μm particles focusing in 100 μm × 40 μm rectangular and triangular channels, respectively. [49] Permission obtained from RSC. 20
Figure 2-4 Curved microchannels under inertial flow conditions, the faster-moving fluid at the center tends to maintain its outward trajectory due to momentum. To conserve mass, the slower-moving fluid near the channel walls circulates inward, resulting in the formation of two counter-rotating vortices perpendicular to the main flow direction. [18] Permission obtained from RSC. 21
Figure 2-5 Channel Reynolds number (Re_C) maps for each condition of curvature and particle confinement. [53] 23

Figure 2-6 Schematic illustration of the microparticle focusing device. (a) Particles are initially distributed randomly at the inlet. (b) As they progress, they converge into a focused stream at the AA′ cross-section within the transition region. (c) Enlarged views of (i) the transition region and (ii) the outlet region is shown, with channel dimensions $R_1 = 800$ μm, $R_2 = 1150$ μm, and length $L = 9.75$ mm. (d) A diagram illustrating the directions of dominant forces acting on particles at various positions within the channel. [54] 24
Figure 2-7 (a) Schematic of the microfluidic chip for isolating circulating tumor cells (CTCs) from white blood cells. (b) Close up view of the curvilinear microchannel with dimensions. [55] 26
Figure 2-8 Design and operation of serpentine microfluidic channel for focusing 2 μm red fluorescent particles. (a) Top view schematic of the full inertial focusing device, featuring a 4.5 cm-long serpentine section. (b) Enlarged view of the serpentine curved channel and (b′) corresponding fluorescence image showing focused particle streams. (c) Magnified image of a single serpentine unit with channel widths of 20 μm (small bend) and 80 μm (large bend), and (c′) fluorescence image confirming particle focusing at this location. (d) Close-up of the isolation region and (d′) its corresponding fluorescence image showing focused 2 μm particles. White dashed lines denote microchannel boundaries. [13]..... 27
Figure 2-9 An overview of the z-rise device: (A) the z-rise inertial microfluidic channel is depicted on a macroscopic scale. (B) detailed view of the z-rise channel. (C) from a lagrangian perspective, the zigzag microchannel comprises a series of straight microchannels with a distinctive cross-section expansion. [17] Permission obtained from RSC. 29
Figure 2-10 (A) Effect of channel rigidity on 3 μm particles' focusing. (B) Comparison between various channel geometry at flow rates from 100 μL/min to 500 μL/min. [17] Permission obtained from RSC. 31
Figure 2-11 Evaluation of bacterial separation using the zigzag microfluidic channel. (A) Separation efficiency of epithelial cells and E. coli. (B) At a flow rate of 150 μL/min, epithelial cells and debris focused at the central outlet, while E. coli remained dispersed across the channel. [11] Permission obtained from RSC. 31
Figure 2-12 Schematic representation of the experimental setup and triangular microchannel design for inertial cell separation. (A) Illustration of introducing a mixture of circulating tumor cells (CTCs) and white blood cells (WBCs) into the triangular microchannel. (B) Schematic of the key forces acting on cells at the triangular bends, including wall-induced lift forces, shear forces,

centrifugal forces, and Dean drag. (C) 3D view of the triangular microchannel featuring vertex angles of 30° and 60°, and (D) cross-sectional geometry with a channel width of 200 µm, height of 100 µm, and variable curvature radius (R) ranging from 100 to 400 µm. [68] permission obtained from Elsevier. 35
Figure 2-13 Schematic diagrams of the three curved channels. (a) top view of the three curved channels and (b) unit structure of the three curved channels. [69] 36
Figure 2-14 Numerical simulations and particle trajectories in zigzag channels. (A) Velocity contours show shifting flow patterns. (B) Lift- and drag-dominated regions are marked, with reference points A, B, and C; lateral flow appears at bends due to channel curvature and inertia. (C) Particle trajectories reveal that small particles focus near the sidewalls. [17] Permission obtained from RSC. 37
Figure 3-1 Fabrication and assembly of the zigzag microfluidic device. (A) Hot embossing fabrication process consisting of three steps: (1) Controlled pressure and temperature is applied between the silicon wafer master mold and the PMMA substrate for 5 minutes. (2) Applied pressure is released at T = 80°C. (3) The embossed PMMA substrate is demolded. (B) The assembled microfluidic device comprises three layers: the PMMA sheet with an embossed microchannel, an adhesive bonding layer, and a flat PMMA substrate. It includes a single inlet, a zigzag channel, a single outlet, and an expansion zone for particle imaging. 41
Figure 3-2 Calibration curve of E. coli concentration based on fluorescence GFP intensity measurements using a fluorometer plotted against the actual bacterial concentrations measure via plate counting. Each data point represents the mean of fifteen replicates of three cultures, with error bars indicating the standard deviation. Significance thresholds were determined using p-values, with a threshold set at 0.05 to define statistical significance. Statistical significance is indicated by asterisks where * denotes $p < 0.05$, ** denotes $p < 0.01$, *** denotes $p < 0.001$, **** denotes $p < 0.0001$, and 'ns' indicated non- significant differences. 45
Figure 3-3 Methods used for analyzing particles distribution in microfluidic channels. Image overlaps show particles trajectory and distribution across the expansion channel width for 3.9 µm particles at V_x of (A) 0.07 m s^{-1} and (B) 0.37 m s^{-1} in a rigid zigzag microchannel. The microchannels featured $L_z = 2$ mm, $\theta_z = 60°$, $N_z = 20$ units, $w = 45$ µm, and $h = 25$ µm. Normalized number of particles (NNP) were drawn versus the normalized channel width. FWMH indicates the

full width at half maximum, representing the particles' distribution. PC shows the peak of centroid, representing the location of the highest particles concentration. 46
Figure 3-4 Schematic diagram of the simulated microfluidic channels with 3.9 μm particles being focused at the channel center. The simulated microchannel featured L_z = 2 mm, θ_z = 60°, N_z = 20 units, w = 45 μm, and h = 25 μm. 48
Figure 4-1 Characterization of the hot-embossed zigzag microchannels. Profilometer analysis at a zigzag channel corner at 10x magnification, with the color map indicating surface height variations for (A) the rigid zigzag channel and (B) the mold. Optical images at 5x magnification of (C) the hot-embossed microchannel and (D) the mold. 54
Figure 4-2 Effect of channel rigidity on particles distribution. The NNP is plotted alongside the normalized channel width for 1 μm particles in (A) a rigid PMMA zigzag channel and (B) a soft PDMS zigzag channel, under axial velocities of V_x = 0.07, 0.22, and 0.37 m s^{-1}. Both microchannels featured L_z = 2 mm, θ_z = 60°, N_z = 20 units, w = 45 μm, and h = 25 μm. 55
Figure 4-3 Effect of particle size on particles distribution in a rigid zigzag channel. The NNP is plotted alongside the normalized channel width at V_x = 0.37 m s^{-1} for E. coli, 1 μm, 2.7 μm, and 3.9 μm particles. The used microchannel in these experiments featured L_z = 2 mm, θ_z = 60°, N_z = 20 units, w = 45 μm, and h = 25 μm. 56
Figure 4-4 Numerical simulation of water flow in a zigzag microchannel. (A) Schematic illustration showing the selected cross-sectional planes for model verification. Axial velocity profile at the middle of the channel cross section at an inlet average velocity of 0.74 m s^{-1} of (B) Section A, (C) Section B, and (D) Section C. The simulated microchannel featured L_z = 2 mm, θ_z = 60°, N_z = 20 units, w = 45 μm, and h = 25 μm. 59
Figure 4-5 Comparison of the experimental and numerical results for model validation. (A) 1 μm particles at V_x = 0.07 m s^{-1} (dispersed). (B) 1 μm particles at 0.37 m s^{-1} (partially focused). (C) 2.7 μm particles at 0.37 m s^{-1} (fully focused). (D) 3.9 μm particles at 0.37 m s^{-1} (fully focused). The simulated microchannel in (A-D) featured L_z = 2 mm, θ_z = 60°, N_z = 20 units, w = 45 μm, and h = 25 μm. 60
Figure 4-6 Results of the Taguchi parametric study showing the mean focusing efficiency versus (A) number of zigzags (N_z), (B) zigzag length (L_z), (C) zigzag angle (θ_z), (D) channel width (w), and (E) axial velocity (V_x). 61

Figure 4-7 Focusing behavior of 1 μm particles along the zigzag channel length. (A) Dispersed distribution. (B) Two focusing streams. (C) Partial focusing behavior. (D) Fully Focusing behavior. The simulated zigzag channel featured L_z = 3 mm, θ_z = 60°, N_z = 30 units, w = 40 μm, and h = 20 μm. 63
Figure 4-8 Velocity contours and velocity vectors for different angles at V_x = 0.37 m s^{-1}. The simulated microchannel featured θ_z = 60°, w = 40 μm, and h = 20 μm. 64
Figure 4-9 Dean drag velocity analysis under various conditions. (A) Velocity profile plotted for different zigzag angles at an inlet axial velocity of 0.37 m s^{-1} in a zigzag channel with a cross-section of w × h = 40 × 20 μm^2. (B) Average Dean drag velocity versus zigzag angle at V_x = 0.37 m s^{-1}, in a zigzag channel with a cross-section of w × h = 40 × 20 μm^2. (C) Average Dean drag velocity versus channel width at V_x = 0.37 m s^{-1}, with a fixed θ_z = 60° and h = 20 μm. (D) Average Dean drag velocity versus axial velocity, using a zigzag channel with θ_z = 60° and a cross-section of w × h = 40 × 20 μm^2..... 65
Figure 4-10 A schematic illustration of equilibrium positions of 1 μm particles, with the acting forces shown for (A) moderate axial velocities and (B) high axial velocities. 67
Figure 4-11 Experimental validation of E. coli focusing in the optimized channel (A) Overlapped images of E. coli trajectory at the channel expansion zone in the optimized channel at V_x = 0.37 m s^{-1} (B) Distribution of E. coli across the channel width before and after optimization, compared with the numerical results. The zigzag channel featured L_z = 3 mm, θ_z = 60°, N_z = 30 units, w = 40 μm, and h = 20 μm. 69
Figure 5-1 The assembled microfluidic device comprises three layers: a PMMA sheet with an embossed microchannel, an adhesive bonding layer, and a PMMA substrate. The device included a single inlet, three outlets, and an expansion zone for particle imaging. The optimized channel featured L_z = 3 mm, θ_z = 60°, N_z = 30 units, w = 40 μm, and h = 20 μm. 72
Figure 5-2 Effect of flow rate on the NNP alongside the normalized channel width for 1 μm particles in rigid zigzag channels. 73
Figure 5-3 Enrichment of 1 μm particles and E. coli in rigid zigzag microchannels. (A) Distribution of 1 μm particles and E. coli bacteria across the channel width at Q = 50 μL/min. Trajectories and outlet samples fluorescent images of (B-D) 1 μm particles and (E-G) E. coli in zigzag microchannels at Q = 50 μL/min. 75

Figure 5-4 Enrichment factor of E. coli at various inlet concentrations. Error bars are standard deviations. *: $p < 0.05$, ns: not significant. 76
Figure 5-5. Number of viable E. coli cells after enrichment for the source, control, and enriched samples. 78

Abbreviations

E. coli: *Escherichia coli*

S. aureus: *Staphylococcus aureus*

3D: Three-dimensional

DI Water: Deionized water

FWHM: Full width at half maximum

NNP: Normalized number of particles

PC: Peak of centroid

PDMS: Poly[dimethyl siloxane]

PMMA: Polymethyl methacrylate

RoI: Region of interest

GFP: Green fluorescent protein

LB: Luria Broth

CFU: Colony forming unit

UV: Ultraviolet

DOE: Design of experiments

VDZ: Velocity dead zone

PoC: Point of care

Glossary of Terms

Enrichment: The process of increasing the relative concentration of a specific target.

Microfluidics: The technology to manipulate fluids in channels with tens of micrometer in size.

Lab-on-a-chip: A microdevice, which integrates different laboratory functions on a single integrated circuit with a size up to few square centimeters.

Dielectrophoresis: The movement of neutral particles when subjected to a non-uniform electric field.

Magnetophoresis: This method utilizes the magnetic field gradients to apply a force to particles or cells with magnetic susceptibilities different from the carrying fluid.

Acoustophoresis: Migration of particles under the effect of acoustic force exerted by ultrasound waves.

Dean flow: Secondary fluid movement in lateral direction due to the channel curvature.

Blockage ratio: The ratio of particle diameter to the channel hydraulic diameter.

Chapter 1: Introduction

1.1. Introduction and Research Motivation

Microscale particles and microorganisms are commonly present in a wide range of liquid suspensions, from water sources and food matrices to biological fluids [1]. Timely sample preparation, detection, and identification of micro-scale particles and organisms are crucial in various fields including medical diagnostics, environmental monitoring, food safety, and biotechnological applications [1]. For example, microplastics have increasingly become a pressing environmental issue because of their widespread occurrence and harmful effects on ecosystems and human well-being [2]. Similarly, pathogenic bacteria such as *Escherichia coli (E. coli)*, *Salmonella,* and *Staphylococcus aureus (S. aureus)* pose significant risks to human health, potentially causing severe diseases and outbreaks [3], [4].

Among various essential sample preparation steps, the enrichment (concentration enhancement) of microparticles and target bacteria is crucial to meet the limit of detection of various detection methods [5]. The enrichment factor and cell viability can be defined as follows:

$$Enrichment\ Factor\ = \frac{Device\ outlet\ concentration}{Device\ inlet\ concentration} \qquad (1-1)$$

$$Viability\ (\%) = \frac{\#\ of\ viable\ bacteria\ in\ outlet}{\#of\ viable\ bacteria\ in\ inlet} \times 100 \qquad (1-2)$$

Conventional methods for enrichment include filtration, centrifugation, enrichment broths, and immunomagnetic separation, each with their own advantages and limitations [6], [7], [8], [9]. Filtration can suffer from clogging and may not differentiate microorganisms or microparticles from each other [6]. Centrifugation requires special equipment and may be inefficient for low concentrations [7]. Enrichment broths enhance growth but may also support other microbes [8]. Immunomagnetic separation is costly and may need optimization [9].

Considering the shortcomings of conventional enrichment methods, researchers have innovated and implemented novel enrichment methods using particle manipulation in microfluidics [10], [11]. Particle manipulation is a fundamental technique that involves examining the flow dynamics and alignment of particles within a fluid stream in a microchannel. It enables precise analysis and separation [12] of particles through the use of various physical forces and phenomena to streamline particles at specific locations in the channel, called particle focusing in the field. For example, Fig. 1-1 shows the distribution of 2 μm (red) and 920 nm (green) particles at the channel outlet in a serpentine channel with a channel cross section of 20 × 10 μm^2 at a flow rate of 80 μL/min [13].

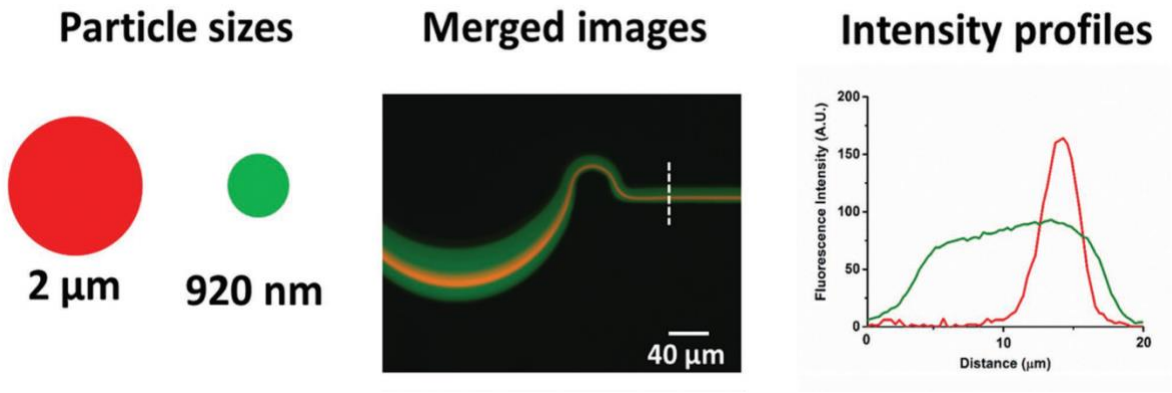

Figure 1-1 Focusing of 2 µm and 920 nm particles in serpentine channels. The left panel indicates the relative particle sizes along with their associated fluorescence colors. The middle panel displays merged fluorescence images of 2 µm and 920 nm particles tested simultaneously in the same microchannel under identical flow conditions. The right panel shows the fluorescent intensity across the channel width. Channel cross section 20 × 10 μm^2. [13]

The merged fluorescence images and intensity profiles show that the larger 2 µm particles focus more tightly near the channel centerline (fully focused), while the smaller 920 nm particles remain more broadly distributed across the channel width (dispersed). Particle focusing technique is crucial for various sorting and enrichment applications, including biomedical diagnostics and environmental monitoring [14].

Particle handling methods in microfluidics are generally categorized into active and passive techniques. Active methods depend on external forces such as electric (electrophoresis), acoustic (acoustophoresis), or magnetic (magnetophoresis) forces to manipulate particles. These techniques collectively advance the capabilities of microfluidic devices in enrichment, enhancing their applications in clinical diagnostics and environmental monitoring; however, they come with several limitations [15]. These techniques often involve expensive components, required to generate external electromagnetic fields, acoustic waves, or optical signals, which can result in higher cost, power consumption, and heat generation [15]. Additionally, they need to be calibrated

and serviced, which demands specialized knowledge that might not always be available at hand [16].

Passive methods rely on inherent microchannel design and fluid properties, and they are favoured by researchers due to their simplicity, cost-effectiveness, and compatibility with standard fabrication techniques. These methods offer a straightforward approach to achieving precise particle or cell alignment within microchannels [17]. Additionally, they provide stable and continuous operation, making them suitable for long-term experiments or applications where precise control is not essential [18]. The focusing efficiency can be defined as follows [19]:

$$Focsuing\ Efficieny = \frac{Number\ of\ particles\ located\ within\ 20\%\ of\ the\ channel\ center}{Total\ number\ of\ particles\ across\ the\ width\ of\ the\ channel} \times 100 \quad (1-3)$$

Traditionally, straight microchannels have been widely used for inertial focusing due to their simplicity and ease of fabrication [18]. However, they often suffer from limitations such as multiple equilibrium positions, low focusing efficiency for small particles, and the need for long channel lengths to achieve stable focusing [14].

To address the limitations above, researchers have explored curved microchannels. The introduction of curvature induces secondary Dean flows, which interact with inertial lift forces to enhance particle migration [20]. These Dean vortices help particles reach stable positions more rapidly than in straight channels by balancing the inertial lift force with the Dean drag force. Nevertheless, the performance of curved channels remains sensitive to flow conditions and particle size, and achieving efficient focusing for small particles still presents challenges. To further improve focusing performance, channel designs with complex

repeated patterns such as square-wave, serpentine, and zigzag channels were developed. These geometries generate alternating Dean vortices that periodically reverse direction, resulting in enhanced focusing efficiency [21]. This mechanism enables particles to achieve tighter focusing with shorter channel lengths.

In general, zigzag channels with sharp corners outperform other designs such as curvilinear, asymmetric curvilinear, rounded corner zigzag, and square wave patterns in terms of particle focusing and separation capabilities [17]. The distinct advantage of the zigzag channel design stems from its abrupt changes in cross-section at each zigzag corner, which promote stronger dean flow than those observed in curvilinear or square-wave channels [17]. For instance, Bazaz et al. [17] compared different serpentine geometries (Fig 1-2), including symmetric and asymmetric curvilinear, square-wave, zigzag with rounded corners, and zigzag with sharp corners. Among these, only the rigid zigzag channel with sharp corners successfully focused 3 µm particles across the entire range of tested flow rates, discussed in depth in chapter 2.

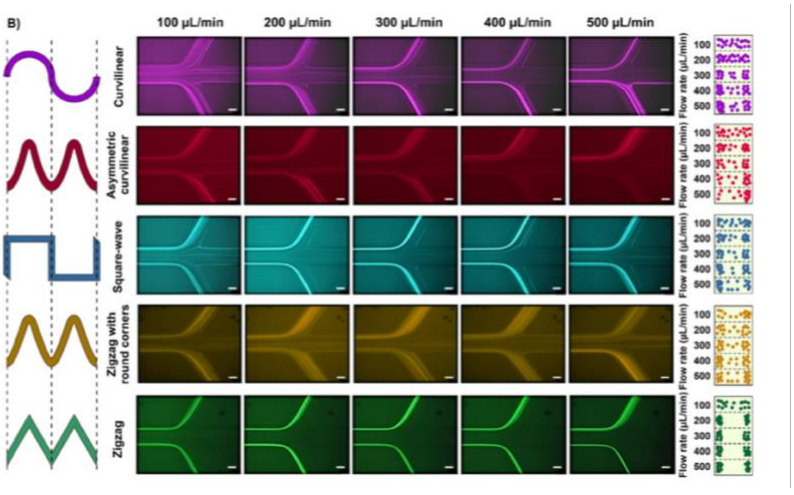

Figure 1-2 Comparison of different channel geometries operated across flow rates ranging from 100 to 500 µL/min. [17] Permission obtained from RSC.

In parallel with experimental advancements, computational studies have provided valuable insights into the physics of particle migration [22], enabling a more comprehensive and intuitive understanding of particle migration in different geometries such as straight [23], [24], spiral [25], sinusoidal [26] and square wave channels [27], and other geometries [28].

In general, previous research on microparticle focusing in various geometries, including zigzag channels, has mainly targeted microorganisms [25], [26] and microparticles [27] larger than 1 μm. Furthermore, efficient focusing of 1 μm particles and bacteria such as *E. coli, Salmonella,* and *S. aureus* remain challenging in zigzag microchannels. Importantly, the existing literature has primarily investigated the focusing efficiency of zigzag channels, without developing a fundamental understanding of the zigzag channel parameters that govern particle migration for particles around 1 μm or smaller. For instance, Bazaz et al. [16] utilized rigid zigzag microchannels to focus microparticles with diameters ranging from 20 μm to 7 μm efficiently; however, they were unable to achieve focusing for smaller particles of 5 μm and 3 μm, further elaborated on in chapter 2. In another study, Shrestha et al. [11] proposed a zigzag microfluidic channel to isolate particles and cells. Their device showed size-based differential focusing to separate 3 μm particles from 1 μm particles, as well as bacteria from epithelial cells and debris; however, the reported separation efficiency for 1 μm particles and *E. coli* was limited to ~ 50% after the first run and ~ 70% after two processing runs, discussed in depth in chapter 2.

1.2. Research Opportunity and Thesis Objectives

A comprehensive review of the literature reveals significant progress in microparticle manipulation using microfluidic platforms. However, several critical gaps remain,

particularly in the context of rigid zigzag microchannels and micrometer-sized particles behavior, that limit both fundamental understanding and practical implementation.

1. **Limited understanding of micrometer-sized particles behavior in rigid zigzag microchannels**

Most existing studies have focused on microparticles larger than 1 μm, with minimal exploration of the migration and focusing behavior of micrometer-sized particles and bacteria in zigzag geometries. This knowledge gap is especially important given the increasing interest in manipulating smaller biological and synthetic particles for biomedical and environmental applications. Additionally, addressing this gap is essential to extend the applicability of inertial microfluidics to nanometer targets, which behave differently due to the growing influence of Brownian motion and weaker inertial effects at such small scales.

2. **Lack of systematic evaluation of channel rigidity and design parameters**

While zigzag channels have been studied, the role of channel rigidity and the influence of key geometric factors, such as zigzag length, number of zigzags, zigzag angle, cross-sectional dimensions, and axial velocity, on focusing efficiency remain poorly understood. A systematic investigation of these parameters could enable the rational design of high-efficiency microchannels tailored for micrometer-sized particle focusing.

3. **Unexplored numerical modelling of micrometer-sized particles in zigzag channels**

Current numerical studies largely overlook micrometer-sized particles, particularly in zigzag geometries, where the complex interplay between inertial lift forces and secondary flow vortices significantly influences particle migration.

4. **Absence of experimental and numerical correlations for Dean drag velocity and Dean drag force in zigzag geometries**

Despite the significant role of Dean flow in secondary migration, there is a lack of experimentally validated or simulation-based correlations for Dean drag velocity and force specific to zigzag microchannels. Such correlations are crucial not only for optimization of microfluidic devices operating at the micro and nanoscale, but also for deepening the understanding of the underlying physics governing particle migration and focusing behavior.

5. **Need for efficient and quantitative bacterial enrichment in rigid zigzag microchannels**

While bacterial enrichment has been explored in other microfluidic geometries such as spiral and sheath-based channels, rigid zigzag microchannels have not yet been demonstrated as a platform for the efficient and quantitative enrichment of clinically important bacterial species such as *E. coli, Salmonella*, and *S. aureus*. Existing studies focus primarily on particle focusing, with no quantitative assessment of enrichment factor or post-enrichment viability under varying inlet concentrations. Demonstrating the capability of rigid zigzag channels to achieve high bacterial enrichment would significantly enhance their applicability in diagnostics, food safety, and environmental monitoring.

Based on the identified gaps in the current literature, this thesis seeks to address some of the following key research questions related to microparticle and bacterial manipulation using rigid zigzag microchannels:

- What is the effect of channel rigidity and key geometric parameters (zigzag length, number of zigzags, zigzag angle, cross-sectional dimensions, and axial velocity) on the focusing efficiency of micrometer-sized particles?
- How can numerical modelling be adapted to capture the focusing dynamics of micrometer-sized particles?
- Can experimental and numerical correlations be developed to accurately quantify Dean drag velocity and Dean drag force in zigzag geometries?
- Can rigid zigzag microchannels achieve efficient enrichment of clinically relevant bacterial species such as *E. coli*, *Salmonella*, and *S. aureus* across varying inlet concentrations? What enrichment factor can be achieved per run in the device, and how does it compare to theoretical predictions?
- Can scalable strategies, such as continuous recirculation, be used to enhance the enrichment performance toward detectable levels?

1.2.1. Thesis Goals and Objectives

Based on the identified research gaps and questions above, this study aims to optimize rigid zigzag microchannels for the efficient focusing of microparticles (1 - 3 μm) and *E. coli* as a biological application, by developing a fundamental understanding of how the key zigzag channel parameters influence particle focusing. This is followed by the quantitative enrichment of *E. coli* bacteria by approximately 10 factors with 100% post-enrichment viability. To achieve this, the following objectives will be pursued:

Obj. 1 - Experimental investigation on the inertial focusing behavior of 1- 3 μm particles inside soft and rigid zigzag microchannels.

This study aims to systematically investigate the effects of key parameters, including channel rigidity, particle size, and flow velocity, on the inertial focusing of 1- 3 μm particles. Specifically, zigzag microchannels were designed and fabricated using both soft polydimethylsiloxane (PDMS) via soft lithography and rigid polymethyl methacrylate (PMMA) via hot embossing, to evaluate the influence of channel rigidity. Subsequently, the above mentioned microparticles were tested across a range of flow velocities, and the resulting focusing behavior was quantified to assess the effects of particle size and axial velocity on focusing efficiency.

Obj. 2 - Enhancing the focusing quality and throughput of micrometer particles inside zigzag microchannels through numerical modeling and parametric analysis.

This objective involved a comprehensive parametric study to evaluate the effects of zigzag microchannel design parameters and flow velocity on the inertial focusing behavior of micrometer-sized particles. Key parameters under consideration included zigzag length, number of zigzags, zigzag angle, channel width, and axial velocity. The study was conducted through numerical modeling using COMSOL Multiphysics, guided by a Taguchi Design of Experiments (DOE) approach. The experimental data in Obj. 1 was utilized for the verification and validation of the numerical model. Finally, the results of the parametric study were utilized for identifying the optimal combination of parameters for efficient particle focusing at the center of the channel.

Obj. 3 - Enrichment and post-processing viability of E. coli bacteria inside rigid zigzag microchannels.

This study utilised the optimized zigzag channel in Obj. 2 to investigate the enrichment of *E. coli* bacteria across a range of inlet concentrations. First, a calibration curve for *E. coli* green

fluorescent protein (GFP) expression was established using a fluorometer to enable accurate quantification of bacterial concentrations at the inlet and outlet. Subsequently, enrichment experiments were conducted at various inlet concentrations with the goal of determining the enrichment factor achieved in each individual run. For each run, the experimentally obtained enrichment factor was compared to a theoretically calculated value, allowing us to quantify the deviation from ideal performance. This approach helped evaluate how efficiently the device enriches the sample per cycle. To improve overall enrichment, multiple consecutive runs were performed, and the enrichment factor at each stage was tracked. Finally, the viability of *E. coli* after enrichment in the device was assessed to determine the biological impact of the enrichment process.

1.3. Thesis Organization

The first chapter presents the research background, motivation, existing gaps, and the objectives of this thesis. It highlights the need to enhance the focusing of microparticles and microorganisms ranging from 1 to 3 μm in size in rigid zigzag microchannels for efficient enrichment.

The second chapter provides a comprehensive literature review of conventional and microfluidic techniques for enrichment. It begins with an overview of the conventional enrichment methods. Afterwards, active microfluidic techniques are briefly discussed, followed by a review of passive methods and the theory behind particle focusing in various microchannel geometries. The chapter ends with a review of previous numerical studies on particle focusing.

The third chapter presents a detailed description of the materials, fabrication procedure, experimental and numerical methods, and data analysis techniques employed in this study.

Furthermore, the chapter discusses the simulation setup, the governing equations used, and the parameters selected for the parametric study conducted to evaluate particle focusing efficiency.

The fourth chapter demonstrates the experimental and numerical results. Initially, it explores how particle diameter and flow velocity influence focusing efficiency. Furthermore, the chapter includes the verification and validation of the numerical model against experimental data and discusses the outcomes of the parametric study, highlighting how key factors affect particle focusing behavior.

The fifth chapter focuses on the focusing and enrichment of *E. coli* using the optimized microfluidic channel. The chapter then demonstrates the device's ability to enrich *E. coli* at various initial concentrations and reporting the corresponding enrichment factors.

The sixth and final chapter summarizes the key findings of the research, discusses the limitations of the current work, and offers suggestions and recommendations for future research.

1.4. Research Contributions

This thesis is currently being developed into two journal paper manuscripts and has resulted in one conference presentation. All three contributions were developed under the supervision of Prof. Pouya Rezai.

Conference: A. Refaei and P. Rezai, "Focusing Behavior of Micrometer Particles Inside Rigid Zigzag Microchannels and Application to *E. coli* Enrichment", *Abstract Accepted*, *The 29th International Conference on Miniaturized Systems for Chemistry and Life Sciences (μTAS 2025)*.

Chapter 2: Literature Review

2.1. Conventional Methods for Particle Manipulation and Enrichment

As discussed in Chapter 1, conventional techniques for enriching microparticles and microorganisms typically involve centrifugation, filtration, magnetic separation, sedimentation, and flocculation, each with its own advantages and limitations. While centrifugation is an efficient and fast method for enrichment with applications in clinical diagnostics, environmental monitoring, and industrial biotechnology, its lack of selectivity tends to result in the co-concentration of undesired particles along with possible cell damage [29], [30]. Filtration

techniques, more specifically membrane-based filtration techniques, are simple and widely applied, efficiently separating particles based on size; however, they are prone to the issues of filter clogging and non-selective enrichment [6]. Magnetic separation achieves improved specificity with the use of functionalized magnetic beads and appropriate biological sample handling, although its scalability and the expense of reagents restrict its applicability in large-scale or resource-poor environments [31]. Alternative approaches like gravitational sedimentation and chemical flocculation are cost and energy efficient and can be performed at high volumes, yet are typically slower, less specific, and require additional steps for particle recovery [32], [33]. Often, more than one technique needs to be employed to attain optimum enrichment for a specific application, a compromise on efficiency, specificity, scalability, and affordability [29], [30], [34].

Switching to microfluidics offers numerous advantages for particle manipulation and enrichment. Microfluidics is defined as the science and technology of precisely controlling small volumes of fluids, typically in the microliter to picoliter range, within channels of micrometer-scale dimensions. This platform enables enhanced control over the flow behavior and particle dynamics, offering benefits such as reduced sample consumption, faster processing, and the potential for device miniaturization and integration, making it highly suitable for biomedical and analytical applications.

The next sections provide an overview of two main categories of microfluidic methods used for particle manipulation and enrichment: Section 2.2.1 discusses active microfluidic methods, which employ external fields such as electric, magnetic, or acoustic forces, while Section 2.2.2 focuses on passive microfluidic methods, which rely on intrinsic hydrodynamic forces and channel geometry.

2.2. Microfluidic Methods for Particle Manipulation and Enrichment

2.2.1. Active Microfluidic Methods

Active microfluidic approaches to microparticle and microorganism enrichment employ externally applied forces such as electric, acoustic, magnetic, optical, and thermal forces for selective and efficient concentration from environmental and clinical samples [35], [36]. Dielectrophoresis (DEP) acts on particles depending on their dielectric properties in non-uniform electric fields and hence label-free cell and microparticle separation is possible, although it may be restricted by heating and forces near the electrodes [36], [37], [38]. Acoustofluidics (acoustophoresis) is based on size, density, and compressibility differences using ultrasonic waves and offers contactless, gentle enrichment for biological samples but generally needs to be carefully optimized for very small particles [39], [40]. Magnetophoresis separates magnetically labeled cells or particles, including immunomagnetically labeled pathogens or circulating tumor cells, with specificity and low physical stress but with the need for magnetic labeling or naturally magnetic targets [41], [42], [43]. Optical techniques such as optical tweezers provide precise manipulation using optical forces; however, these methods have lower throughput and thus are less effective for bulk processing [44]. Moreover, methods such as electrophoresis and thermophoresis use charge-based migration and temperature gradients, respectively, for selective separation in microfluidic devices [45].

Collectively, active methods improve the performances of microfluidic devices in microparticle and microorganism enrichment with greater applications in clinical diagnostics and environmental monitoring but with varying limitations [15]. These techniques often rely on costly components

such as electromagnetic, acoustic, or optical systems, which not only increase power consumption and heat generation but also require regular calibration and maintenance by trained personnel [15][16].

2.2.2. Passive Microfluidic Methods

Passive microfluidic methods exploit intrinsic hydrodynamic forces such as inertial lift force, drag force, and secondary flow vortices, to manipulate and focus particles without relying on external fields. These methods are particularly appealing due to their simplicity, low power requirements, and suitability for portable, label-free systems. The following subsections (2.2.2.1 and 2.2.2.2) provide a comprehensive overview of both experimental and numerical studies on passive particle focusing in various microfluidic geometries, emphasizing the underlying physical mechanisms and channel designs that enable efficient particle manipulation at the microscale.

2.2.2.1. Experimental Techniques in Microfluidics Microparticle Focusing

In a straight microchannel, inertial migration occurs in accordance with hydrodynamic principles, wherein initially dispersed particles migrate laterally to multiple equilibrium positions across both the length and cross-section of the channel. This phenomenon, called particle focusing, typically manifests between stokes flow ($Re \rightarrow 0$) and turbulent flow ($Re \gtrsim 2000$). Channel Reynolds number is defined as $Re = \rho U D_h / \mu$, where ρ, U, and μ are the density, average flow velocity, and dynamic viscosity of the fluid, respectively, and $D_h = 2wh/(w+h)$, where w is the channel width and h is the channel height. Particle Reynolds number defined as $Re_p = \rho U a_p / \mu$ is also used in particle microfluidics where $Re_p > 1$ is generally required to achieve particle focusing. Particle focusing is driven by a balance

between the shear gradient lift force (F_s) and the wall lift force (F_w) [17]. Shear gradient lift force (F_s) results from the parabolic nature of the laminar velocity profile, pushing particles away from the channel center and towards the walls [18]. Conversely, as particles approach the channel walls, F_w counteracts F_s, pushing particles away from the walls, as shown in Fig. 2-1 [46]. Once these forces reach equilibrium, particles settle into their focusing positions.

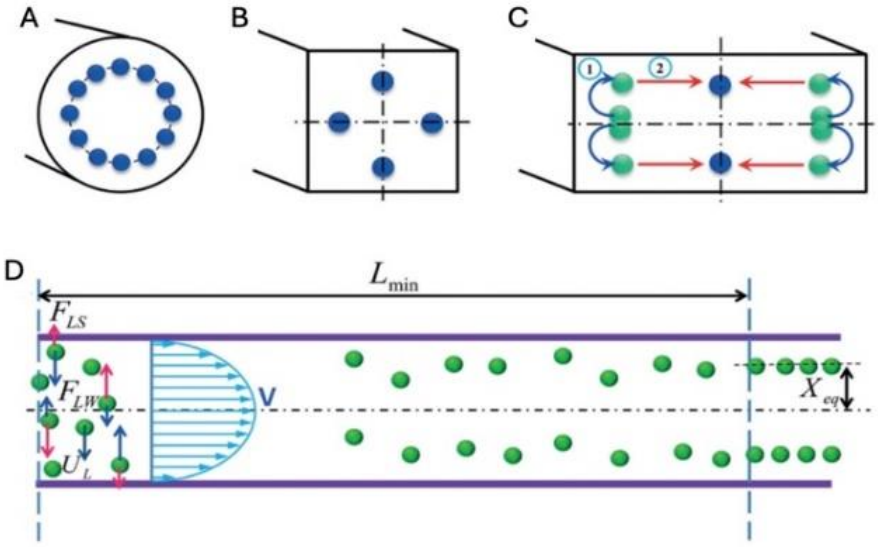

Figure 2-1 Demonstration of equilibrium positions in a straight microchannel with (A) circular, (B) square, and (C) rectangular cross section with AR = 0.5. (D) The lateral migration speed U_L and minimum channel length for particle focusing L_{min}. [46] Permission obtained from RSC.

The mathematical expression for the net lift force acting on a particle can be expressed as follows [47]:

$$F_L = \frac{f_L \rho U^2 a_P^4}{D_h^2} \qquad (2-1)$$

Here, a_p is the particles diameter and f_L is the dimensionless coefficient of inertial lift force which depends on the particle's position in the channel cross section, channel Reynolds number, and particle size.

In a straight channel with a circular cross-section, particles tend to move laterally towards a narrow annulus located around 0.6 times the channel radius from the axis as depicted in Fig. 2-1A. However, in a straight channel with a rectangular cross-section, such as those commonly used due to microfabrication constraints, the behavior becomes more intricate. In a square channel (with an aspect ratio $AR = h/w = 1$), particles typically concentrate at four equilibrium points, aligned with the center of each wall as it appears in Fig. 2-1B. Furthermore, in channels with a low aspect ratio ($AR \approx 0.5$), the equilibrium positions reduce to two, with particles focusing around 0.2 times the height away from the longer walls as it is shown in Fig. 2-1C. The lateral migration velocity (U_L) of particle can be determined by balancing the net inertial lift force (Eq. 2-1) with Stokes drag force (Eq. 2-2) as shown in Eq. 2-3 [46].

$$F_{stks} = 3\pi\mu a_p U_L \qquad (2-2)$$

$$U_L = \frac{F_L}{3\pi\mu a_p} = \frac{f_L \rho U^2 a_p^3}{3\pi\mu D_h^2} \qquad (2-3)$$

Generally, straight microchannels have been utilized by researchers to achieve microparticles and microorganisms focusing and separation. For instance, Mach and Di Carlo [48] introduced a microfluidic approach to filtering blood using simple straight channels (Fig. 2-2A), utilizing inertial forces only.

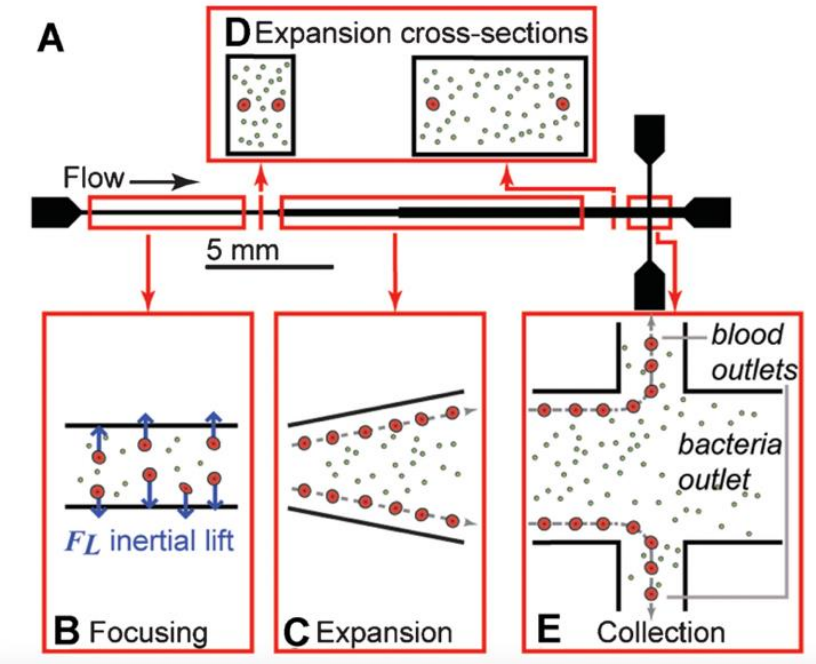

Figure 2-2 Amplification of inertial focusing for particle separation. (A) Schematic of a straight microchannel with one inlet and three outlets. (B) Larger particles experience inertial lift forces, causing differential migration toward equilibrium positions. (C, D) Top and cross-sectional views show how channel expansion drives red blood cells (RBCs) toward the channel walls. (E) RBCs are collected through the side outlets. [48] *Permission obtained from Biotechnology and Bioengineering.*

Their design features 40 parallel microchannels arranged in a radial layout and each channel starts with a narrow section that helps align cells based on their size (Fig. 2-2B). As blood flows through, larger red blood cells (around 8 μm) are pushed toward the walls, while *E. coli* bacteria (about 1 μm) stays dispersed as shown in Fig. 2-2C. This positioning allows the two to be separated downstream using three outlets (Fig. 2-2E); however, the device required two passes through the device to remove around 80% of bacteria and concentrate red blood cells by about 4 times. Therefore, further enhancement in particles focusing remains necessary to decrease the operating time.

A change in the channel cross-section geometry can further enhance particle focusing into one focusing stream in straight channels. For instance, Ukherjee et al. [49] developed a novel microfluidic device for single position inertial focusing using low aspect ratio (*AR*) triangular microchannels (Fig 2-3).

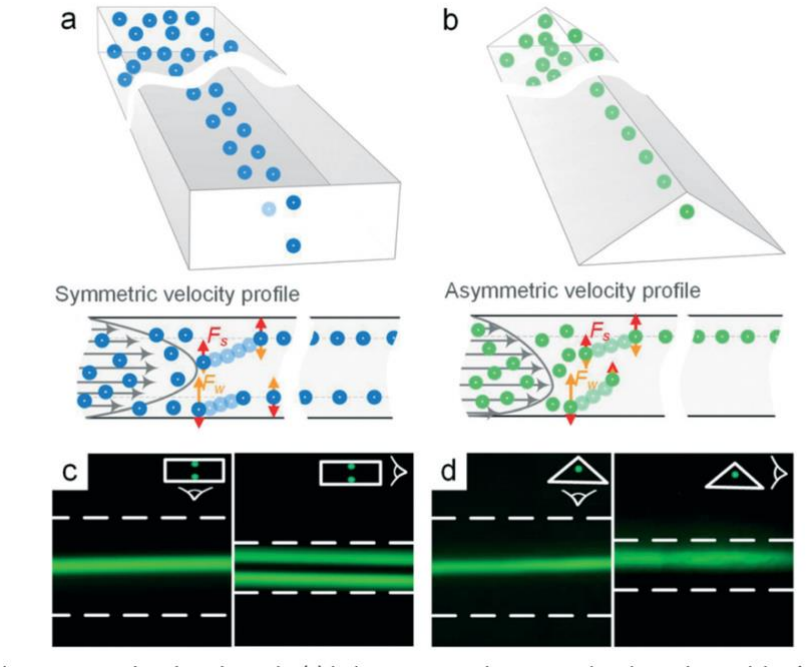

Figure 2-3 Particle focusing in low aspect ratio microchannels. (a) In rectangular microchannels with low aspect ratio (b) Triangular microchannels with low aspect ratio exhibit a compressed, asymmetric velocity profile, concentrating particles near the apex. (c, d) Fluorescence images showing top and side views of 15 µm particles focusing in 100 µm × 40 µm rectangular and triangular channels, respectively. [49] *Permission obtained from RSC.*

The triangular cross section creates an asymmetric velocity profile that pushes particles toward a single stable focusing position near the apex of the channel. The microchannel had a width of 100 µm, a height of 40 µm, with a total length of 5 cm, and was fabricated using micromilling on PMMA to produce positive masters for PDMS casting. The focusing behavior was examined using polystyrene beads of different diameters (7.32, 10, 15, and 18 µm) across flow rates from 30 to 650 µL/min (*Re* from 8.4 to 190). In contrast to

conventional rectangular channels, which result in multiple lateral equilibrium positions (Fig. 2-3(A, C)), at *Re* = 29, 15 µm beads achieved a single stream of focusing near the apex as shown in Fig. 2-3(B, D). However, fabricating microchannels with a triangular cross-section is considered costly and technically challenging, in addition to the complexity of designing outlet configurations suitable for efficient enrichment.

Introducing curvature into the channel geometry can significantly enhance lateral particle migration, enabling faster alignment to controlled equilibrium positions compared to straight channels. In such geometries, the parabolic profile of laminar flow shift more towards the outer wall [50]. This shift results in a mismatch between fluid momentum in the channel center and near the wall, generating a pressure gradient in the radial direction [17]. Consequently, fluid flows outward due to the presence of higher momentum near the channel center, creating nearly constant streams that push toward the walls. This motion generates two counter-rotating vortices in the corners, known as Dean vortices, as shown in Fig. 2-4 [51], which reduce the required length for particles to reach their equilibrium position compared with straight channels, especially for small particles that need very long length.

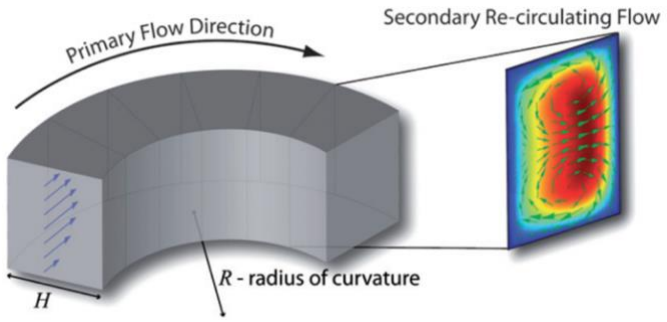

Figure 2-4 Curved microchannels under inertial flow conditions, the faster-moving fluid at the center tends to maintain its outward trajectory due to momentum. To conserve mass, the slower-moving fluid near the channel

walls circulates inward, resulting in the formation of two counter-rotating vortices perpendicular to the main flow direction. [18] *Permission obtained from RSC.*

The magnitude of this secondary flow can be described with the Dean number (De) and can be calculated as follows [52]:

$$De = Re\sqrt{\frac{D_h}{2R}} \qquad (2-4)$$

Here, R is the radius of curvature as shown in Fig. 2-4.

Particle migration is highly influenced by their size, with inertial lift forces (F_L) being proportional to particle size to the power of four ($F_L \propto a_P^4$) (Eq. 2-1), and Dean drag force (F_D) being proportional to particle size to the power of one ($F_D \propto a_P$) (Eq. 2-2). The maximum value of Dean drag force can be estimated as follows [52]:

$$F_D \sim \frac{\mu^2 a_p De^2}{\rho D_h} \qquad (2-5)$$

The ratio of inertial lift force to the Dean drag force (F_L/F_D) plays a pivotal role in determining the final equilibrium position of particles of a given size [17]. Typically, at a constant Re, small particles remain dispersed as the Dean drag force dominates ($F_D > F_L$), whereas larger particles become focused immediately due to the dominance of inertial lift forces ($F_L \geq F_D$).

Researchers have utilized curved microchannels to enhance particle focusing efficiency. For instance, Martel and Toner [53] investigated how particles behave in curved microfluidic channels by controlling the flow conditions and channel geometry as shown in Fig. 2-5.

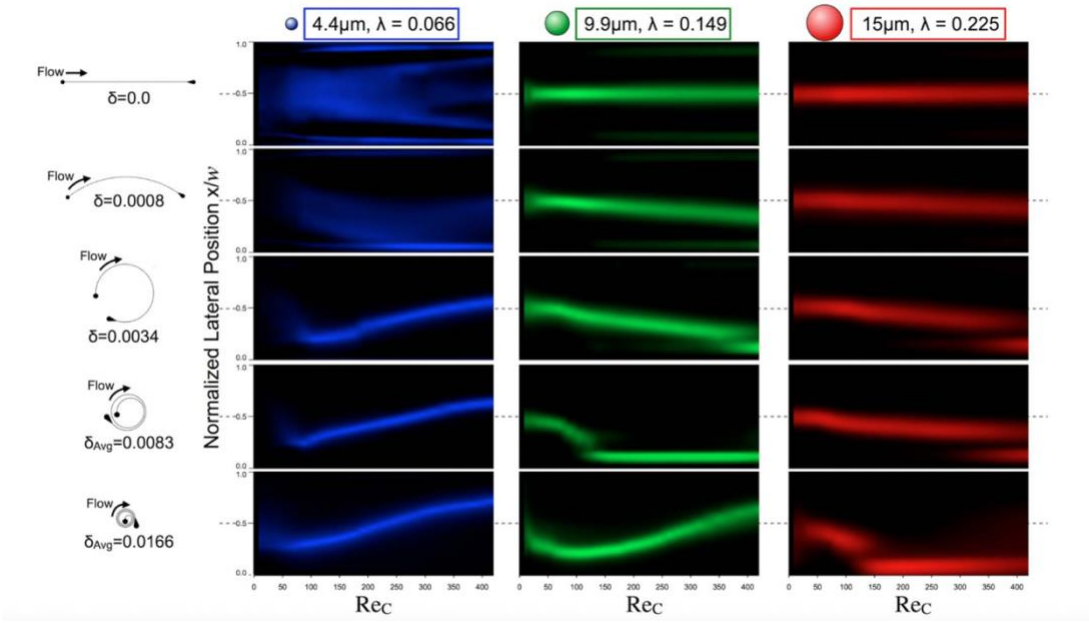

Figure 2-5 Channel Reynolds number (Re_C) maps for each condition of curvature and particle confinement. [53]

They fabricated rigid epoxy channels with a cross section of 100 μm in width, 50 μm in height, and 4 cm in length, but varied the curvature to investigate how it affects particle focusing. They used fluorescent polystyrene beads with diameters of 4.4 μm (λ = 0.066), 9.9 μm (λ = 0.149), and 15 μm (λ = 0.225), where λ is the confinement ratio (a_p/D_h). The experiments covered a wide range of Reynolds numbers (*Re* from ~9 to over 400) and Dean numbers (*De* from ~ 0 to over 50), with flow rates ranging from 25 μL/min to 1200 μL/min. At specific combinations of flow rate and curvature, the particles achieved a stable single stream of focusing near the inner wall, resulting in highly confined streaks.

In Fig. 2-5, the optimum single stream focusing for 15 μm particles occurred at $Re \approx 150$ in a channel with $\delta = 0.0166$, where δ is the curvature ratio $\delta = D_h/2R$, while for 9.9 μm particles, it happened at $Re \approx 150$ and $\delta = 0.0083$, and for 4.4 μm particles at $Re \approx 200$ and

$\delta = 0.0008$; however, a partial focusing was observed for 4.4 µm. That is attributed to the insufficient channel length, which might have prevented all particles from fully migrating to their equilibrium location. Increasing the channel length expands the overall footprint, adds significant hydraulic resistance, and complicates device operation. Therefore, exploring new channel geometries is essential to achieve efficient focusing for microparticles within shorter length.

Building on curved channels, introducing alternating curvature such as serpentine, square wave, and zigzag designs, the fluid flow generates Dean drag forces that periodically reverse direction. As particles follow through these alternating curvatures multiple times, the repeated interaction between Dean drag and inertial lift forces promotes migration toward more stable equilibrium positions, resulting in narrower focusing bands compared with normal curved channels. For example, Özbey et al. [54] investigated the inertial

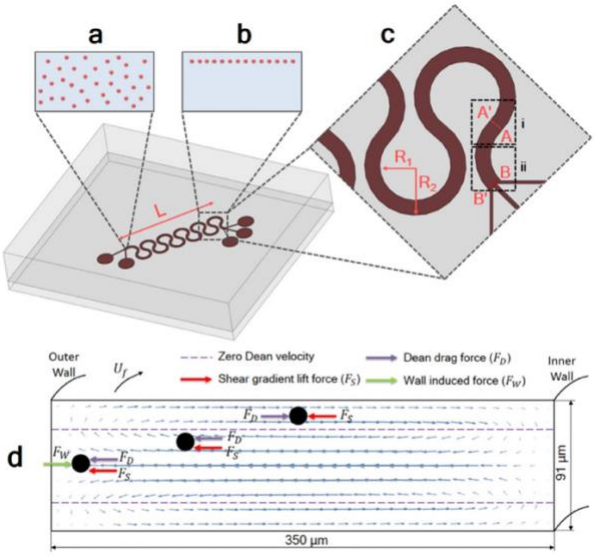

Figure 2-6 Schematic illustration of the microparticle focusing device. (a) Particles are initially distributed randomly at the inlet. (b) As they progress, they converge into a focused stream at the AA' cross-section within the transition region. (c) Enlarged views of (i) the transition region and (ii) the outlet region is shown, with channel dimensions R_1 = 800 µm, R_2 = 1150 µm, and length L = 9.75 mm. (d) A diagram illustrating the directions of dominant forces acting on particles at various positions within the channel. [54]

focusing behavior of microparticles in curvilinear microchannels with a high curvature angle (280°) as shown in Fig 2-6.

The microchannel consisted of 11 symmetric curvatures with an inner radius of 800 μm, outer radius of 1150 μm, width of 350 μm, and height of 91 μm, with a channel length of 9.75 mm. They performed their experiments at flow rates ranging from 400 to 2700 μL/min (*Re* between 30 and 205). Their aim was to analyze the effects of inertial lift and Dean drag forces on different size particles (10, 15, and 20 μm) across a wide range of Reynolds numbers. The study revealed that large (20 μm) particles focused stably near the channel centerline over a broad *Re* range as shown in Fig. 2-6B, while medium size (15 μm) particles initially formed a narrow-focused stream at intermediate Reynolds numbers ($Re \approx 60–100$), but they began to defocus at higher Reynolds numbers ($Re > 136$). As the flow rate increased, the vertical position of particles shifted, causing the Dean drag force to act in the same direction as the lift force, which led to lateral migration toward the outer wall and disrupted stable focusing. Small particles (10 μm) failed to focus efficiently due to their lower lift force in the used cross section compared with the larger particles. Fig. 2-6D illustrates the directions of dominant forces acting on particles at various positions within the channel.

Building on the previously discussed geometry, in a biological context, Ozbey et al. [55] investigated the inertial focusing of cancer cell in a curvilinear microchannel with a 280°curvature as shown in Fig. 2-7, aiming to isolate circulating tumor cells (CTCs) from white blood cells.

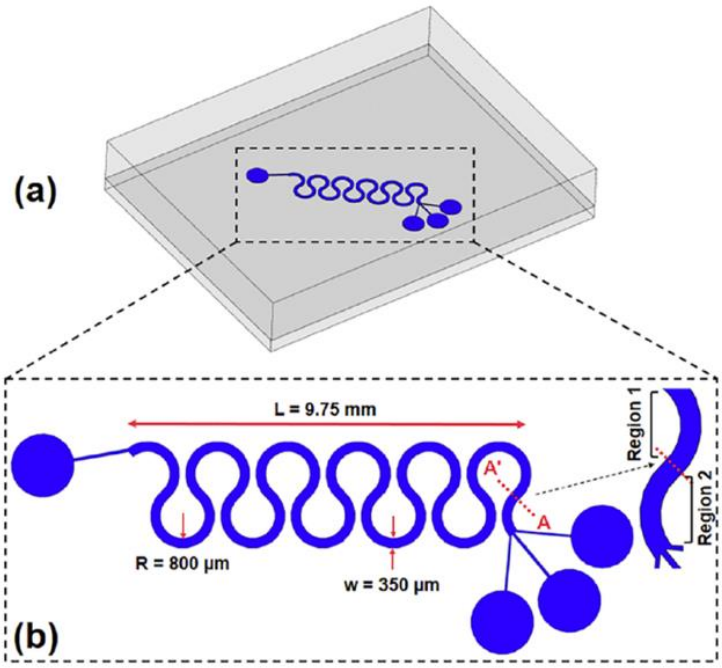

Figure 2-7 (a) Schematic of the microfluidic chip for isolating circulating tumor cells (CTCs) from white blood cells. (b) Close up view of the curvilinear microchannel with dimensions. [55]

The microchannel had a width of 350 µm, height of 91 µm, and radius of curvature of 800 µm. Using four cancer cell types (MDA-MB-231, HeLa, K562), and Jurkat (as surrogates for white blood cells), they examined the effects of curvature and flow rate (ranging from 400 µL/min to 2700 µL/min) on focusing behavior. At an optimal Reynolds number of ~121 (corresponding to a flow rate around 1800 µL/min), MDA and HeLa cells formed distinct focusing streams separated from Jurkat cells, enabling effective size-based separation. The study confirmed that curvature-induced Dean flow, in conjunction with inertial lift forces, could achieve efficient separation while maintaining high cell viability (>94%). This work demonstrates the potential of simple curvilinear microchannels for passive CTC isolation in clinical liquid biopsy applications.

Although symmetric serpentine channels have been widely explored for inertial focusing, they often lead to multiple equilibrium positions. The introduction of asymmetry reduces the number of focusing positions and shortens the length required for focusing compared to symmetric channels. For instance, Wang and Dandy [13] developed a high throughput inertial microfluidic device capable of focusing and separating microparticles using an asymmetric serpentine microchannel (Fig. 2-8).

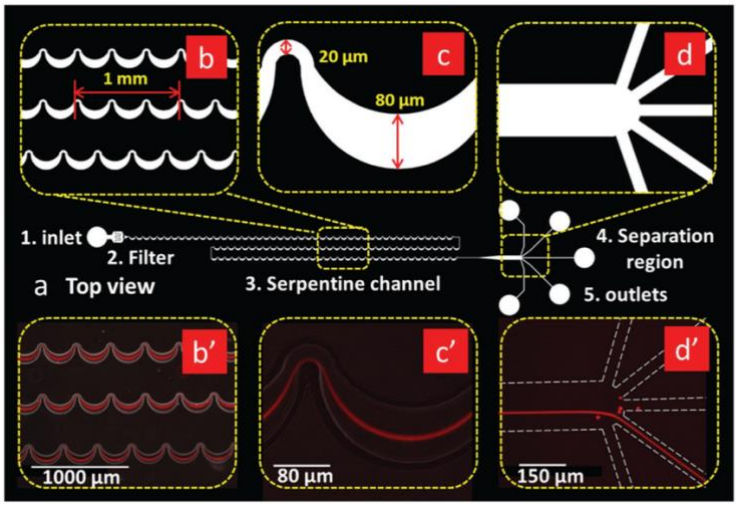

Figure 2-8 Design and operation of serpentine microfluidic channel for focusing 2 µm red fluorescent particles. (a) Top view schematic of the full inertial focusing device, featuring a 4.5 cm-long serpentine section. (b) Enlarged view of the serpentine curved channel and (b') corresponding fluorescence image showing focused particle streams. (c) Magnified image of a single serpentine unit with channel widths of 20 µm (small bend) and 80 µm (large bend), and (c') fluorescence image confirming particle focusing at this location. (d) Close-up of the isolation region and (d') its corresponding fluorescence image showing focused 2 µm particles. White dashed lines denote microchannel boundaries. [13]

The device was fabricated from rigid thermoset polyester (TPE) to withstand high flow rates and avoid deformation, enabling reliable focusing at Reynolds numbers up to 1550. A channel with cross section of 20 µm × 10 µm and a total channel length of 4 mm, was used to successfully focus 2 µm particles; however, this geometry was insufficient for effective focusing of 920 nm particles. As a result, a smaller channel with dimensions of

10 μm × 5 μm had to be fabricated to achieve focusing of the 920 nm particles. While this approach enabled micrometer particles focusing, it required decreasing the hydraulic diameter significantly to meet a blockage ratio ($\beta = a_p / D_h$) > 0.07 for efficient focusing. Working with such very narrow cross sections is very complicated, significantly increases the risk of clogging and poses practical challenges in device operation and sample handling.

Researchers have also developed other channel geometries to achieve efficient particle focusing at blockage ratio below 0.07, which is typically challenging with small particles. For example, Bazaz SR et al [17] used rigid zigzag channels for enhancing the focusing efficiency of microparticles and cells and reduced the required blockage ratio. The device was fabricated using high-resolution 3D printing, with channel cross-sectional dimensions of 140 μm × 40 μm. It operated across a wide Reynolds number range of 15.5 to 134, with flow rates ranging from 0.1 to 0.8 mL/min and polystyrene particles with diameters of 3, 5, 7, 10, 15, and 20 μm were tested. Their findings demonstrate that the rigid zigzag channel efficiently focuses particles that satisfy the criterion of $a_p/D_h \geq 0.04$. This marks a significant enhancement compared to conventional microchannels made of PDMS, which require particles meeting the criteria of $a_p/D_h \geq 0.07$ for optimal focusing [18].

The unique design of zigzag channel lies in the abrupt changes in channel cross-section after passing each loop, resulting in more stable equilibrium positions and narrower focusing bands compared to curvilinear and square wave channels. This effect is amplified in zigzag channel width sharp corner device due to the sudden change of the cross-section at the corner. A schematic illustration of such a device is depicted in Fig. 2-9.

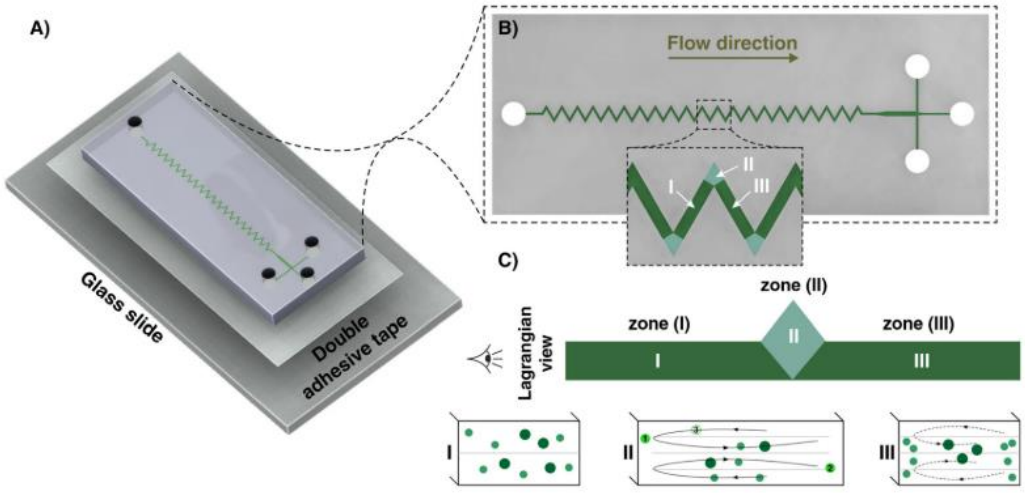

Figure 2-9 An overview of the z-rise device: (A) the z-rise inertial microfluidic channel is depicted on a macroscopic scale. (B) detailed view of the z-rise channel. (C) from a lagrangian perspective, the zigzag microchannel comprises a series of straight microchannels with a distinctive cross-section expansion. [17] *Permission obtained from RSC.*

Particle focusing within the channel (Fig. 2-9B) can be understood as a three-stage process occurring in distinct zones (Fig. 2-9C) [17]. In the Lagrangian view, particles sense the cross-section expansion as they traverse the zigzag microchannel. In zone I, particles experience the influence of inertial lift forces. The behavior of lift forces, which is linked to the blockage ratio, increases near the centerline, prompting larger particles to migrate towards the microchannel's center (as depicted in Fig. 2-9CI). Upon reaching the corner (zone II), the forces acting on particles undergo abrupt changes due to the expansion of the channel cross-section. Here, particles are subjected to Dean drag force, with Dean drag exerting a strong influence on particles at the midline, directing large particles towards the middle and small particles towards the sides (Fig. 2-9CII). This leads to the establishment of a stable equilibrium position. In zone III, the straight region, the fluid retains a memory of zone II and particles become stable at that position (as depicted in Fig. 2-9CIII), resulting in focused streams of particles for both particles size. In conclusion, the unique

geometry of zigzag channel and rigidity of the channel generate stronger forces on flowing particles and lead to enhanced focusing behavior [13], [17].

Figure 2-10A illustrates the focusing behavior of rigid zigzag microchannels in comparison to soft (PDMS) zigzag microchannels. At flow rates of 200 and 500 µL/min, 3 µm particles remained dispersed in the soft PDMS zigzag channel, while the rigid device achieved clear side wall focusing, demonstrating the impact of channel rigidity on focusing quality. This difference is attributed to the deformability of the PDMS material, which causes the channel to expand under flow, weakening the Dean drag forces and disrupting the focusing conditions. In contrast, the rigid channel maintains its geometry under flow, enabling stronger Dean flow and improved focusing performance, achieving efficient focusing at a blockage ratio ≥ 0.04.

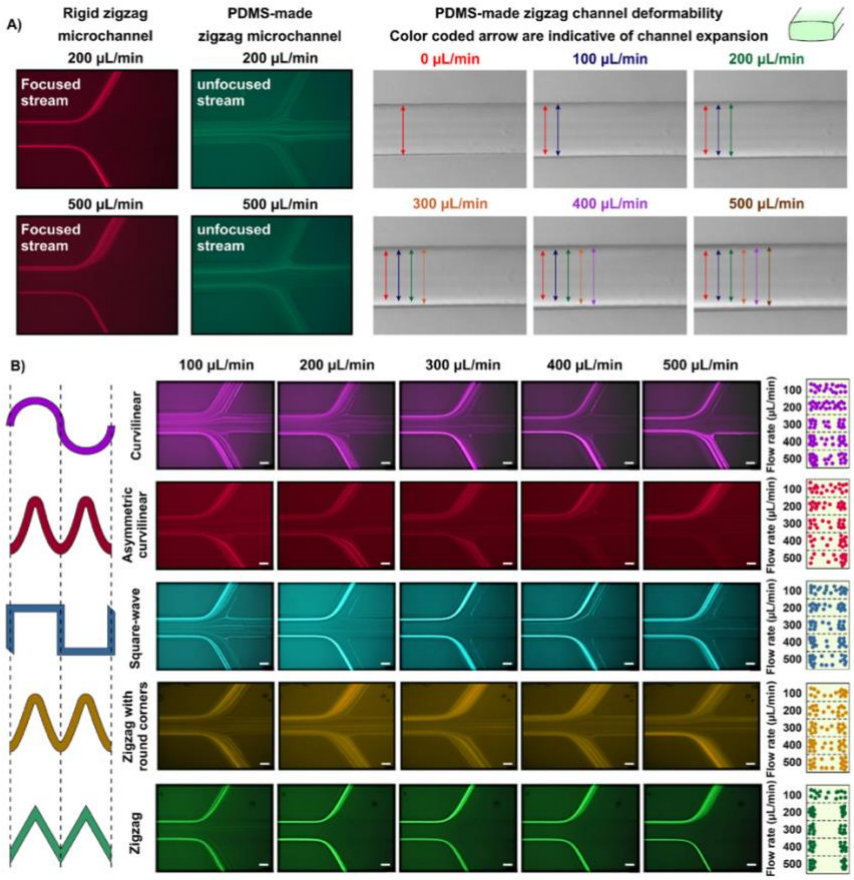

Figure 2-10 (A) Effect of channel rigidity on 3 μm particles' focusing. (B) Comparison between various channel geometry at flow rates from 100 μL/min to 500 μL/min. [17] *Permission obtained from RSC.*

Figure 2-10B shows various serpentine geometries including symmetric curvilinear, asymmetric curvilinear, square-wave, zigzag with round, and zigzag with sharp corners. Among the serpentine geometries tested, only the rigid zigzag channel with sharp corners focused 3 µm particles across all flow rates tested. Other designs failed to focus the particles, highlighting the superior performance of zigzag channel with sharp corners.

Another study by Shrestha J et al. [11] developed a PDMS-based inertial microfluidic device featuring a sharp zigzag microchannel for the rapid and label-free separation of bacterial cells from primary human nasal swab samples (Fig. 2-11).

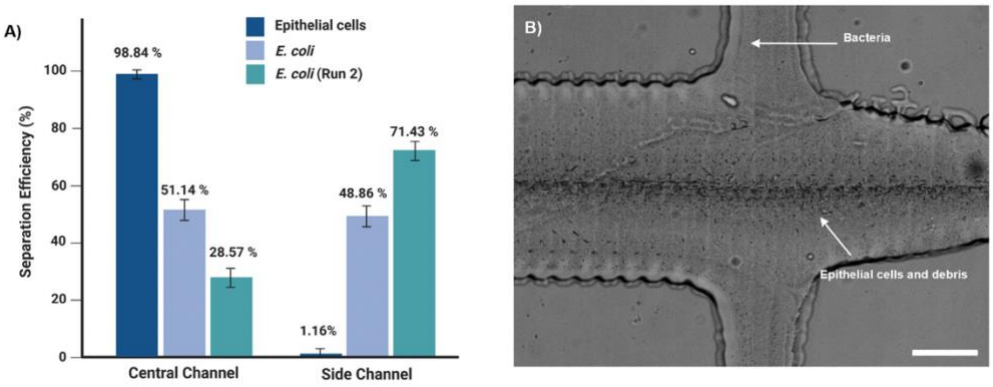

Figure 2-11 Evaluation of bacterial separation using the zigzag microfluidic channel. (A) Separation efficiency of epithelial cells and E. coli. (B) At a flow rate of 150 μL/min, epithelial cells and debris focused at the central outlet, while E. coli remained dispersed across the channel. [11] *Permission obtained from RSC.*

The channel had a cross-sectional dimension of 120 µm × 40 µm and was able to separate *E. coli* bacteria (~1 µm) from epithelial cells and debris (>3 µm) based on differential focusing behavior. The device operated at flow rates ranging from 50 to 200 µL/min (optimized at 150 µL/min); however, the separation efficiency of *E. coli* was ~ 50% after the first run and ~ 72%

after two runs as shown in Fig. 2-11A. Fig. 2-11B shows epithelial cells and debris focused at the central outlet, while *E. coli* remained dispersed across the channel at a flow rate of 150 μL/min.

2.2.2.1.1. Experimental Research Gaps in Microparticle Focusing in Zigzag Microchannels

Although previous studies have demonstrated the potential of zigzag microchannels for particle focusing and separation, several gaps remain in both fundamental understanding and practical applications. Most existing work has focused on microparticles and microorganisms larger than 1 μm, and there is a lack of systematic investigation into key geometric parameters such as zigzag length, number of zigzags, zigzag angle, cross-sectional dimensions, axial velocity, and channel rigidity on the focusing behavior of micrometer-sized particles, as well as their biological applications. Furthermore, there is a lack of experimental correlations for Dean drag velocity and Dean drag force specific to zigzag geometries, which hinders predictive modeling and device optimization for both microscale and nanoscale applications.

From a practical standpoint, the use of zigzag channels for quantitative bacterial enrichment has not been thoroughly investigated, particularly across various concentration levels or with clinically relevant species such as *E. coli, Salmonella, and S. aureus*. Furthermore, no prior studies have developed scalable strategies for enhancing enrichment factor, such as continuous recirculation of the sample through the device until detectable concentrations are achieved. These gaps highlight the need for continued research that bridges fundamental fluid-particle interactions with practical device design and real-world implementation.

2.2.2.2. Numerical Techniques in Microfluidics Microparticle Focusing

In recent years, numerical approaches have become a powerful tool for exploring how particles behave in microfluidic systems. Starting with simulating the motion of spherical particles in fluid environments that was restricted to two-dimensional domains [56], [57]. Recently, more complex geometries such as straight and spiral microchannels have been simulated [58], [59]. Early solvers like Polyflow [60], [61] and CFD-ACE [58], [62] were widely used but eventually fell out of favor due to their limitations in handling the multi-physics nature of microfluidic systems. These days, COMSOL Multiphysics and ANSYS Fluent are preferred for their versatility, accuracy, and ease of use in solving coupled physical phenomena. These advanced models offer the significant benefit of enabling the analysis of multiple interacting forces involved in particle focusing and separation.

As the experimental microfluidic methods progressed towards adoption of active methods, so did the numerical techniques. For example, Forbes and Forry [63] developed a numerical model to study magnetophoretic separation of rare mammalian cells that were labeled with immunomagnetic tags in a microfluidic setting. Their simulation considered factors such as magnetic field orientation, magnet type, flow rate, channel design, and buffer composition to optimize the separation efficiency. Similarly, Hale and Darabi [64] used COMSOL Multiphysics to model a magnetophoretic microfluidic device designed for DNA isolation, analyzing how different parameters influenced the magnetic flux within the separation channel.

Furthermore, as research increasingly focused on passive microfluidic methods, numerical modeling efforts also began to align with this trend. Researchers have focused on understanding particles focusing using passive methods in straight [23], [24], spiral [25], [65], sinusoidal [26], [66], square wave channels [27], and other geometries [28], revealing how factors such as particle

size, channel geometry, and flow conditions affect particle migration [22]. For instance, Amin [65] used ANSYS Fluent with the Discrete Phase Model (DPM) to study inertial focusing in a spiral microchannel with a trapezoidal cross-section. The simulation accounted for key forces acting on the particles, including drag, buoyancy, and lift, with the lift force incorporated through a User Defined Function (UDF). A polynomial expression was developed to estimate the lift coefficient as a function of Reynolds number. Building on this, Parrot [67] modified the model by correlating the lift coefficient with the particle's distance from the channel wall rather than with Reynolds number. Their approach successfully produced particle focusing behavior consistent with experimental data, although the model's applicability remained restricted to a narrow range of Reynolds numbers.

Researchers also utilized computational methods for channel optimization for particles and microorganisms inertial focusing. For instance, Khodayari et al. [68] introduced a novel inertial microfluidic device featuring an optimized triangular microchannel geometry as shown in Fig. 2-12 for high-throughput separation of circulating tumor cells (CTCs) from white blood cells (WBCs). The microchannel had a cross-section of 200 μm × 100 μm, with triangular angles of 30° and 60°, and fillet curvature radii (R) ranging from 100 to 400 μm. The device operated at flow rates between 0.5 and 2.0 mL/min, corresponding to Reynolds numbers ranging from 24.7 to 98.9. CTCs ranging from 15-30 μm in diameter and WBCs of 10 μm were tested. Simulations revealed that a 60° triangular channel with R = 200 μm achieved 100% separation efficiency and purity for CTCs ≥ 20 μm at 2 mL/min as the 60° curvature induces stronger Dean vortices compared to the 30° design. Experimental validation using MCF-7 cells and WBCs confirmed high performance, achieving 95.7% efficiency and 93.3% purity at a 1:30 ratio and 93.2% efficiency and 92.5% purity at 1:5000.

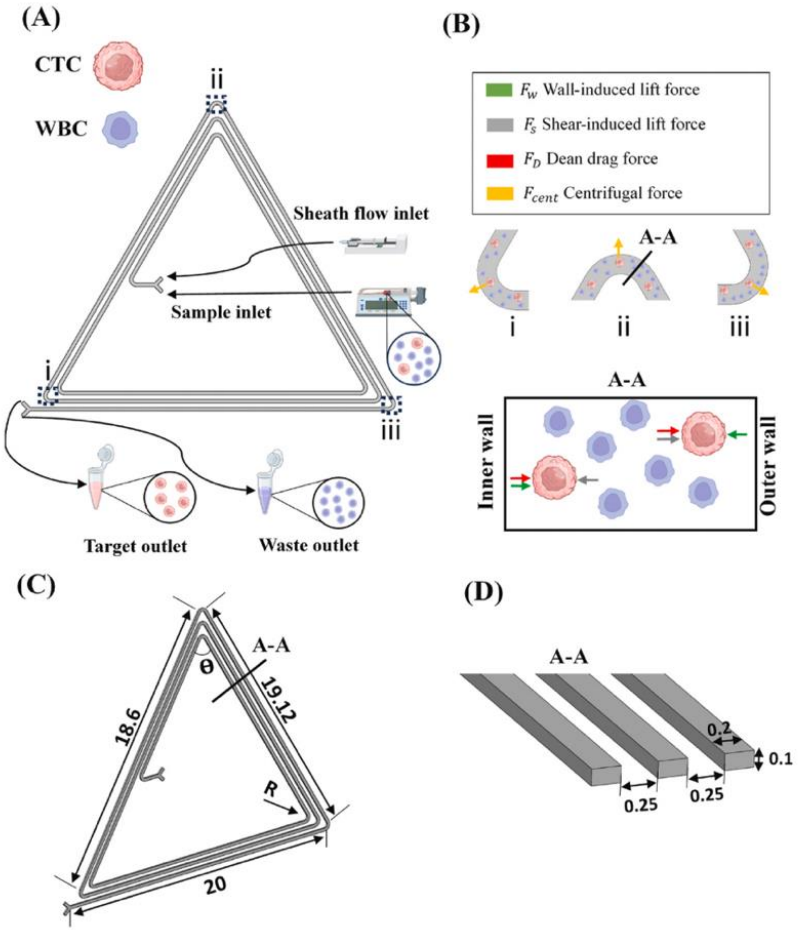

Figure 2-12 Schematic representation of the experimental setup and triangular microchannel design for inertial cell separation. (A) Illustration of introducing a mixture of circulating tumor cells (CTCs) and white blood cells (WBCs) into the triangular microchannel. (B) Schematic of the key forces acting on cells at the triangular bends, including wall-induced lift forces, shear forces, centrifugal forces, and Dean drag. (C) 3D view of the triangular microchannel featuring vertex angles of 30° and 60°, and (D) cross-sectional geometry with a channel width of 200 µm, height of 100 µm, and variable curvature radius (R) ranging from 100 to 400 µm. [68] *permission obtained from Elsevier.*

Another study by Yue Ying and Ying Lin [69] conducted a numerical study to evaluate the performance of three curved microchannel designs (zigzag, serpentine, and square wave) for inertial particle focusing and separation (Fig. 2-13).

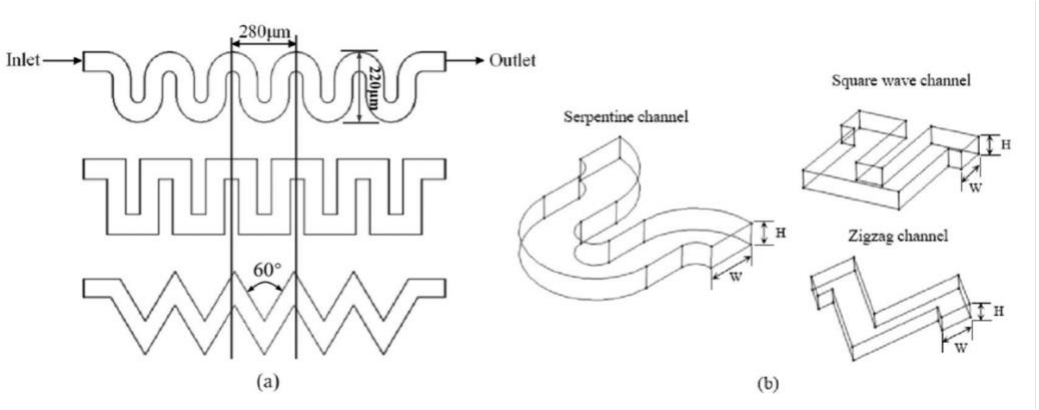

Figure 2-13 Schematic diagrams of the three curved channels. (a) top view of the three curved channels and (b) unit structure of the three curved channels. [69]

All channels shared the same dimensions: 80 μm in width, 40 μm in height, and a repeating unit length of 280 μm as depicted in Fig. 2-13(A,B). The simulations were performed using 5 μm and 10 μm spherical particles across a range of Reynolds numbers. The results revealed that 10 μm particles showed single stream focusing in all three geometries once *Re* exceeded 60. However, the 5 μm particles required higher Reynolds numbers to focus efficiently, with the zigzag channel consistently demonstrating superior performance in terms of focusing at high flow rates. Most notably, at *Re* = 62.5, the zigzag channel achieved a clear separation between the smaller and larger particles, enabling efficient passive size-based separation. In addition to its focusing and separation capabilities, the zigzag design exhibited the lowest pressure drop, averaging 13.9% less than the serpentine and 22.7% less than the square wave channel. These findings make the zigzag channel a particularly promising option for label-free particle focusing and separation in microfluidic applications.

Another study by Bazaz et al. [17] utilized numerical simulations using Direct Numerical Simulation (DNS) to validate 3 μm particles migration in rigid zigzag microchannels (Fig. 2-14).

Bazaz et al. [17] simulated the flow and particle trajectories within zigzag channel, revealing how the velocity field shifts at each zigzag turn (Fig. 2-14A). Fig. 2-14B identifies regions where either inertial lift or Dean drag forces dominate, highlighting the periodic transformation of force

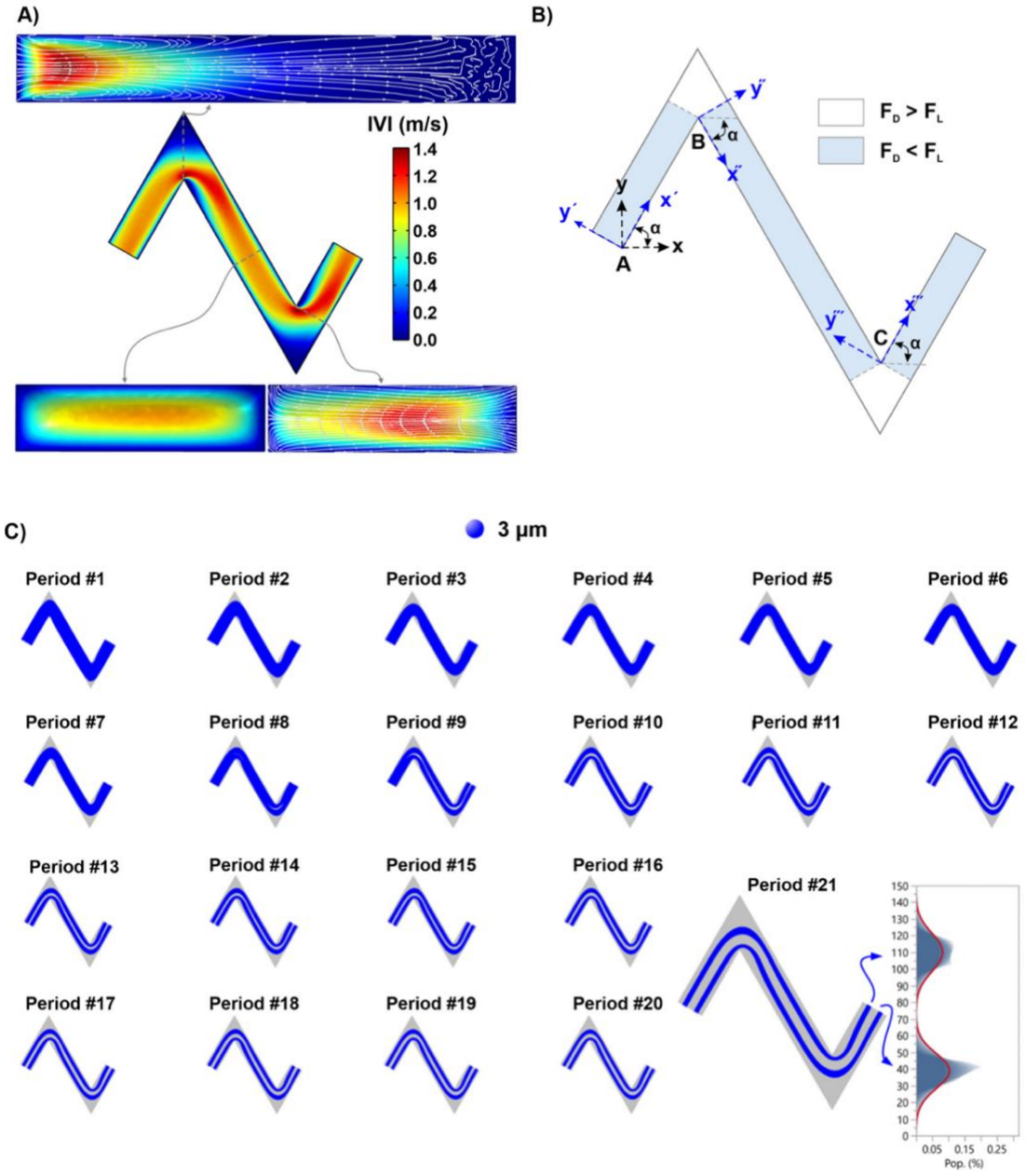

Figure 2-14 Numerical simulations and particle trajectories in zigzag channels. (A) Velocity contours show shifting flow patterns. (B) Lift- and drag-dominated regions are marked, with reference points A, B, and C; lateral flow appears at bends due to channel curvature and inertia. (C) Particle trajectories reveal that small particles focus near the sidewalls. [17] *Permission obtained from RSC.*

balance along the channel. Their particle tracing results showed that smaller particles (3 μm) gradually focused near the sidewalls after nine periods (Fig. 2-14C), while larger particles (15 μm) rapidly aligned at the centerline within just seven loops demonstrating that particle size and the corresponding lift-to-drag force ratio determine the final focusing position.

2.2.2.2.1. Numerical Research Gaps in Numerical Modeling of Zigzag Channels

Although numerical modeling has significantly contributed to the understanding of inertial particle focusing in various microfluidic geometries, several important gaps remain, particularly for curved geometries such as zigzag microchannels. For instance, previous modeling efforts in zigzag microchannels have focused on microparticles larger than 1 μm and there is a need to extend the numerical modeling to investigate the focusing of 1 μm by exploring key geometric parameters such as zigzag length, number of zigzag, zigzag angle, cross-sectional dimensions, and flow velocity, which remains a significant challenge. Additionally, the Dean drag velocity in zigzag microchannels has not been systematically quantified through simulations. Numerical investigation of this phenomenon would enable the development of correlations for Dean drag velocity and Dean drag force, specific to zigzag geometries. Such correlations would enhance the predictive accuracy of inertial focusing models, facilitate the design of more efficient microfluidic devices, and contribute to a deeper understanding of flow dynamics in zigzag microchannels.

Chapter 3: Materials and Methods

This chapter outlines the materials, experimental procedures, and numerical modelling techniques employed throughout this thesis. Section 3.1 introduces the materials used and the protocols followed for preparing microparticle and bacterial samples. The design and fabrication processes of both soft (PDMS) and rigid (PMMA) microfluidic devices are described in Section 3.2. Section 3.3 details the experimental setup and procedures, as well as the methods used to quantify *E. coli* concentration and establish a fluorescence-based calibration curve. Section 3.4 explains the image processing and particle tracking methods used to evaluate the focusing behavior. Finally, Section 3.5 presents the governing equations and boundary conditions applied in COMSOL simulations for fluid flow and particle tracing, along with the Taguchi-based design of experiments used to systematically assess the effects of key channel geometries and flow parameters on particle focusing efficiency.

3.1. Materials and sample preparation

Table 1 lists the materials used in this study and their sources.

Table 3-1 List of materials used and their procurement sources.

Material	**Source**
SU-8 2035 Photoresist	MicroChem Corp., USA
4-inch silicon wafers	Wafer World Inc., USA
Polydimethylsiloxane (PDMS) prepolymer and curing agent	Sylgard 184 silicone elastomer kit, Dow Corning, USA
Polymethyl methacrylate (PMMA) sheets	McMaster-Carr, USA
Adhesive double-sided tape (ARcare 8939)	AR Global, USA
Polystyrene Microparticles 1 μm (1.0-1.9 μm, FP-4056-2, 1% w/v) 2.7 μm (2.5-3.6 μm, FP-3056-2, 1% w/v) 3.9 μm (3.6-4.5 μm, FP-4056-2, 1% w/v)	Spherotech Inc., USA
E. coli OP50 expressing green fluorescent protein (GFP)	Caenorhabditis Genetics Center, University of Minnesota, Minneapolis, MN, USA

For sample preparation, particles with nominal diameters of 1, 2.7, and 3.9 μm were spiked into deionized (DI) water at an approximate concentration of 10^5/mL and supplied through the microfluidic channel inlet. GFP *E. coli* bacteria were cultured at 37 °C in Luria Broth (LB) medium for 24 hours and the bacterial concentration was determined using the plate counting method, yielding approximately 5×10^8 colony forming unit (CFU)/mL. The *E. coli* culture was subsequently diluted using DI water to achieve the desired concentration for use in microfluidic devices.

3.2. Design and fabrication of microfluidic devices

To fabricate microfluidic devices with zigzag channels (Fig. 3-1), silicon wafer molds were fabricated using the photolithography technique. Replica molds were used to fabricate PDMS soft microchannels while hot embossing molds were utilized to fabricate PMMA rigid microchannels (Fig. 3-1A). The photoresist was spin-coated onto 4-inch silicon wafers and subjected to prebaking at 65°C and 95°C. Ultraviolet (UV) light exposure was performed using an UV exposure system (UV-KUB 2, KLEO, France) with various photomask designs. The silicon master molds were then post-baked at 65°C and 95°C, developed using SU-8 developer, and finally hard-baked at 150°C for 30 minutes.

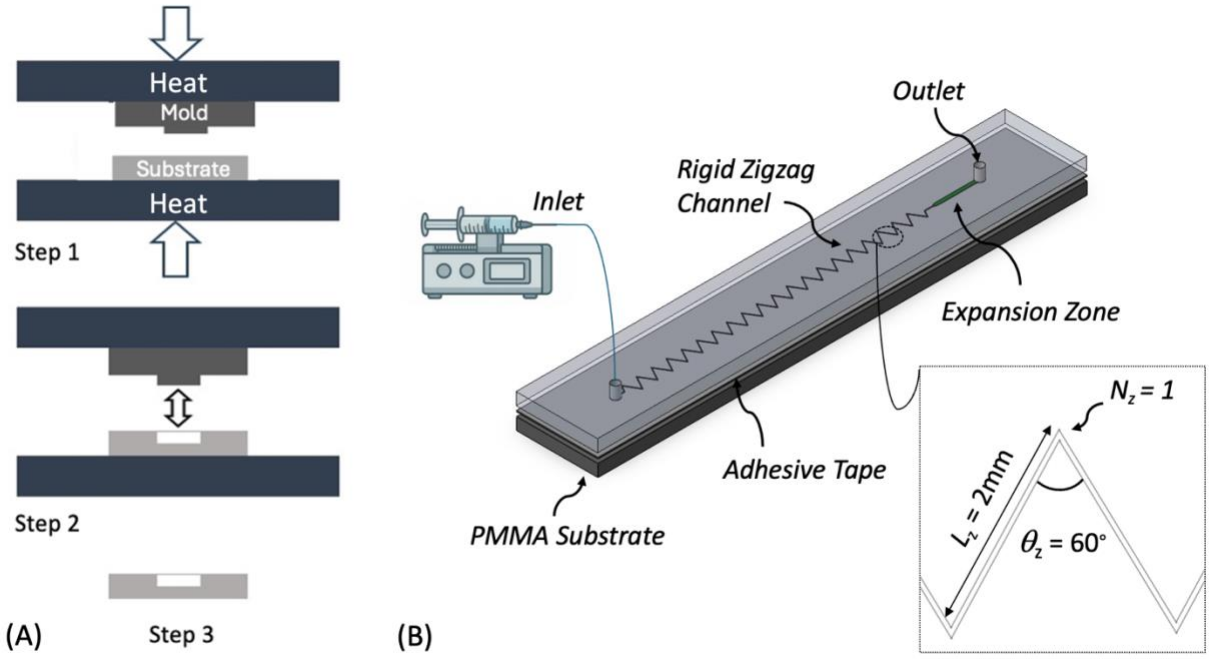

Figure 3-1 Fabrication and assembly of the zigzag microfluidic device. (A) Hot embossing fabrication process consisting of three steps: (1) Controlled pressure and temperature is applied between the silicon wafer master mold and the PMMA substrate for 5 minutes. (2) Applied pressure is released at T = 80°C. (3) The embossed PMMA substrate is demolded. (B) The assembled microfluidic device comprises three layers: the PMMA sheet with an embossed microchannel, an adhesive bonding layer, and a flat PMMA substrate. It includes a single inlet, a zigzag channel, a single outlet, and an expansion zone for particle imaging.

The microfluidic devices (Fig. 3-1B) featured one inlet, a zigzag channel with various designs, and one outlet with an expansion zone at the end (800 μm in width) for particle visualization at a lower speed [70]. Various channels were fabricated by varying key channel parameters, including channel width (w) between 40 and 50 μm and channel height (h) between 20 and 25 μm, to adjust the blockage ratio ($\beta = a_p / D_h$) for different particle sizes ranging from approximately 1 to 3.9 μm. The zigzag length (L_z) varied between 2 and 3 mm, the number of zigzags (N_z) ranging from 20 to 30 units, and zigzag angle (θ_z) maintained around 60°, resulting in total channel lengths between approximately 8 and 18 cm.

Soft PDMS and rigid PMMA microchannels were fabricated using soft lithography and hot embossing, respectively. For PDMS devices, a 10:1 mixture of PDMS prepolymer and curing agent was cast against silicon master molds, cured at 100 °C for 30 minutes, and bonded to glass slides via oxygen plasma treatment (Harrick Plasma Inc., USA). PMMA devices were fabricated using hot embossing (Hot Embosser EVG 6-inch, Austria) with 1.5 mm thick PMMA sheets, following the process illustrated in Fig. 3-1A. Unlike previous studies that relied on 3D printing [17], this work employed hot embossing as a more cost-effective, rapid, and reproducible method. Fabricating rigid devices is generally challenging, especially for small channels, as precise control of processing parameters is required to avoid defects; therefore, embossing temperature, applied force, and embossing time were systematically optimized by varying one parameter at a time until well-defined channel structures were obtained. Under optimized conditions, the PMMA substrate was heated and pressed against a patterned silicon master mold at 145 °C and 1 mbar pressure for 5 minutes, after which the mold was retracted and the applied force was released at 80

°C. The embossed substrate was then carefully demolded, laser cut into single-channel devices, and drilled with 2 mm inlet and outlet ports before final assembly by bonding to a flat PMMA sheet with adhesive double-sided tape.

3.3. Experimental setup and procedures

3.3.1. Experimental setup and procedure

PDMS and PMMA devices were used to investigate the effect of the channel rigidity. Particles with a nominal diameter of 1, 2.7 and 3.9 μm in DI water solutions were prepared and supplied through the inlet. The axial velocities tested ranged from 0.07 m s^{-1} to 0.37 m s^{-1}. An inverted microscope (Bioimager, BIM 500FL, Canada) was used at 10x magnification and videos were recorded with a high-speed camera (FASTEC, IL3, USA) at the channel expansion zone at a frame rate of 150 to 750 frames per second (FPS), depending on the axial velocity.

For a typical *E. coli* enrichment experiment, DI water spiked with GFP-labelled *E. coli* was injected into the channel inlet at a specified flow rate (e.g., 50 μL/min) using a syringe pump. To assess enrichment performance, samples were collected from both the inlet and the middle outlet, and their concentrations were measured using a QFX Fluorometer (DeNovix Inc., USA). The measured fluorescence intensities were then converted to bacterial concentrations using the established calibration curve (Fig. 3-2).

3.3.2. Quantification of E. coli concentration

To estimate *E. coli* concentration by plate counting, cultured samples (~10^8 CFU/mL) were serially diluted to as low as 10 CFU/mL. For each dilution, 50 μL was plated onto LB agar and evenly spread using a sterile L-shaped spreader. These plates were then incubated at 37 °C for 18 to 24 hours to promote visible colony formation. After incubation, colonies

were manually counted on plates that contained between 30 and 100 colonies, as this range is generally accepted for reliable quantification. Based on these counts, the number of viable bacteria in the original sample was calculated by multiplying the colony number by the corresponding dilution factor, thus providing an estimation of the initial sample concentration.

3.3.3. Establishment of a calibration curve for E. coli GFP

To establish the calibration curve for GFP *E. coli*, three independent bacterial samples were first prepared. The initial concentration of each culture was determined using the plate counting method, after which they were serially diluted to obtain a range of known concentrations. For each concentration, five replicates of 200 µL were measured for fluorescence intensity using a QFX Fluorometer. The mean intensity and standard deviation were then calculated by combining data from all three cultures. The resulting relationship between the relative fluorescence units (RFU) from the fluorometer and bacterial concentration (CFU/mL) from plate counting, used to interpolate unknown sample concentrations, is presented in Fig. 3-2.

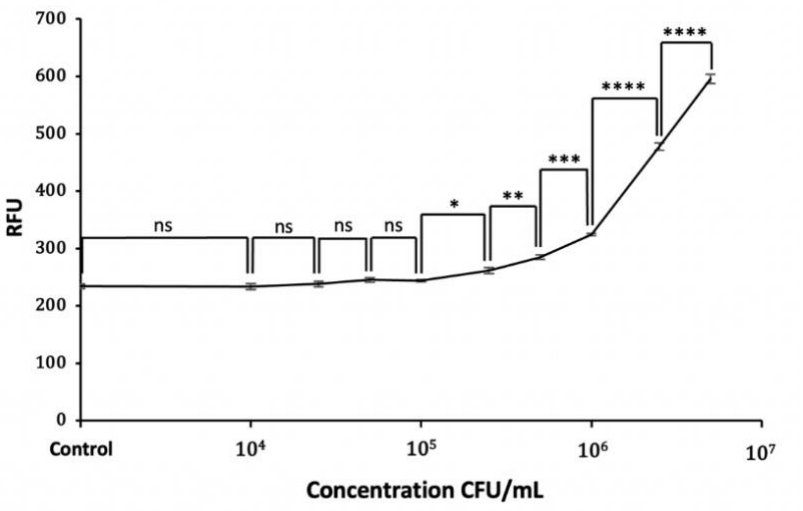

*Figure 3-2 Calibration curve of E. coli concentration based on fluorescence GFP intensity measurements using a fluorometer plotted against the actual bacterial concentrations measure via plate counting. Each data point represents the mean of fifteen replicates of three cultures, with error bars indicating the standard deviation. Significance thresholds were determined using p-values, with a threshold set at 0.05 to define statistical significance. Statistical significance is indicated by asterisks where * denotes $p < 0.05$, ** denotes $p < 0.01$, *** denotes $p < 0.001$, **** denotes $p < 0.0001$, and 'ns' indicated non- significant differences.*

3.4. Data analysis

The videos recorded from the expansion zone of the microfluidic device were analyzed using the WrMTrack plugin in ImageJ to count the particles (almost 100 particles for each video). The channel expansion width was spilt into 11 sections, and Excel was used to further analyze the data after ImageJ analysis. The normalized number of particles (NNP) and normalized channel width were plotted on x and y axes, respectively. Peak of centroid (PC) and full width at half maximum (FWHM) were calculated using OriginPro software (Origin2024b, OriginLab Corp., USA), which represented the particles' distribution and the location of the highest particles concentration, respectively [19], [71]. Furthermore, background subtraction was applied to enhance image clarity, and then frame overlapping was employed to generate a composite image that clearly visualizes both the channel boundaries and the particle trajectories within the expansion region, as shown in Fig. 3-3A and 3-3B.

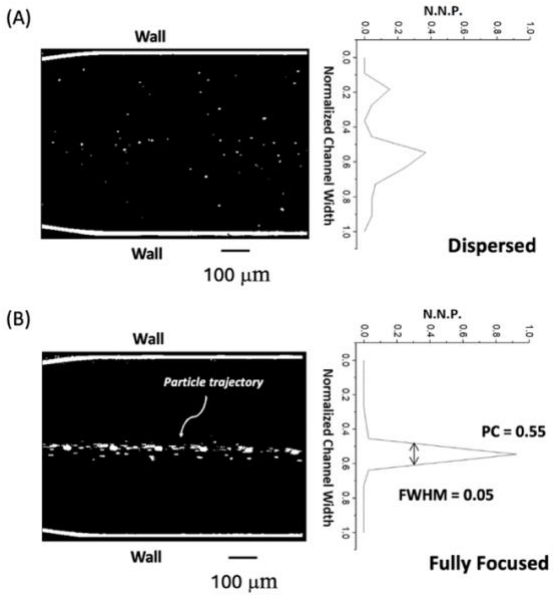

Figure 3-3 Methods used for analyzing particles distribution in microfluidic channels. Image overlaps show particles trajectory and distribution across the expansion channel width for 3.9 μm particles at V_x of (A) 0.07 m s^{-1} and (B) 0.37 m s^{-1} in a rigid zigzag microchannel. The microchannels featured L_z = 2 mm, θ_z = 60°, N_z = 20 units, w = 45 μm, and h = 25 μm. Normalized number of particles (NNP) were drawn versus the normalized channel width. FWMH indicates the full width at half maximum, representing the particles' distribution. PC shows the peak of centroid, representing the location of the highest particles concentration.

Figure 3-3A shows the dispersion of 3.9 μm particles in a rigid zigzag channel which features L_z = 2 mm, θ_z = 60°, N_z = 20 units, and a channel cross section of $w \times h$ = 45 × 25 μm^2 at an axial velocity of V_x = 0.07 m s^{-1}, while Fig. 3-3B shows the formation of a focused stream at the center in the same rigid zigzag channel at a higher axial velocity of 0.37 m s^{-1}. The focusing efficiency of the particles at the channel outlet was quantified based on Eq. 1-3 as follows: a focusing efficiency below 50% was classified as dispersed, values between 50% and 80% indicated partial focusing (FWHM above 0.12), and efficiencies above 80% were considered fully focused (FWHM equal or below 0.12).

3.5. Numerical model and governing equations

Simulations were conducted using the COMSOL Multiphysics software package and Digital Research Alliance of Canada platform for computation. The geometry of the simulated zigzag channels is illustrated schematically in Fig. 3-4. Representative experimental data were employed for model validation and further optimization of parameters. The numerical simulation process consisted of two stages. Initially, a steady-state flow solution was obtained without particle injection. Subsequently, thirty particles were randomly introduced into the flow at the channel inlet and particles trajectories were determined by solving the force balance equation governing particle motion. A time-dependent solver was used with a time step of 10^{-5} s for an axial velocity of $V_x = 0.74$ m s^{-1}. As the axial velocity increased, the time step was proportionally reduced to ensure accurate tracking of particle trajectories and to prevent numerical instability due to higher particle speeds.

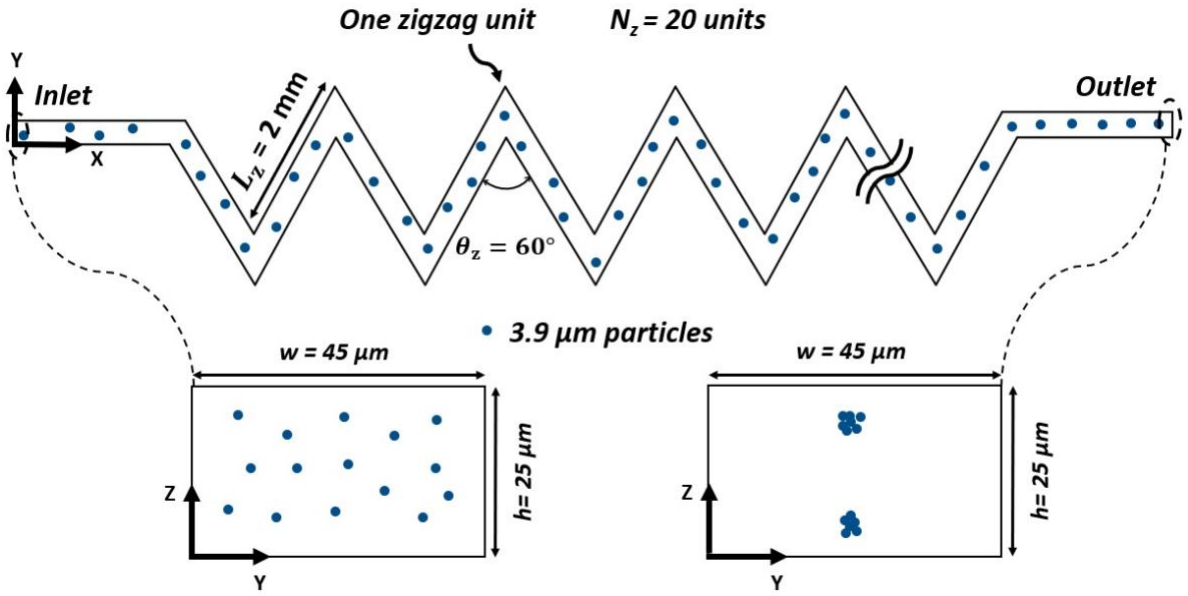

Figure 3-4 Schematic diagram of the simulated microfluidic channels with 3.9 μm particles being focused at the channel center. The simulated microchannel featured L_z = 2 mm, θ_z = 60°, N_z = 20 units, w = 45 μm, and h = 25 μm.

3.5.1. Fluid flow simulation

The laminar-flow module was employed to compute the flow distribution fields within the microchannel. This module utilizes the Navier-Stokes equations and the continuity equation as its governing principles. For the case of single-phase, Newtonian, and incompressible laminar flow, these equations can be expressed as follows:

$$r\,(\vec{u}.\nabla)\,\vec{u} = \nabla.\,[-p\boldsymbol{I} + \boldsymbol{\tau}] + \vec{F} \tag{3-4}$$

$$\nabla.\,\vec{u} = 0 \tag{3-5}$$

$$\boldsymbol{\tau} = \mu((\nabla\vec{u})^{\mathrm{T}} + \nabla\vec{u}) \tag{3-6}$$

Where velocity vector and pressure are denoted by $\vec{u}$ and p, respectively. The volumetric force vector and viscous stress tensor are denoted by $\vec{F}$ and $\boldsymbol{\tau}$, respectively. The fluid flow equations were solved using the direct MUMPS solver (multifrontal massively parallel sparse direct solver).

3.5.2. Particle tracing simulation

The Particle Tracing Module was utilized to simulate the injection and movement of microparticles within the microchannel. This module employs Lagrangian particle tracking to calculate the trajectories of individual particles. An ordinary differential equation was solved for each component of the position vector for every particle. The particle trajectories were calculated by solving Newton's second law of motion.

$$m\frac{\vec{u}_p}{\mathrm{d}t} = \vec{F}_L + \vec{F}_D \tag{3-7}$$

Where m is the particle mass and $\vec{F}_D$ is the drag force driving the particles to move along with the fluid flow (Eq. 2-2). $\vec{F}_L$ combines the shear gradient lift force, and the wall induced lift force as follows:

$$\vec{F}_L = \frac{1}{m}\rho\frac{a_p^4}{16D_h^2}\varphi(\varphi\ G_1(s) + \gamma G_2(s))\vec{n} \tag{3-8}$$

$$\varphi = \left| D(\vec{n}\cdot\nabla)\vec{u}_p \right|$$

$$\gamma = \left| \frac{D^2}{2}(\vec{n}\cdot\nabla)^2\vec{u}_p \right|$$

$$\vec{u}_p = (I - (\vec{n}\otimes\vec{n}))\vec{u}$$

In Eq. 3-8, $\vec{n}$ is the wall normal at the nearest point on the reference wall, and the symbol $\otimes$ indicates the tensor product of the $\vec{n}$ vectors. D is the distance between the channel walls, and s is the dimensionless distance from the particle to the reference wall. The functions $G_1(s)$ and $G_2(s)$ are dimensionless and were previously defined in earlier studies [72], [73]. The inertial lift force acts solely in the direction perpendicular to the fluid velocity. Additionally, the particles are assumed to be rigid spheres with small diameters relative to the channel width.

3.5.3. Boundary conditions

The boundary conditions of the microfluidic device were defined to closely replicate the experimental setup. A uniform velocity profile was applied at the inlet along the x-axis, represented as $u = U_{inlet}$. The fluid velocities in the y and z directions were assumed to be zero ($v = w = 0$). A constant pressure boundary condition with zero-gauge static pressure ($P_{outlet} = 0$) was applied at the outlet. A no-slip boundary condition was enforced on the device walls. Thirty particles were introduced randomly into the flow field at the inlet for each simulation. At each time step of the simulation, the forces acting on each particle were

calculated based on its current position and particle–particle interactions were neglected. The channel walls were modelled as rigid, and a "bounce" condition was applied for particles hitting the walls.

3.5.4. Design of experiments

A Taguchi design of experiments (DOE) was implemented using Minitab software to systematically evaluate the influence of key geometrical and flow parameters on particle focusing efficiency in zigzag microchannels using numerical modelling. Five independent variables were investigated as listed in Table 3-2: L_z, θ_z, N_z, w, and V_x, while h and a_p were held constant at 20 µm and 1 µm, respectively. The parameters were chosen to span a broad design space, while the channel height was fixed to maintain a consistently low aspect ratio and reduce the number of varying factors. Similarly, a particle size of 1 µm was selected as it closely approximates the size of bacteria, serving as a suitable surrogate. This choice allows the study to focus on the effects of geometry and flow conditions without additional variability from particle size.

Table 3-2 Parameter levels selected for the design of experiments using Taguchi model.

Parameter / Levels	L_z (mm)	θ_z (degrees)	N_z (units)	w (µm)	V_x (m s^{-1})
Level 1	1	40	10	40	0.37
Level 2	2	60	20	50	0.74
Level 3	3	80	30	60	1.11

The DOE approach significantly reduced the number of required simulations from 243 in a full factorial design (3^5 combinations) to 27 (Table 3-3). This not only minimized

computational costs and simulation time but also enabled the identification of dominant parameters influencing particle migration. This design ensured both computational feasibility and meaningful interpretation of results within the defined parameter space.

Table 3-3 All the conducted simulations based on Taguchi model.

Simulation Number	L_z (mm)	θ_z (degrees)	w (μm)	N_z (units)	V_x (m s^{-1})
1	1	40	40	10	0.37
2	1	40	40	10	0.74
3	1	40	40	10	1.11
4	1	60	50	20	0.37
5	1	60	50	20	0.74
6	1	60	50	20	1.11
7	1	80	60	30	0.37
8	1	80	60	30	0.74
9	1	80	60	30	1.11
10	2	40	50	30	0.37
11	2	40	50	30	0.74
12	2	40	50	30	1.11
13	2	60	60	10	0.37
14	2	60	60	10	0.74
15	2	60	60	10	1.11
16	2	80	40	20	0.37
17	2	80	40	20	0.74
18	2	80	40	20	1.11
19	3	40	60	20	0.37
20	3	40	60	20	0.74
21	3	40	60	20	1.11
22	3	60	40	30	0.37
23	3	60	40	30	0.74
24	3	60	40	30	1.11
25	3	80	50	10	0.37
26	3	80	50	10	0.74
27	3	80	50	10	1.11

Chapter 4: Microparticles Focusing Inside Rigid Zigzag Microchannels

This chapter presents the experimental and numerical results related to the inertial focusing of microparticles and *E. coli* in rigid zigzag microchannels, addressing both Objective 1 and Objective 2 of this thesis. First, the accuracy of the hot embossing process was assessed by comparing the fabricated channel geometries to those of the original silicon wafer molds (Section 4.1). Then, the influence of channel rigidity on particle focusing was investigated by comparing soft PDMS and rigid PMMA devices (Section 4.2). The effect of particle size on focusing efficiency and the suitability of 1 μm particles as a model for bacterial behavior were explored in Section 4.3. To improve the focusing performance of 1 μm particles and *E. coli*, a numerical model was developed and validated against experimental data (Section 4.4), and subsequently employed in a Taguchi-based parametric study to evaluate the effects of the zigzag geometry and flow

parameters on focusing behavior. Finally, the optimized channel design was experimentally validated using *E. coli*, confirming improved focusing efficiency in rigid zigzag microchannels (Section 4.5). The outcomes of this chapter directly support the design and implementation of efficient passive microfluidic devices for bacterial enrichment, which is further explored in Chapter 5.

4.1. Characterization of hot embossed zigzag microchannels

The hot embossing process was assessed by comparing the dimensions of the fabricated zigzag microchannels, i.e., width (w), height (h), zigzag length (L_z), and zigzag angle (θ_z), to those of the original silicon wafer mold (Fig. 4-1). The channel height and width of both the hot embossed channels and the molds were measured using profilometer analysis at 10x magnification (Contour GT-K, Bruker, USA), as shown in Figs. 4-1A and 4-2B. The optical images captured at 5x magnification were used to measure the zigzag length and angle (Figs. 4-1C and 4-1D).

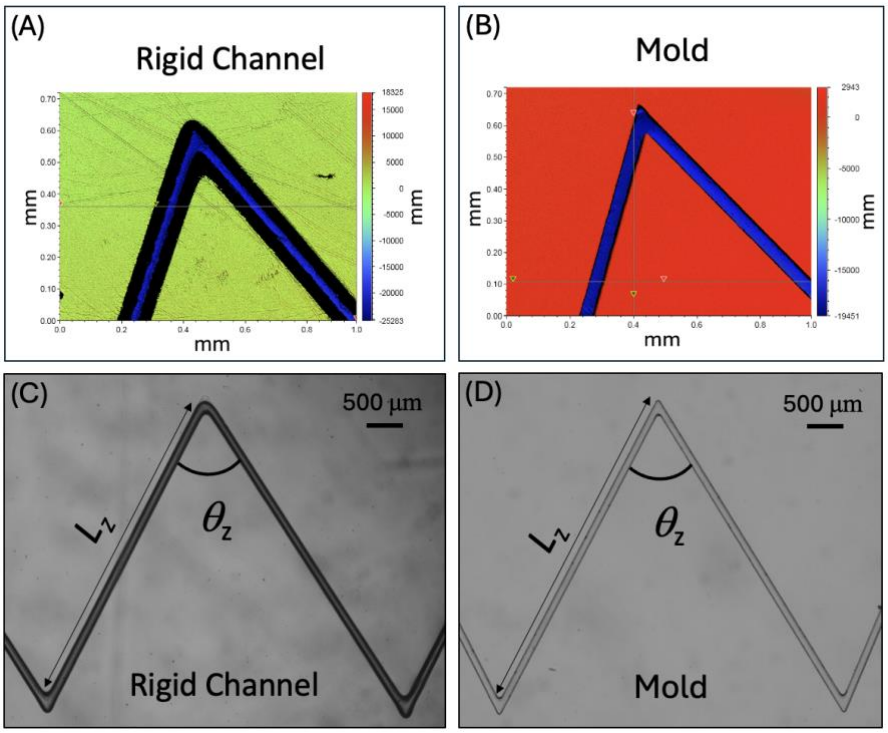

Figure 4-1 Characterization of the hot-embossed zigzag microchannels. Profilometer analysis at a zigzag channel corner at 10x magnification, with the color map indicating surface height variations for (A) the rigid zigzag channel and (B) the mold. Optical images at 5x magnification of (C) the hot-embossed microchannel and (D) the mold.

The hot embossed channels exhibited dimensions of $L_z = 1.97 \pm 0.01$ mm, $w = 47 \pm 4$ μm, $h = 25 \pm 3.49$ μm, and $\theta_z = 57.67 \pm 2.53°$, compared to $L_z = 2.14 \pm 0.041$ mm, $w = 43.5 \pm 1.3$ μm, $h = 22 \pm 0.6$ μm, and $\theta_z = 56.45 \pm 2.23°$ for the mold. The calculated percentage deviations were 7.9% for L_z , 8% for w, 13.6% for h, and 2.2% for θ_z. As the errors for most parameters are around or below 10%, the dimensional accuracy of the hot embossing process is considered acceptable. Based on these results, the same fabrication steps and configuration were applied for all subsequent channels.

4.2. Effect of channel rigidity on particle focusing in zigzag channels

To evaluate the effect of channel rigidity on focusing efficiency of particles, two similar zigzag microchannels were fabricated, i.e., one rigid device made of PMMA, and one soft device made of PDMS. Both channels featured $L_z = 2$ mm, $\theta_z = 60°$, and $N_z = 20$ units, consistent with designs reported in the literature [11], [17]. These channels were designed with a low aspect ratio, which gives the optimum focusing of particles at the channel center [14], with a cross section of $w \times h = 45 \times 25$ μm^2 to achieve a blockage ratio ($\beta = a_p / D_h$) of 0.035 for 1 μm particles. Particles with a diameter of 1 μm were introduced and tested at various axial velocities of $V_x = 0.07$ - 0.37 m s^{-1} (flow rates $Q = 5$ - 25 μL/min, $Re = 2.35$ - 11.75, $Re_p = 0.09$ - 0.45). The NNP was plotted against the normalized channel width for rigid and soft channels, as shown in Fig. 4-2.

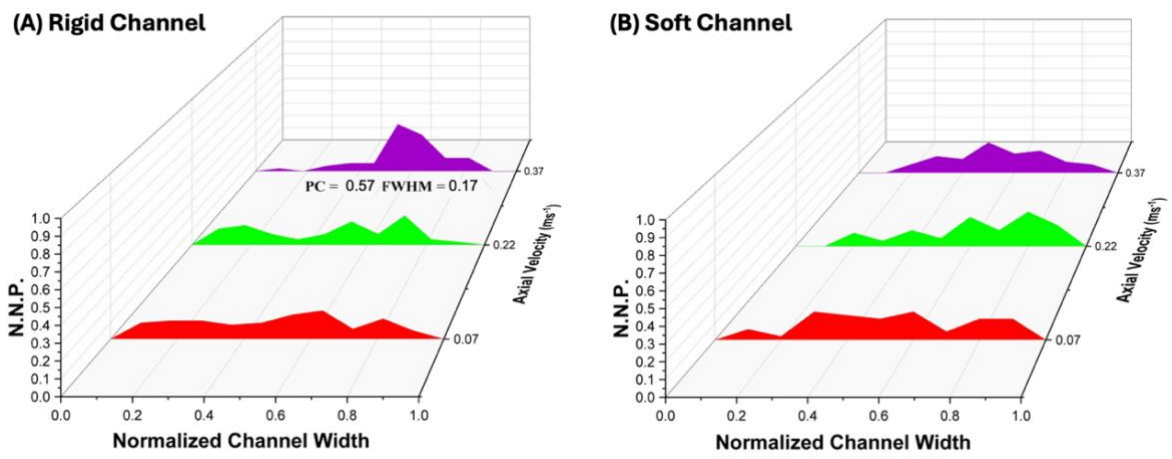

Figure 4-2 Effect of channel rigidity on particles distribution. The NNP is plotted alongside the normalized channel width for 1 μm particles in (A) a rigid PMMA zigzag channel and (B) a soft PDMS zigzag channel, under axial velocities of V_x = 0.07, 0.22, and 0.37 m s^{-1}. Both microchannels featured L_z = 2 mm, θ_z = 60°, N_z = 20 units, w = 45 μm, and h = 25 μm.

Fig. 4-2A demonstrates that particle focusing in the rigid zigzag microchannel improved with increasing the axial velocity. At lower velocities (V_x = 0.07 and 0.22 m s^{-1}), particles remained fully dispersed across the channel width. However, at V_x = 0.37 m s^{-1}, particles began to partially focus near the channel center, driven by enhanced inertial lift and Dean drag forces. This was reflected by PC of 0.56 and a FWHM of 0.17. In contrast, the soft PDMS channel (Fig. 4-2B) exhibited dispersed particle distributions at all tested velocities. This diapered focusing is attributed to the elastic expansion of soft channels under flow, which reduces the effective inertial forces acting on the particles and disrupts the balance required for focusing [17].

Overall, the rigid PMMA device achieved partial focusing at Re = 11.75 and despite a low blockage ratio (β = 0.035), whereas the soft PDMS channel failed to achieve any focusing, consistent with prior studies indicating that soft devices typically require a β > 0.07 [14]. Based on these results, rigid channels were used for all subsequent experiments.

4.3. Effect of particle size to mimic *E. coli* bacteria focusing behavior

To investigate the effect of particle size on the focusing efficiency of particles and identify the size that best mimic the hydrodynamic focusing of bacteria, experiments were conducted using rigid zigzag microchannels with $L_z = 2$ mm, $\theta_z = 60°$, $N_z = 20$ units, $w = 45$ µm, and $h = 25$ µm. Particles with diameters of 1 µm ($\beta = 0.035$), 2.7 µm ($\beta = 0.083$), and 3.9 µm ($\beta = 0.12$), as well as *E. coli*, were tested. Experiments were conducted at $V_x = 0.37$ m s^{-1} which corresponds to a Q of 25 µL/min, Re of 11.75, and Re_p of 0.45, 1.08, and 1.58 for the 1, 2.7, and 3.9 µm particles, respectively. The NNP against the normalized channel width was plotted as shown in Fig. 4-3.

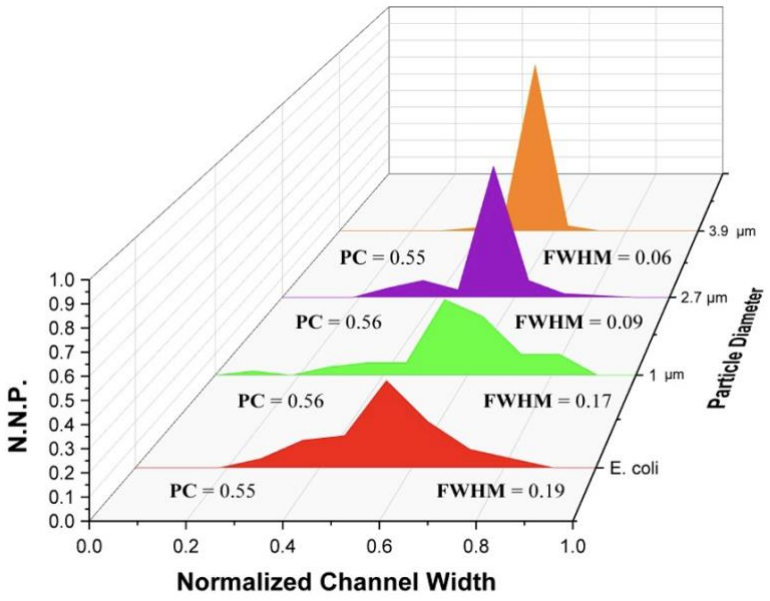

Figure 4-3 Effect of particle size on particles distribution in a rigid zigzag channel. The NNP is plotted alongside the normalized channel width at $V_x = 0.37$ m s^{-1} for E. coli, 1 µm, 2.7 µm, and 3.9 µm particles. The used microchannel in these experiments featured $L_z = 2$ mm, $\theta_z = 60°$, $N_z = 20$ units, $w = 45$ µm, and $h = 25$ µm.

All particle sizes exhibited nearly similar PC around 0.55 and the FWHM increased as particle size decreased. Particles with a diameter of 3.9 µm and 2.7 µm were fully focused with FWHM =

0.06 and 0.09, respectively, with 3.9 μm demonstrating enhanced focusing. The 1 μm particles and *E. coli* showed similar behavior as they were partially focused with FWHM = 0.17 and 0.19, respectively. It is worth noting that the comparable focusing behavior observed for 1 μm particles and *E. coli* is consistent with prior findings that *E. coli* exhibit focusing patterns similar to those of 1 μm particles [74].

Generally, the variation in particle focusing behavior can be attributed to the balance between inertial lift forces (Eq. 2-1) and Dean drag forces (Eq. 2-2). Larger particles, such as those with diameters of 2.7 and 3.9 μm, focus more rapidly than smaller particles (1 μm) and *E. coli*, primarily due to the stronger inertial and drag forces acting on them, as previously reported for microparticles [17]. In addition, the zigzag channel parameters can play a critical role in determining the focusing behavior of particles, as demonstrated in studies on various microchannel geometries [13], [49], [68].

4.4. Numerical modelling and particle focusing optimization

Overall, optimizing the zigzag channel parameters is important for improving the focusing efficiency of 1 μm particles and *E. coli*, and further investigation of higher axial velocities is necessary to enhance the device throughput. Therefore, a numerical parametric study is needed to explore of a wide design space with reduced time, cost, and fabrication efforts, enabling the visualization of particle trajectories under high axial flow velocities and the identification of optimal channel parameters. Therefore, a numerical model was built and verified by investigating its mesh independency and fluid flow characteristics (section 4.4.1), then the model was validated against the above experimental results (section 4.4.2). Lastly, the validated model was used to

conduct a parametric study to investigate the effects of different channel parameters and axial flow velocity (as described in Table 3-2) on the focusing behavior of 1 μm particles (Section 4.4.3).

4.4.1. Mesh independency study

To ensure mesh independence while minimizing computational cost, the 3D geometry of the zigzag microchannel (Fig. 3-4) was discretized using a combination of tetrahedral, prism, and pyramid elements. Several mesh numbers were considered, ranging from 3.1×10^5 to 3.2×10^6 elements. COMSOL's automatic mesh refinement was applied near the channel corners to accurately capture velocity gradients and flow vortices in these critical regions. Since Dean flow has a significant impact on particle migration at the zigzag corners, mesh verification was focused on these areas. As shown in Fig. 4-4A, velocity profiles were examined at three representative cross-sections, i.e., upstream, within, and downstream of a zigzag corner, under an inlet velocity of 0.74 m s^{-1} (Figs. 4-4 B–D). Upstream of the zigzag corner, the flow stabilized into a normal parabolic velocity profile with a central peak, while within the corner and downstream, the velocity profiles exhibited asymmetric peaks near the sidewalls due to the Dean flow effect. As the mesh was refined, variations in velocity magnitude progressively decreased, and convergence was achieved beyond 907,730 elements with fully developed velocity fields. At this resolution, further refinement resulted in less than 0.1% change in the average axial velocity, confirming mesh independence. Therefore, the mesh containing 907,730 elements was adopted for all subsequent simulations to ensure both accuracy and computational efficiency.

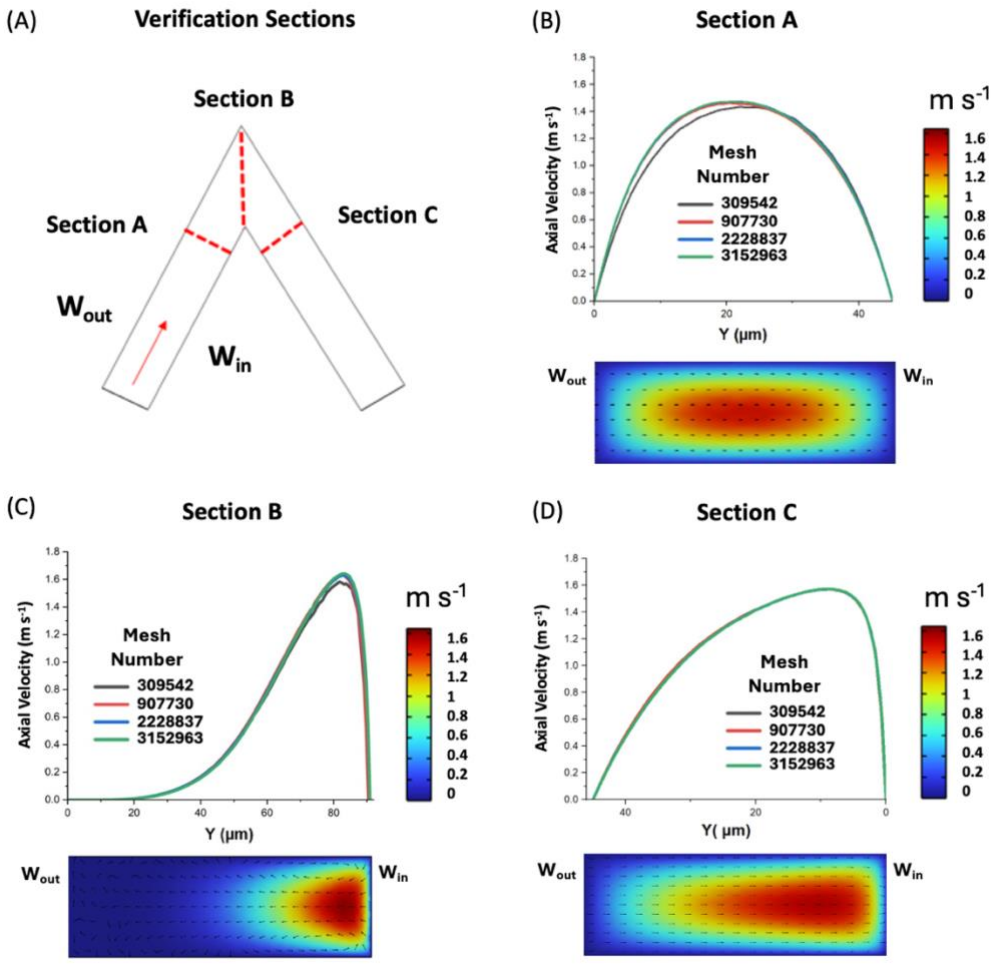

Figure 4-4 Numerical simulation of water flow in a zigzag microchannel. (A) Schematic illustration showing the selected cross-sectional planes for model verification. Axial velocity profile at the middle of the channel cross section at an inlet average velocity of 0.74 m s^{-1} of (B) Section A, (C) Section B, and (D) Section C. The simulated microchannel featured L_z = 2 mm, θ_z = 60°, N_z = 20 units, w = 45 μm, and h = 25 μm.

4.4.2. Model validation

The predictive capability of the model for particle trajectories in Newtonian flow (water) within the zigzag channel (Fig. 3-4) was evaluated by comparing its results with previously presented experimental data (Figs. 4-2A and 4-3). The NNP across the channel width was plotted to compare the focusing behavior under the conditions described in Section 3.4. Fig. 4-5 presents the numerical and experimental focusing results for different particle sizes.

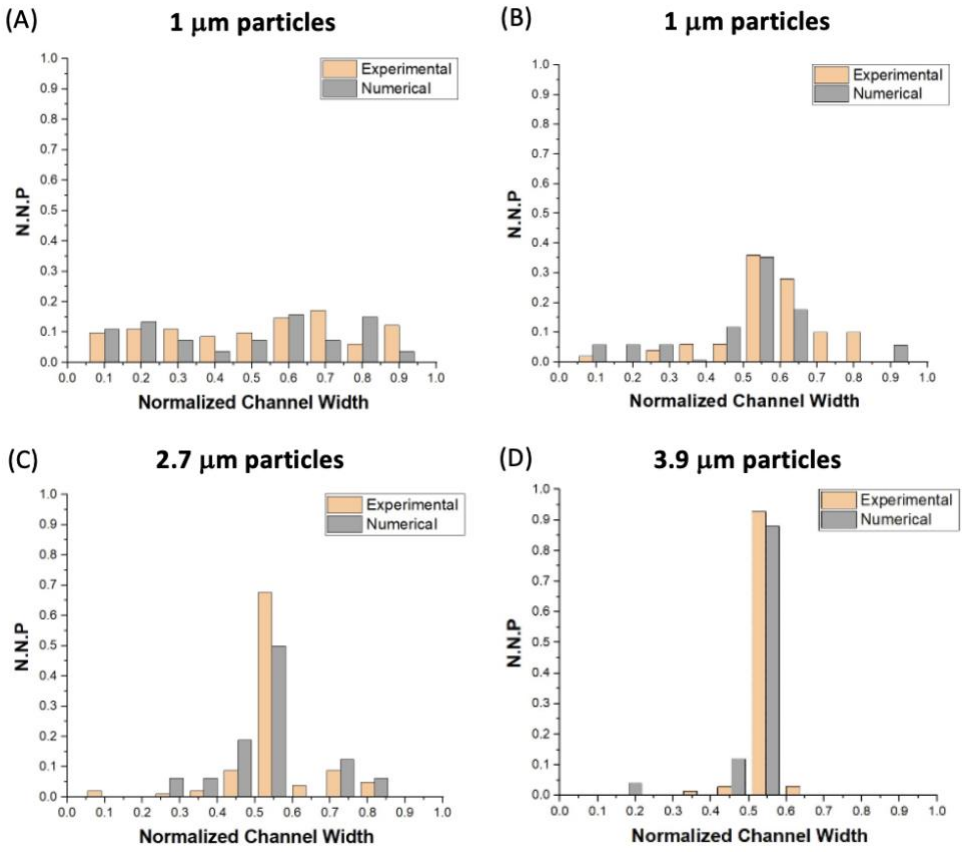

Figure 4-5 Comparison of the experimental and numerical results for model validation. (A) 1 µm particles at V_x = 0.07 m s^{-1} (dispersed). (B) 1 µm particles at 0.37 m s^{-1} (partially focused). (C) 2.7 µm particles at 0.37 m s^{-1} (fully focused). (D) 3.9 µm particles at 0.37 m s^{-1} (fully focused). The simulated microchannel in (A-D) featured L_z = 2 mm, θ_z = 60°, N_z = 20 units, w = 45 µm, and h = 25 µm.

As observed in Fig. 4-2A, 1 µm particles are randomly distributed at V_x = 0.07 in experiments as well as in our model, as shown in Fig. 4-5A. Furthermore, At V_x = 0.37 m s^{-1}, partially focusing behavior was observed for 1 µm particles in experiments and simulations (Fig. 4-5B) which confirms the ability of the model to capture the effect of axial velocity on particle focusing. Morover, fully focused behavior for 2.7 and 3.9 µm particles was observed in both setups (Fig. 4-5C and 4-5D), with 3.9 µm particles exhibiting enhanced focusing. This confirms that the model accurately captures the influence of particle size on particle focusing. Overall, there is strong agreement between the simulation

and experimental results, demonstrating that the model accurately predicts both particle dispersion and focusing across varying flow conditions.

4.4.3. Parametric numerical study on microparticle focusing in zigzag channel

The parameter levels presented in Table 3-2 were selected for the design of experiments using Taguchi model to investigate the effect of L_z, θ_z, N_z, w, and V_x on particle focusing. A total of 27 simulations were conducted (Table 3-3), and the data were analyzed using Minitab software. In this analysis, the focusing efficiency was used as the response signal, and the mean focusing efficiency for each parameter level was calculated by averaging the response values from all trials involving that level. The results are plotted in Fig. 4-6 and the effect of each parameter is explained in the subsections below.

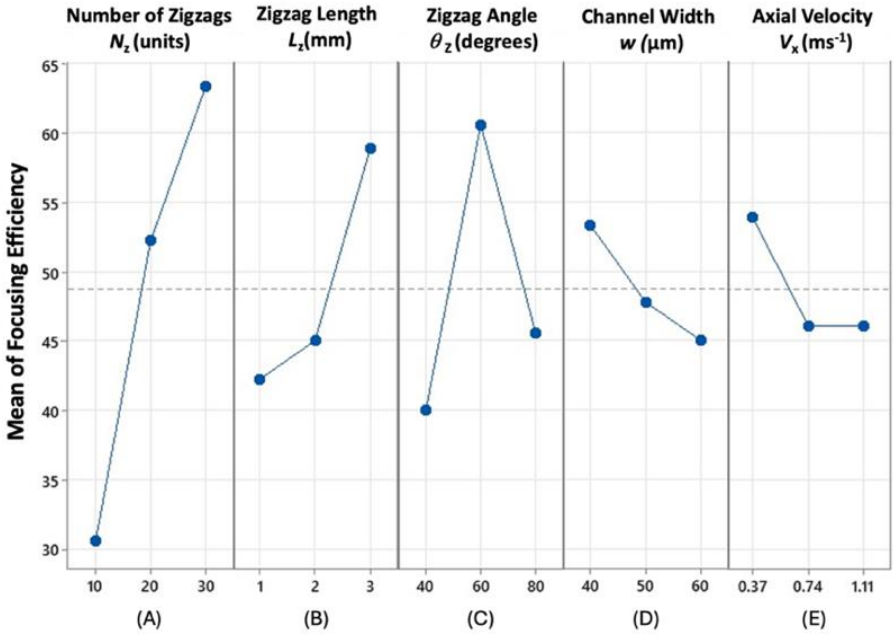

Figure 4-6 Results of the Taguchi parametric study showing the mean focusing efficiency versus (A) number of zigzags (N_z), (B) zigzag length (L_z), (C) zigzag angle (θ_z), (D) channel width (w), and (E) axial velocity (V_x).

4.4.3.1. Effect of number of zigzags (N_z) and zigzag length (L_z)

Increasing the number of zigzags significantly enhanced the focusing efficiency and had the most pronounced effect, as shown in Fig. 4-6A. Similarly, increasing the zigzag length led to improved focusing efficiency (Fig. 4-6B). This enhancement can be attributed to two main factors. First, the Dean drag force generated at the zigzag corners acts repeatedly on the particles, helping to balance the inertial lift forces and promote lateral migration. Second, particle focusing is a length-dependent process as smaller particles (e.g., 1 μm) require a longer distance to reach their equilibrium positions compared to larger particles (e.g. 2.7 and 3.9 μm). Therefore, the observed improvements in focusing efficiency for both parameters result from the combined effects of repeated Dean force application at the corners and the overall increase in channel length. These findings are consistent with previous studies reporting that longer channel lengths enhance focusing performance in other geometries, such as serpentine and square-wave designs [13], [69].

Generally, it is worth noting that, based on the numerically observed particle trajectories, focusing of 1 μm particles in zigzag microchannels progresses through four distinct stages along the channel length. Initially, particles are dispersed (Fig. 4-7A) and then they form two distinct focusing peaks after a certain length (Fig. 4-7B), which then merge into a single peak near the center of the channel with a partially focused behavior (Fig. 4-7C). Furthermore, as particles continue to travel along the channel, their bandwidth gradually decreases, resulting in further enhanced focusing until they become fully focused (Fig. 4-7D).

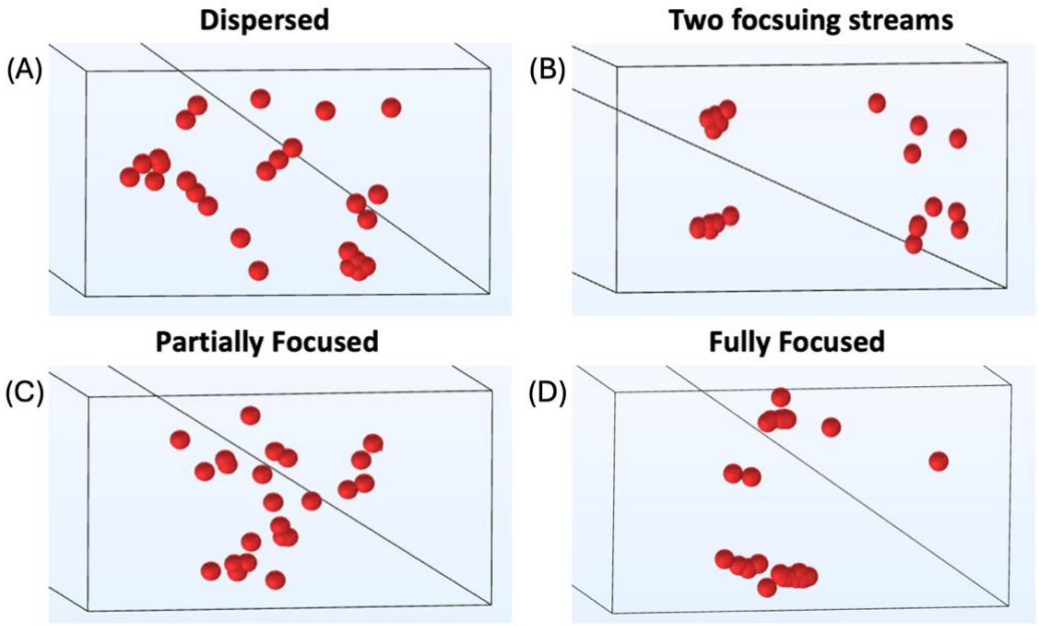

Figure 4-7 Focusing behavior of 1 μm particles along the zigzag channel length. (A) Dispersed distribution. (B) Two focusing streams. (C) Partial focusing behavior. (D) Fully Focusing behavior. The simulated zigzag channel featured L_z = 3 mm, θ_z = 60°, N_z = 30 units, w = 40 μm, and h = 20 μm.

4.4.3.2. Effect of zigzag angle (θ_z)

The results revealed that the focusing efficiency increased as the zigzag angle increased from 40° to 60°, then declined at 80°, as shown in Fig. 4-6C. To better understand this trend, velocity contours and velocity vectors at the zigzag corners were plotted for a range of angles: 15°, 40°, 60°, 80°, and 150° (Fig. 4-8).

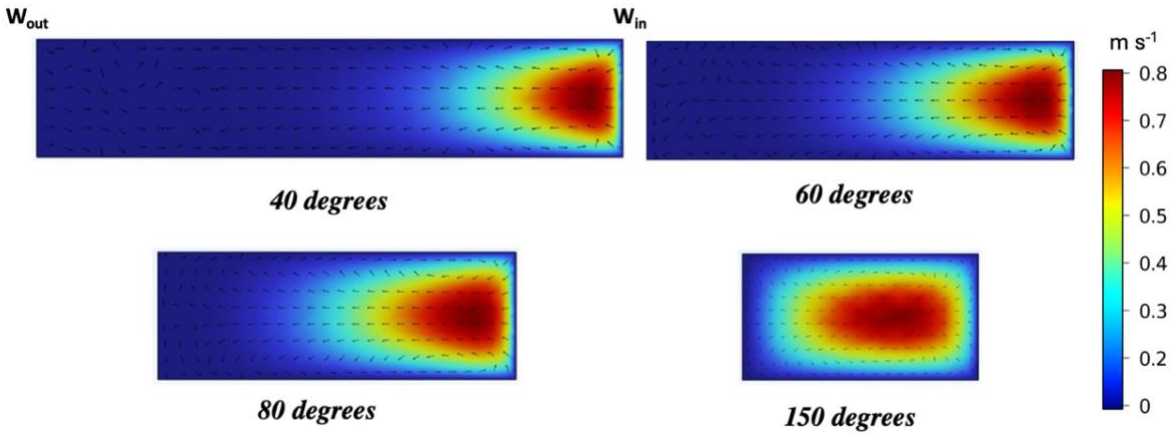

Figure 4-8 Velocity contours and velocity vectors for different angles at V_x = 0.37 m s^{-1}. The simulated microchannel featured w = 40 µm and h = 20 µm.

For each zigzag angle, the velocity profile at the middle of the cross-section of the zigzag corner (Section B in Fig. 4-4A) was plotted at an inlet axial velocity of 0.37 m s^{-1}, with the channel width and height fixed at 40 µm and 20 µm, respectively (Fig. 4-9A). Furthermore, for quantitative comparison, the average velocity vector magnitude of each cross-section of each angle was calculated and defined as the Dean drag velocity (V_{De}) of that angle. These values were then plotted against the zigzag angle, alongside the velocity dead zone (VDZ), defined as the fraction of the cross-section where axial velocity dropped below 95% of the maximum value (Fig. 4-9B).

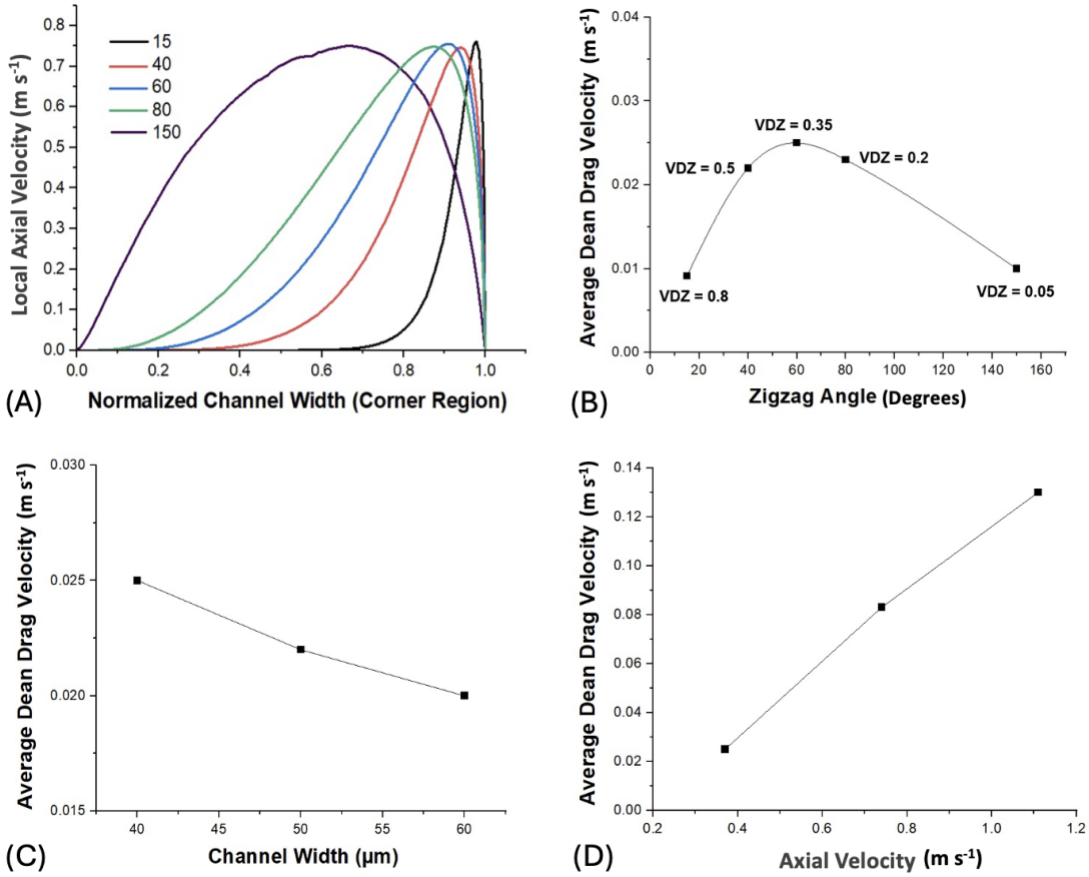

Figure 4-9 Dean drag velocity analysis under various conditions. (A) Velocity profile plotted for different zigzag angles at an inlet axial velocity of 0.37 m s^{-1} in a zigzag channel with a cross-section of w × h = 40 × 20 μm². (B) Average Dean drag velocity versus zigzag angle at V_x = 0.37 m s^{-1}, in a zigzag channel with a cross-section of w × h = 40 × 20 μm². (C) Average Dean drag velocity versus channel width at V_x = 0.37 m s^{-1}, with a fixed θ_z = 60° and h = 20 μm. (D) Average Dean drag velocity versus axial velocity, using a zigzag channel with θ_z = 60° and a cross-section of w × h = 40 × 20 μm².

Generally, the trend of V_{De} closely aligned with the focusing efficiency trend from the Taguchi analysis, both peaking at 60°, confirming the direct effect of Dean flow in enhancing particle focusing. This behavior can be interpreted based on the curvature-induced flow dynamics. In a straight channel, no secondary flow is generated (V_{De} = 0). As the corner angle reduces from 180°

to 150°, curvature begins to induce Dean vortices, with V_{De} reaching 0.01 m s^{-1} and VDZ around 0.05. Further decreasing the angle to 60° intensifies the lateral shift in the velocity profile, which enhances the pressure gradient across the channel width. This amplifies the Dean flow, resulting in a peak V_{De} of 0.025 m s^{-1} and VDZ of 0.35. Additionally, the zigzag corners not only generated Dean vortices but also contributed to the enhanced lift forces acting on the particles due to the higher velocity gradient at these zigzag corners which enhanced the shear gradient lift force, thereby accelerating lateral particle migration, an effect that is most pronounced at a 60° angle. However, reducing the angle below 60° had a detrimental effect. At 40° and 15°, a substantial low-velocity region was observed near the corner, with VDZ increasing up to 0.8. This suppressed vortex formation and reduced the cross-sectional pressure gradient, thereby weakening both Dean drag and shear gradient lift forces. As a result, the overall particle focusing efficiency declined at these smaller angles.

4.4.3.3. Effect of channel width (w)

Increasing the channel width led to a decrease in focusing efficiency (Fig. 4-6D). This trend is further supported by Fig. 4-9C, which shows the relationship between V_{De} and channel width with fixed V_x = 0.37 m s^{-1}, θ_z = 60°, and h = 20 µm. At w = 40 µm, V_{De} was 0.025 m s^{-1}, and it slightly decreased to 0.02 m s^{-1} as the width increased to 60 µm. The observed decline in V_{De} with increasing width closely aligns with the reduction in focusing efficiency reported in the Taguchi analysis. This behavior can be explained by two main factors. First, a wider channel provides more space for the Dean vortices to develop, which leads to a dispersion of their strength and a reduction in their effective drag force on the particles. Second, increasing the channel width reduces the inertial forces acting on the particles, thereby diminishing their lateral migration and focusing efficiency. As a result, a channel width of 40 µm, with an aspect ratio of 0.5, was found to be the

best configuration for focusing 1 µm particles, maintaining strong Dean drag and inertial lift forces. This is consistent with findings reported for other geometries in previous studies, as a channel with an aspect ratio of 0.5 was considered optimal [46].

4.4.3.4. Effect of axial velocity (V_x)

Increasing the axial velocity from 0.37 m s^{-1} to 0.74 m s^{-1} disrupted the focusing behavior, resulting in a reduction in focusing efficiency. Further increases beyond 0.74 m s^{-1} showed no significant improvement in focusing performance (Fig. 4-6E). Fig. 4-9D shows the relationship between V_{De} and V_x in a zigzag channel with fixed $\theta_z = 60°$, $w = 40$ µm, and $h = 20$ µm. Generally, V_{De} increased with increasing V_x, reaching 0.025 m s^{-1} at V_x = 0.37 m s^{-1} and 0.126 m s^{-1} at V_x = 1.11 m s^{-1}.

At moderate axial velocities, particles focus at the center of the channel due to a balance between F_S and F_D at that position (Fig. 4-10A). However, as the axial velocity increases, the Dean drag force becomes dominant, shifting the equilibrium position toward the sidewalls, where it balances with F_W and F_S (Fig. 4-10B).

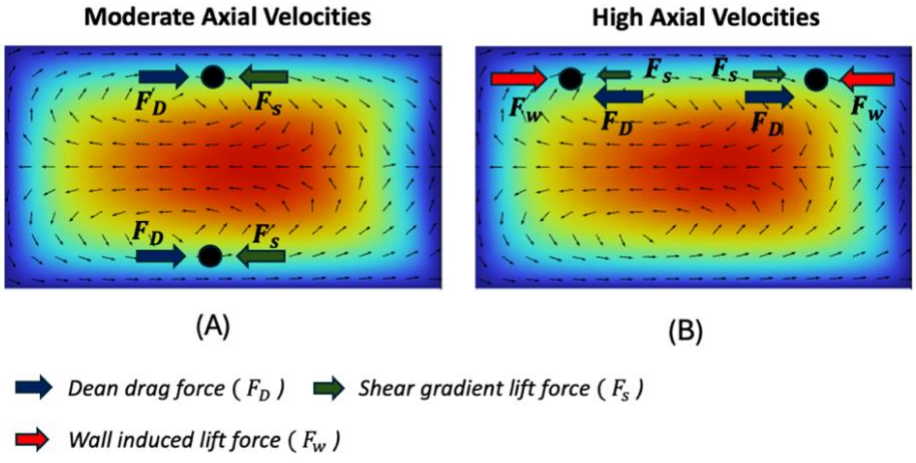

Figure 4-10 A schematic illustration of equilibrium positions of 1 µm particles, with the acting forces shown for (A) moderate axial velocities and (B) high axial velocities.

Notably, the sidewall focusing of particles observed at axial velocities above 0.37 m s^{-1} is consistent with previous reports on 1 μm particles behavior at high axial velocities in zigzag microchannels [17]. It is worth noting that increasing the channel length allows the two focused streams to eventually merge into a single central stream. Therefore, at axial velocities exceeding 0.37 m s^{-1}, a longer channel is required to achieve efficient particle focusing.

In conclusion, Dean flow enhances particle focusing by balancing inertial lift forces. However, increasing the Dean drag velocity beyond 0.025 m s^{-1} (V_x = 0.37 m s^{-1}) leads to particles dispersion and migration toward the sidewalls, necessitating longer channel length to achieve single focusing stream.

4.5. Proof of concept *E. coli* focusing using the optimum device

As previously shown in Fig. 4-3, *E. coli* exhibited similar focusing behavior to 1 μm particles, making it a suitable biological model for validation after channel optimization. Based on the numerical results presented in Section 4.4, the optimized design for focusing 1 μm particles was identified as a rigid zigzag microchannel with L_z = 3 mm, θ_z = 60°, N_z = 30 units, w = 40 μm, and h = 20 μm. Using this design, microchannels were fabricated and experimentally tested with *E. coli* at an axial velocity of V_x = 0.37 m s^{-1} (Fig 4-11). Figure 4-11A shows the overlapped trajectories of *E. coli* in the expansion zone, while Fig. 4-11B compares the distribution of *E. coli* across the channel width before and after optimization. Before optimization, particles exhibited partial focusing with a FWHM of 0.19. After optimization, they became more tightly focused at the center of the channel, with a FWHM of 0.12, closely matching the numerical result of 0.1. This improvement is

primarily attributed to the increased channel length, achieved by extending both L_z and N_z, which provides a longer focusing path and allows particles more length to migrate toward their equilibrium positions and undergo repeated interactions at the zigzag corners.

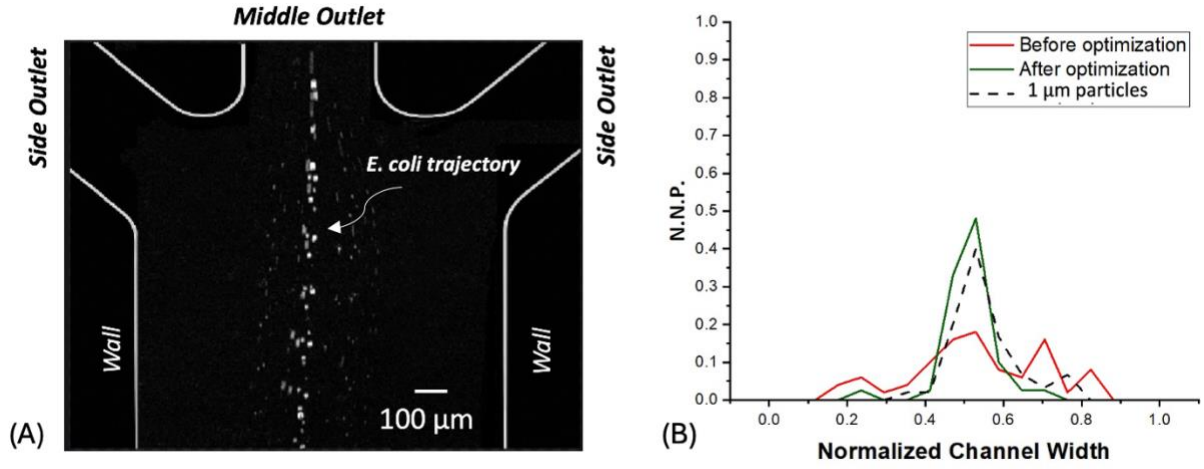

Figure 4-11 Experimental validation of E. coli focusing in the optimized channel (A) Overlapped images of E. coli trajectory at the channel expansion zone in the optimized channel at V_x = 0.37 m s^{-1} (B) Distribution of E. coli across the channel width before and after optimization, compared with the numerical results. The zigzag channel featured L_z = 3 mm, θ_z = 60°, N_z = 30 units, w = 40 µm, and h = 20 µm.

Generally, these results confirm a strong agreement between experimental observations and numerical predictions, validating the accuracy of the simulation in capturing the focusing dynamics. Moreover, compared to previous studies where *E. coli* focused near the sidewalls [11], our results demonstrate a central focusing behavior for bacteria in a low aspect ratio rigid zigzag microchannel, highlighting the device's strong potential for bacterial enrichment applications with high enrichment efficiency.

Concluding Remarks

In this chapter, the inertial focusing behavior of microparticles with diameters of 1, 2.7, and 3.9 μm, as well as *E. coli* bacteria, was investigated in rigid zigzag microchannels. The focusing patterns under the influence of particle size, channel rigidity, zigzag geometry parameters, and axial velocity were experimentally and numerically investigated. Experimental results showed that larger particles (2.7 and 3.9 μm) achieved fully focused distributions at an axial flow velocity of 0.37 m s^{-1}, while smaller particles such as 1 μm and *E. coli* showed partial focusing, indicating the need for further optimization. To address this, a numerical parametric study was conducted employing a Taguchi Design of Experiments (DOE) approach to systematically investigate the effects of zigzag length, number of zigzags, zigzag angle, channel width, and axial velocity on the focusing efficiency. The analysis revealed that increasing the number of zigzags and the zigzag length had the most pronounced positive effects on focusing efficiency by increasing the channel length available for particle migration, while increasing the channel width and axial velocity disrupted focusing behavior. Furthermore, a zigzag angle of 60° provided the most effective focusing due to the enhanced Dean flow it generated. The optimum channel design identified through this study achieved focusing efficiencies exceeding 80% for 1 μm particles at 0.37 m s^{-1}, consistent with experimental validation for both 1 μm particles and *E. coli*. The combination of the rigid channel material and the optimized zigzag geometry is considered responsible for the efficient focusing performance observed in this study. Overall, the optimized rigid zigzag microchannel here provides a promising platform for efficient focusing and enrichment of micrometer-sized particles and *E. coli* bacteria, which is further discussed in Chapter 5.

Chapter 5: *Escherichia coli* Enrichment using Inertial Focusing in Rigid Zigzag Microchannels

This chapter presents the experimental validation of the optimized rigid zigzag microchannel for the enrichment of *E. coli* bacteria, addressing Objective 3 of this thesis. Section 5.1 investigates the effect of flow rate on the inertial focusing of 1 µm particles used as surrogates for *E. coli*. Section 5.2 evaluates the enrichment performance of both 1 µm particles and *E. coli* under the identified optimal flow condition. The impact of inlet bacterial concentration on the enrichment factor is examined in Section 5.3, which also introduces a multi-pass enrichment strategy for handling low-abundance samples. Finally, Section 5.4 examines the post-enrichment viability of *E. coli*. This structured investigation aims to demonstrate the device's suitability as an efficient preconcentration module for point-of-care (PoC) diagnostic applications.

5.1. Effect of flow rate on particle focusing

Using the optimized zigzag microchannel shown in Fig. 5-1, the initial objective was to determine the most efficient flow rate for focusing 1 μm particles, used as surrogates for *E. coli*.

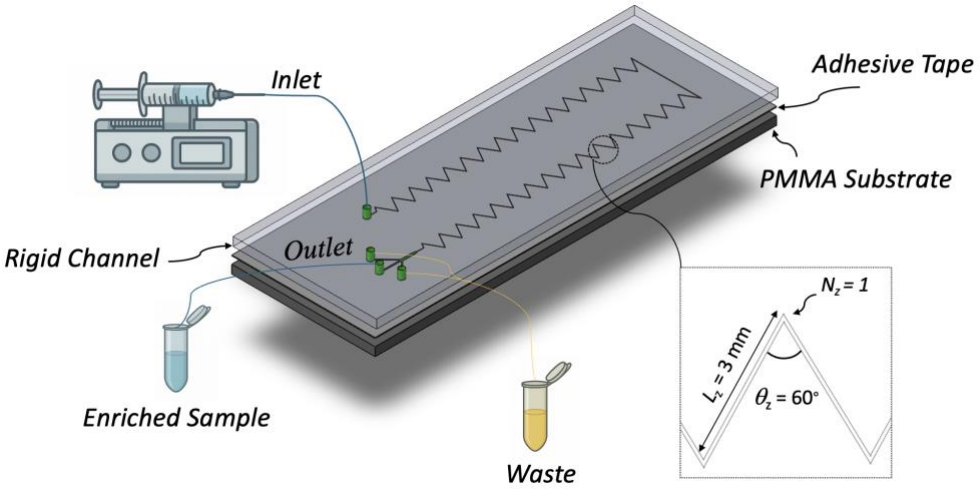

Figure 5-1 The assembled microfluidic device comprises three layers: a PMMA sheet with an embossed microchannel, an adhesive bonding layer, and a PMMA substrate. The device included a single inlet, three outlets, and an expansion zone for particle imaging. The optimized channel featured L_z = 3 mm, θ_z = 60°, N_z = 30 units, w = 40 μm, and h = 20 μm.

The optimized zigzag microchannel was used and particles with a diameter of 1 μm (β = 0.042) were introduced and tested under various flow rates of Q = 5 - 50 μL/min (V_x = 0.104 - 1.04 m s^{-1}, Re = 2.77 - 27.7, and Re_p = 0.116 - 1.16) at a concentration of 2.5 × 10^5/mL. This concentration was chosen to avoid the high particle–particle interactions that occur at higher concentrations [13]. The NNP was plotted against the normalized channel width as shown in Fig. 5-2. As discussed in Section 3.4, focusing was considered acceptable when PC was around 0.5 and FWHM was equal or below 0.12. These criteria indicate that over 80% of the particles were concentrated within a narrow region (approximately ±10%

of the channel width) around the centerline. This ensured effective particle capture, as the middle outlet width was designed to cover 30% of the main channel width, providing a sufficient margin for collecting the focused particle stream.

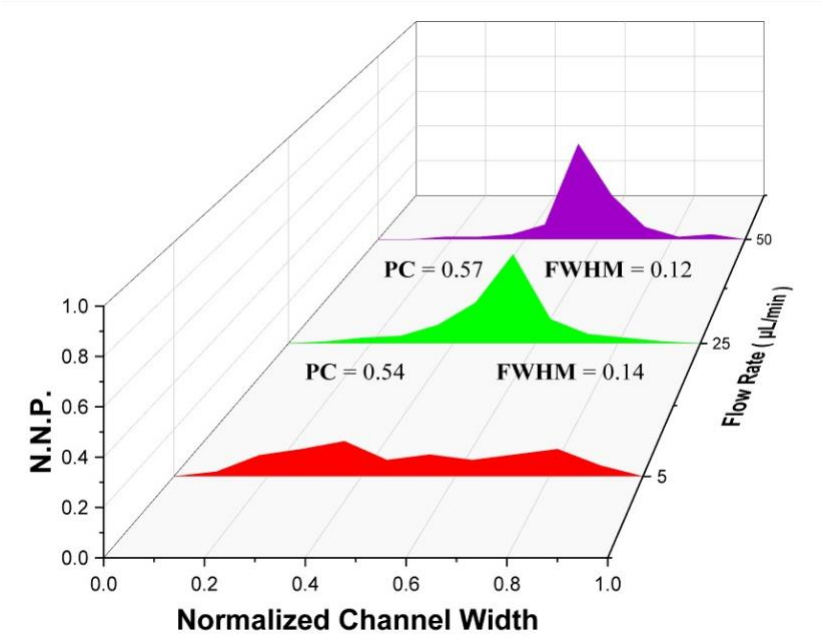

Figure 5-2 Effect of flow rate on the NNP alongside the normalized channel width for 1 μm particles in rigid zigzag channels.

Generally, as the flow rate increased from 5 to 50 μL/min, particles exhibited progressively enhanced focusing behavior. At a low flow rate of Q = 5 μL/min, the particles remained dispersed. At Q = 25 μL/min, focusing was observed, with a slight improvement at 50 μL/min, where a fully focused stream of particles appeared at the center of the channel, with PC = 0.57 and FWHM = 0.12. The enhanced focusing observed at higher flow rates can be attributed to the enhanced inertial lift force (Eq. 2-1) and Dean drag force (Eq. 2-2) generated by the alternating sharp curvatures of the zigzag channel. The Dean drag force balances with the inertial lift force, guiding particles

toward equilibrium positions near the channel centerline and resulting in faster lateral migration and a narrower focusing bandwidth. These results highlight the critical role of flow conditions in achieving high focusing efficiency as previously reported in the literature [75].

5.2. Enrichment of particles and *E. coli*

To evaluate the enrichment performance of the optimized rigid zigzag microchannel, a flow rate of 50 μL/min, previously identified as optimal for focusing 1 μm particles, was used with both 1 μm particles and *E. coli* at a concentration of 2.5×10^5 /mL (Fig. 5-3). Fig. 5-3A compares the distribution of 1 μm particles and *E. coli* across the channel width at *Q* 50 μL/min. The enrichment of 1 μm particles and *E. coli* was further confirmed through image overlapping at the channel expansion zone and fluorescence images of outlet samples captured at 10x magnification (Figs. 5-3B-G), as described in section 3-4. For 1 μm particles, a fully focused stream was observed at the channel center with PC = 0.57 and FWHM = 0.12 (Fig 5-3B). Most of particles were collected from the middle outlet (Fig. 5-3C), with minimal presence in the side outlets (Fig. 5-3D). Similarly, *E. coli* formed a focused stream with PC = 0.55 and FWHM = 0.12 (Fig 5-3E), with the majority of cells recovered from the middle outlet (Fig. 5-3F) and a negligible number in the side outlets (Fig. 5-3G).

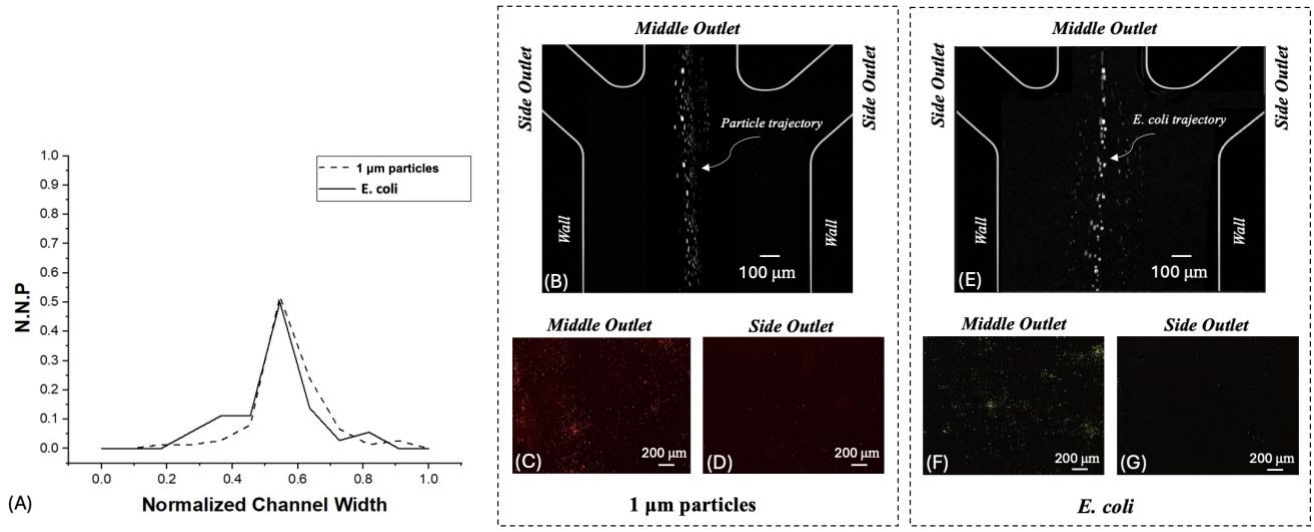

Figure 5-3 Enrichment of 1 µm particles and E. coli in rigid zigzag microchannels. (A) Distribution of 1 µm particles and E. coli bacteria across the channel width at Q = 50 µL/min. Trajectories and outlet samples fluorescent images of (B-D) 1 µm particles and (E-G) E. coli in zigzag microchannels at Q = 50 µL/min.

The slight difference in focusing performance between *E. coli* and the microparticles is primarily attributed to differences in shape and rigidity. While the microparticles are spherical and rigid, *E. coli* cells are rod-shaped and deformable, which influences their interaction with the flow. The quantification of *E. coli* enrichment is further explored in the following section.

5.3. Effect of bacteria concentration on enrichment

Under ideal focusing conditions, a single-pass operation is anticipated to enrich particles by approximately 3-factor (Eq. 1-1), based on the outlet geometry. A second-pass operation, applied to the enriched sample after one pass, is theoretically expected to achieve an overall enrichment factor of up to 9, assuming consistent recovery and focusing efficiency. To experimentally validate these expectations, the device was tested at a fixed flow rate of 50 µL/min, and the inlet and middle outlet concentrations were quantified using fluorometry, as detailed in the Methods section (Chapter 3). Testing was conducted across

a range of inlet *E. coli* concentrations, from 3.6×10^4 to 2.5×10^6 CFU/mL. This testing range was selected to cover concentrations below the fluorometer's detection threshold as well as the highest concentrations generally required for bacterial detection. The resulting enrichment factor versus the inlet concentration is shown in Fig. 5-4.

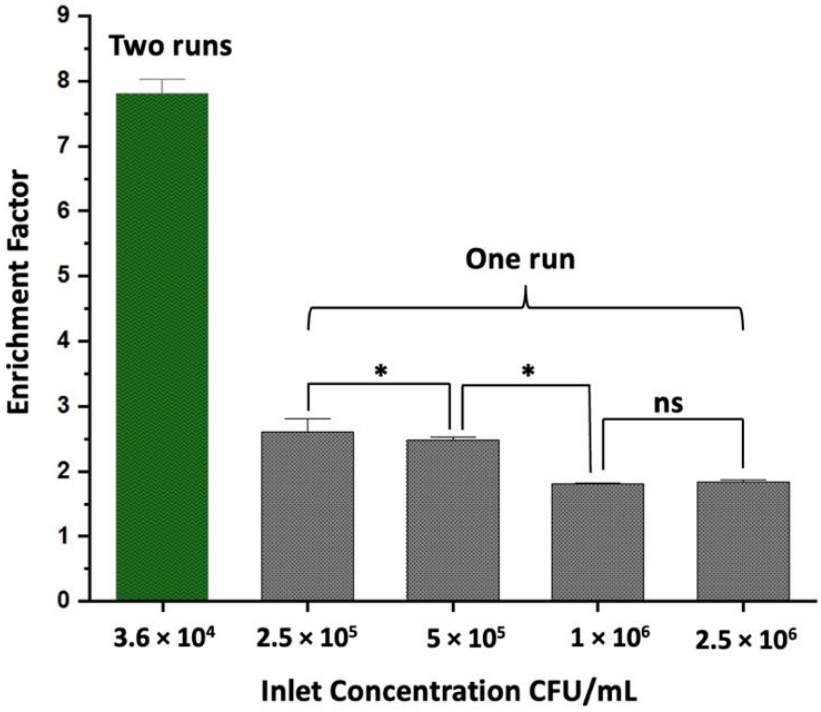

Figure 5-4 Enrichment factor of E. coli at various inlet concentrations. Error bars represent standard deviations calculated from three independent experimental repeats.: $p < 0.05$, ns: not significant.*

For single pass runs, the enrichment performance was evaluated across inlet concentrations ranging from 2.5×10^5 to 2.5×10^6 CFU/mL. At a concentration of 2.5×10^5 CFU/mL, an enrichment factor of approximately 2.6 ± 0.2 was achieved. As the inlet concentration increased to 1×10^6 CFU/mL, the enrichment factor decreased to around 1.81 ± 0.02, indicating slight reduced enrichment efficiency at higher bacterial concentrations. Further increasing the concentration to 2.5×10^6 CFU/mL resulted in a similar factor of

1.85 ± 0.03. This reduction in enrichment factor is potentially due to intensified particle-to-particle interactions at higher concentrations, which disrupt inertial focusing [13].

For the lowest inlet concentration of 3.6×10^4 CFU/mL, the first enrichment run could not be characterized due to concentration bacteria still falling below the detection limit of the fluorometer. Therefore, a second enrichment run was applied by reintroducing the the middle outlet sample collected from the first run back into the device. This approach substantially increased the enrichment factor to 7.8 ± 0.22, raising the concentration from 3.6×10^4 to approximately 2.9×10^5 CFU/mL, making the sample detectable by the fluorometer.

Generally, conventional methods and active microfluidic techniques can achieve enrichment factors of up to 1,000×; however, they often require bulky equipment, external fields, or complex instrumentation, which can limit portability and compatibility with downstream biological assays [76]. In contrast, our method offers moderate enrichment through a simple, passive, and label-free design. It effectively concentrates low-abundance samples to detectable levels, reaching concentrations $\geq 10^6$ CFU/mL, meeting the threshold set by regulatory agencies such as the Canadian Food Inspection Agency (CFIA). These features underscore its practical potential as a biocompatible preconcentration platform for point-of-care (PoC) diagnostics.

5.4. Viability of *E. coli* after enrichment

To assess the viability of *E. coli* following enrichment, samples with an initial concentration of 3.6×10^4 CFU/mL were passed twice through the device at a flow rate of 50 µL/min. The number of viable cells of the source, control, and enriched samples (middle outlet) were determined using plate counting, as shown in Fig. 5-5. The control sample was kept at room temperature during the enrichment process to confirm that any viability effects while increasing the concentration was

due to the microfluidic device rather than bacterial culturing. It is worth noting that recovery and viability are treated equivalently in this analysis, as the focusing results confirm that nearly all *E. coli* cells are directed to the middle outlet, with negligible loss to the side outlets.

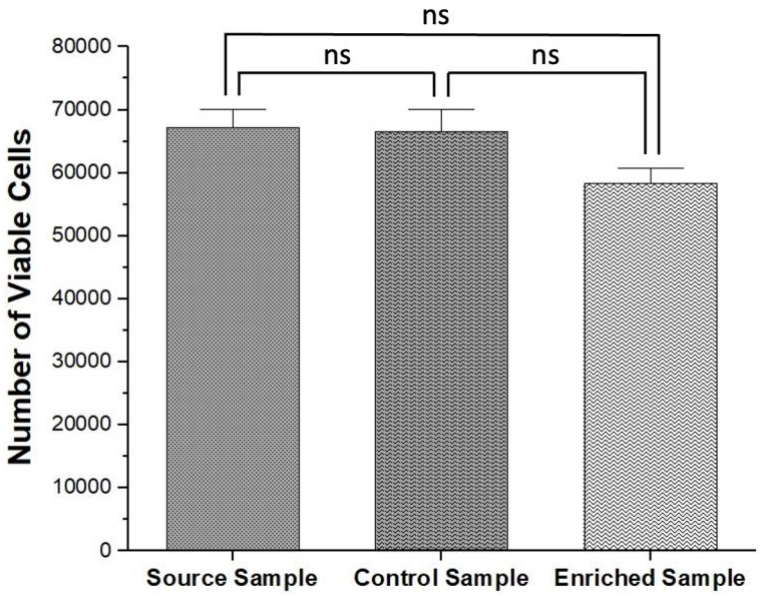

Figure 5-5 Number of viable E. coli cells after enrichment for the source, control, and enriched samples. Error bars represent standard deviations calculated from three independent experimental repeats. ns: not significant.

The source samples contained an average of 69,600 ± 3,746 cells in 1800 µL, while the control samples averaged 66,600 ± 4,762 cells, confirming over 95% viability, i.e., not statistically significant effect due to bacteria residing in the ambient environment. In contrast, the enriched samples yielded an average of 58,333 ± 2,323 CFU in 200 µL. These results correspond to an enrichment factor of 7.8 ± 0.22 and post-enrichment viability of approximately 84 ± 2.4% (Eq. 1-2), indicating high cell survival. The differences in the number of viable cells between the source, control, and enriched samples were not statistically significant ($p > 0.05$), suggesting that the enrichment process maintained bacterial viability. The slight reduction in cell viability in the

enriched sample accounts for potential cell loss within the microchannel and cell death during the enrichment process.

In comparison to the literature, our observed post-enrichment viability compares favorably with other reported microfluidic and conventional enrichment methods, which often exhibit significant viability loss due to high shear stress, electric fields, or acoustic heating; for instance, electrical and acoustophoretic systems have shown reduced viability due to electric field exposure or thermal dissipation effects [76]. By contrast, our device efficiently concentrates *E. coli* while preserving a high proportion of viable cells, making it suitable for downstream biological analysis and culture-based applications. This balance between efficient enrichment and cell survival highlights the strong potential of our device as a reliable preconcentration platform for point-of-care (PoC) applications.

Concluding Remarks

In this chapter, the enrichment of 1 μm particles and *E. coli* bacteria was demonstrated using rigid zigzag microchannels based on inertial focusing. The device achieved full focusing of 1 μm particles and *E. coli* at an optimal flow rate of 50 μL/min. Enrichment experiments showed that a single pass through the device yielded an enrichment factor of up to 2.6 ± 0.2, which increased to 7.8 ± 0.22 with two consecutive passes, effectively raising low-abundance bacterial concentrations to detectable levels ($\geq 10^6$ CFU/mL). Importantly, the device preserved high post-enrichment viability (~84 ± 2.4 %), outperforming several active methods that often compromise cell integrity due to exposure to external fields. Our passive, label-free approach offers a simpler, more portable, and biocompatible solution suitable for integration into point-of-care (PoC) diagnostic systems. Future work will focus on validating the device with real environmental and clinical samples to assess its practical applicability.

Chapter 6: Thesis Summary and Future Work

6.1. Thesis summary

The timely sample preparation, detection, and identification of microparticles and microorganisms play a critical role in medical diagnostics, environmental monitoring, food safety, and biotechnological applications. In particular, microplastics and pathogenic bacteria such as *Escherichia coli (E. coli)* have emerged as serious global health and environmental concerns due to their widespread presence and harmful effects. Enrichment (concentration enhancement) is often a required pre-processing step to increase the target concentration to detectable levels. While conventional enrichment methods such as centrifugation and filtration are effective, they are often time-consuming, equipment-intensive, and unsuitable for point-of-need (PoN) applications.

Microfluidics offers a promising alternative by enabling label-free, high-throughput, and miniaturized sample processing suitable for integration with downstream detection systems. Passive methods in microfluids rely on inherent particle and fluid properties, and they are favored due to their simplicity, cost-effectiveness, and compatibility with standard fabrication techniques. In general, zigzag channels with sharp corners outperform other designs in terms of particle separation and focusing capabilities due to the enhanced dean flow at the corners. Furthermore, there is a need to enhance the inertial focusing of 1 μm particles and *E. coli* as a biological application in rigid zigzag microchannels. Additionally, the numerical optimization of the zigzag channel parameters has not been previously explored. Finally, the quantitative enrichment of bacteria using inertial microfluidics remains uninvestigated.

This thesis presented a comprehensive investigation into the inertial focusing of micrometer-sized particles and *E. coli* within rigid zigzag microchannels, aiming to enhance sample preparation techniques for particle and bacterial enrichment. A summary of the main contributions of each chapter is provided below:

In Chapter 1, the motivation, research gaps, and objectives of the thesis were introduced. The chapter emphasized the need for improved sample handling techniques for micrometer particles and bacteria such as *E. coli*, which present increasing challenges in public health and environmental safety. It also highlighted the limitations of existing enrichment technologies and outlined the proposed approach using rigid zigzag microchannels.

Chapter 2 provided a comprehensive review of conventional and microfluidic-based enrichment methods. It covered the limitations of traditional techniques and discussed active and passive microfluidic methods, with particular emphasis on inertial focusing. Key theoretical concepts and

governing forces were introduced, followed by an overview of previous experimental and numerical studies on particle focusing.

Chapter 3 detailed the fabrication processes and experimental methodologies employed in this thesis. Soft lithography and hot embossing techniques were used to fabricate zigzag microchannels in PDMS and PMMA, respectively. The chapter also described the COMSOL Multiphysics model developed for numerical simulation, including the design of experiments (DOE) used for parameter exploration. Moreover, fluorescence-based quantification techniques for bacterial enrichment were also presented.

In chapter 4, the inertial focusing behavior of microparticles with diameters of 1, 2.7, and 3.9 μm was studied in rigid zigzag microchannels. The results clearly demonstrated that channel rigidity improves focusing performance, particularly at higher flow rates. The experimental results further revealed that particle size and flow velocity are key determinants of focusing quality. For instance, larger particles (e.g. 2.7 and 3.93 μm) achieved fully focusing behavior at an axial velocity of 0.37 m s^{-1}, while 1 μm particles and *E. coli* showed partial focusing behavior and required further optimization of the channel parameters. Building on these findings, a numerical parametric study was conducted using COMSOL Multiphysics, supported by the validation of the experimental results. A Taguchi Design of Experiments (DOE) method was used to systematically investigate the effect of key geometric and flow parameters such as zigzag length, number of zigzags, channel width, zigzag angle, and axial velocity on focusing efficiency. The Taguchi analysis revealed that increasing both number of zigzags and zigzag length significantly enhanced the focusing efficiency, exerting the most dominant influence among all parameters. In contrast, increasing the channel width and axial velocity disrupted the focusing behavior. A zigzag angle of 60° had the most effective focusing performance due to the enhanced dean flow at that angle.

The optimum zigzag channel parameters were identified as zigzag length = 3 mm, number of zigzags = 30, zigzag angle = 60°, with a channel cross section of $w \times h = 40 \times 20$ μm^2. Simulations revealed that under these conditions, focusing efficiency exceeded 80% for 1 μm particles at axial velocity = 0.37 m s^{-1}, aligning with the experimental validation of 1 μm and *E. coli* after optimization. This chapter confirmed that numerical optimization can effectively predict experimental results and identify high focusing efficiency channel designs.

Chapter 5 applied the optimized rigid zigzag microchannel to the enrichment of 1 μm particles *and E. coli*. The chapter began by confirming that 1 μm particles, used as surrogates for *E. coli*, exhibited fully focusing behavior at Q = 50 μL/min. Afterwards, enrichment experiments were then performed using GFP *E. coli* across a range of inlet concentrations form 3.6×10^4 to 2.5×10^6 CFU/mL at Q = 50 μL/min. The enrichment results demonstrated the strong potential of the optimized device for *E. coli* applications. A single pass through the microchannel yielded a notable enrichment factor of 2.6 ± 0.2, which increased to 7.8 ± 0.22 after two consecutive passes, highlighting the effectiveness of the device for enhancing bacterial concentration. Importantly, post-enrichment analysis showed that *E.coli* viability remained high, with approximately 84 ± 2.4% survival following the second enrichment run. These findings validate the device's capability to perform high-efficiency, label-free bacterial enrichment without compromising cell viability, reinforcing its suitability for point-of-need water quality monitoring and other bioanalytical applications.

6.2. Thesis limitations and proposed future work

While Chapter 5 successfully demonstrated the enrichment of *E. coli* using the optimized rigid zigzag microchannel, several limitations remain that should be addressed in future studies. A key

limitation is that all enrichment experiments were performed using deionized (DI) water under controlled laboratory conditions. Although this provided a reliable baseline to evaluate focusing and enrichment behavior, real water samples often contain particulates, organic matter, and chemical contaminants that could alter flow dynamics and particle–channel interactions. Future work should therefore focus on validating the device with environmental and clinical water samples, ultimately advancing its use as a portable point-of-need (PoN) diagnostic tool.

Another limitation lies in the scope of microorganisms tested. This study concentrated on *E. coli*, chosen as a representative bacterium due to its prevalence as a water quality indicator. However, the optimized zigzag microchannel could be further evaluated for other bacteria and pathogens within the 1–3 μm size range, including *Salmonella* and *Staphylococcus aureus (S. aureus)*. Broadening the range of test organisms would confirm the versatility of the device and enhance its relevance to diverse bioanalytical applications.

From a design perspective, the outlet configuration constrained the achievable enrichment factor, as the recovered bacterial samples were still collected in relatively large volumes. To overcome this, future studies could investigate outlet design modifications that enable recovery of bacteria in smaller collection volumes, thereby increasing the enrichment factor. Furthermore, the demonstrated increase in enrichment factor through multiple passes was limited by the need for manual reinjection, which is both time-consuming and labor-intensive. The development of a continuous-flow enrichment system with integrated recirculation could provide a scalable and time-efficient alternative, enabling higher enrichment factors without sacrificing throughput.

On the numerical side, since the zigzag microchannel was optimized specifically for the focusing of 1-3 μm particles, future numerical optimization can be extended to investigate the

focusing and enrichment of nanoparticles. This remains a significant challenge due to the dominant influence of Brownian motion at the nanoscale. Finally, the Dean drag velocity in zigzag microchannels can be systematically investigated through numerical simulations, enabling the development of a numerical correlation for the Dean drag velocity and the Dean drag force. Such correlations would improve the predictive accuracy of inertial focusing models, support the design of more efficient microfluidic devices, and provide a more comprehensive understanding of flow dynamics within zigzag channels.

References

[1] S. N. Zulkifli, H. A. Rahim, and W. J. Lau, “Detection of contaminants in water supply: A review on state-of-the-art monitoring technologies and their applications,” Feb. 01, 2018, *Elsevier B.V.* doi: 10.1016/j.snb.2017.09.078.

[2] J. Fan, L. Zou, T. Duan, L. Qin, Z. Qi, and Jiaoxia Sun, “Occurrence and distribution of microplastics in surface water and sediments in China’s inland water systems: A critical review,” *J Clean Prod*, vol. 331, p. 129968, Jan. 2022, doi: 10.1016/j.jclepro.2021.129968.

[3] M.-I. Mohammed and M. P. Y. Desmulliez, “Lab-on-a-chip based immunosensor principles and technologies for the detection of cardiac biomarkers: a review,” *Lab Chip*, vol. 11, no. 4, pp. 569–595, 2011, doi: 10.1039/C0LC00204F.

[4] Y. Shen, L. Xu, and Y. Li, “Biosensors for rapid detection of *Salmonella* in food: A review,” *Compr Rev Food Sci Food Saf*, vol. 20, no. 1, pp. 149–197, Jan. 2021, doi: 10.1111/1541-4337.12662.

[5] S. C. Hur, T. Z. Brinckerhoff, C. M. Walthers, J. C. Y. Dunn, and D. Di Carlo, “Label-Free Enrichment of Adrenal Cortical Progenitor Cells Using Inertial Microfluidics,” *PLoS One*, vol. 7, no. 10, Oct. 2012, doi: 10.1371/journal.pone.0046550.

[6] X. Zhao, C. W. Lin, J. Wang, and D. H. Oh, “Advances in rapid detection methods for foodborne pathogens,” 2014. doi: 10.4014/jmb.1310.10013.

[7] K. A. Stevens and L. A. Jaykus, “Bacterial separation and concentration from complex sample matrices: A review,” 2004. doi: 10.1080/10408410490266410.

[8] Y. Qu *et al.*, “SSEL, a selective enrichment broth for simultaneous growth of Salmonella enterica, Staphylococcus aureus, Escherichia coli O157: H7, and Listeria monocytogenes,” *J Food Saf*, vol. 40, no. 5, Oct. 2020, doi: 10.1111/jfs.12837.

[9] D. J. Wright, P. A. Chapman, and C. A. Siddons, “Immunomagnetic separation as a sensitive method for isolating Escherichia coli O157 from food samples,” *Epidemiol Infect*, vol. 113, no. 1, pp. 31–39, 1994, doi: 10.1017/S0950268800051438.

[10] T. Zhang *et al.*, “Microfluidic Separation and Enrichment of Escherichia coli by Size Using Viscoelastic Flows,” *Anal Chem*, vol. 95, no. 4, pp. 2561–2569, Jan. 2023, doi: 10.1021/acs.analchem.2c05084.

[11] J. Shrestha *et al.*, “Rapid separation of bacteria from primary nasal samples using inertial microfluidics,” *Lab Chip*, vol. 23, no. 1, pp. 146–156, Dec. 2022, doi: 10.1039/d2lc00794k.

[12] D. J. Beebe, G. A. Mensing, and G. M. Walker, “Physics and applications of microfluidics in biology,” 2002. doi: 10.1146/annurev.bioeng.4.112601.125916.

[13] L. Wang and D. S. Dandy, “High-Throughput Inertial Focusing of Micrometer- and Sub-Micrometer-Sized Particles Separation,” *Advanced Science*, vol. 4, no. 10, Oct. 2017, doi: 10.1002/advs.201700153.

[14] J. Zhang *et al.*, “Fundamentals and applications of inertial microfluidics: A review,” 2016, *Royal Society of Chemistry*. doi: 10.1039/c5lc01159k.

[15] Y. Gou, Y. Jia, P. Wang, and C. Sun, “Progress of inertial microfluidics in principle and application,” Jun. 01, 2018, *MDPI AG*. doi: 10.3390/s18061762.

[16] J. S. Kwon and J. H. Oh, “Microfluidic technology for cell manipulation,” Jun. 17, 2018, *MDPI AG*. doi: 10.3390/app8060992.

[17] S. Razavi Bazaz *et al.*, “Zigzag microchannel for rigid inertial separation and enrichment (Z-RISE) of cells and particles,” *Lab Chip*, vol. 22, no. 21, pp. 4093–4109, Sep. 2022, doi: 10.1039/d2lc00290f.

[18] D. Di Carlo, “Inertial microfluidics,” 2009, *Royal Society of Chemistry*. doi: 10.1039/b912547g.

[19] A. Nikdoost and P. Rezai, “Microparticle manipulation in viscoelastic flows inside curvilinear microchannels: a thorough fundamental study with application to simultaneous particle sorting and washing,” *New Journal of Chemistry*, vol. 47, no. 4, pp. 1635–1648, Nov. 2022, doi: 10.1039/d2nj05328d.

[20] A. Nikdoost and P. Rezai, “Dean flow velocity of viscoelastic fluids in curved microchannels,” *AIP Adv*, vol. 10, no. 8, Aug. 2020, doi: 10.1063/5.0019021.

[21] S. Shen *et al.*, “Spiral microchannel with ordered micro-obstacles for continuous and highly-efficient particle separation,” *Lab Chip*, vol. 17, no. 21, pp. 3578–3591, 2017, doi: 10.1039/C7LC00691H.

[22] S. Razavi Bazaz, A. Mashhadian, A. Ehsani, S. C. Saha, T. Krüger, and M. Ebrahimi Warkiani, “Computational inertial microfluidics: a review,” *Lab Chip*, vol. 20, no. 6, pp. 1023–1048, 2020, doi: 10.1039/C9LC01022J.

[23] M. Charjouei Moghadam, A. Eilaghi, and P. Rezai, “Inertia-magnetic particle sorting in microfluidic devices: a numerical parametric investigation,” *Microfluid Nanofluidics*, vol. 23, no. 12, Dec. 2019, doi: 10.1007/s10404-019-2301-3.

[24] M. Charjouei Moghadam, A. Eilaghi, and P. Rezai, “Elasto-inertial microparticle focusing in straight microchannels: A numerical parametric investigation,” *Physics of Fluids*, vol. 33, no. 9, Sep. 2021, doi: 10.1063/5.0060709.

[25] W. Pakhira, R. Kumar, and K. M. Ibrahimi, “Numerical Simulation of a Sheathless Multi-CTC Separator Lab-on-a-Chip Using Inertial Focusing Method,” *Comput Part Mech*, Oct. 2024, doi: 10.1007/s40571-024-00770-7.

[26] M. Nouri, P. Parvizian, A. Nikookalam, S. Seifi, and A. Shamloo, “A numerical study of Elasto-inertial particle-focusing in straight and serpentine microchannels,” *Results in Engineering*, vol. 23, Sep. 2024, doi: 10.1016/j.rineng.2024.102640.

[27] F. Amouzadeh, A. Ramiar, and N. Hedayati, “Investigation of a novel ‘cavity-added square wave’ microchannel for elasto-inertial focusing and negative magnetophoretic separation of particles,” *Advanced Powder Technology*, vol. 35, no. 4, Apr. 2024, doi: 10.1016/j.apt.2024.104374.

[28] R. Shi, “Numerical simulation of inertial microfluidics: a review,” 2023, *Taylor and Francis Ltd*. doi: 10.1080/19942060.2023.2177350.

[29] K. A. Stevens and L.-A. Jaykus, “Bacterial Separation and Concentration from Complex Sample Matrices: A Review,” *Crit Rev Microbiol*, vol. 30, no. 1, pp. 7–24, Jan. 2004, doi: 10.1080/10408410490266410.

[30] E. Dester and E. Alocilja, “Current Methods for Extraction and Concentration of Foodborne Bacteria with Glycan-Coated Magnetic Nanoparticles: A Review,” *Biosensors (Basel)*, vol. 12, no. 2, p. 112, Feb. 2022, doi: 10.3390/bios12020112.

[31] J. Ku, K. Wang, Q. Wang, and Z. Lei, “Application of Magnetic Separation Technology in Resource Utilization and Environmental Treatment,” *Separations*, vol. 11, no. 5, p. 130, Apr. 2024, doi: 10.3390/separations11050130.

[32] S. E. Philo *et al.*, “A comparison of SARS-CoV-2 wastewater concentration methods for environmental surveillance,” *Science of The Total Environment*, vol. 760, p. 144215, Mar. 2021, doi: 10.1016/j.scitotenv.2020.144215.

[33] E. Molina Grima, E.-H. Belarbi, F. G. Acién Fernández, A. Robles Medina, and Y. Chisti, “Recovery of microalgal biomass and metabolites: process options and

economics," *Biotechnol Adv*, vol. 20, no. 7–8, pp. 491–515, Jan. 2003, doi: 10.1016/S0734-9750(02)00050-2.

[34] N. Tien *et al.*, "Repeated centrifuging and washing concentrates bacterial samples in peritoneal dialysis for optimal culture: an original article," *BMC Microbiol*, vol. 20, no. 1, Dec. 2020, doi: 10.1186/s12866-020-02044-7.

[35] J. Yao, K. Zhao, J. Lou, and K. Zhang, "Recent Advances in Dielectrophoretic Manipulation and Separation of Microparticles and Biological Cells," *Biosensors (Basel)*, vol. 14, no. 9, p. 417, Aug. 2024, doi: 10.3390/bios14090417.

[36] S. Choe, B. Kim, and M. Kim, "Progress of Microfluidic Continuous Separation Techniques for Micro-/Nanoscale Bioparticles," *Biosensors (Basel)*, vol. 11, no. 11, p. 464, Nov. 2021, doi: 10.3390/bios11110464.

[37] Y. Xie *et al.*, "Microfluidic Isolation and Enrichment of Nanoparticles," *ACS Nano*, vol. 14, no. 12, pp. 16220–16240, Dec. 2020, doi: 10.1021/acsnano.0c06336.

[38] A. Rahmani, A. Mohammadi, and H. R. Kalhor, "A continuous flow microfluidic device based on contactless dielectrophoresis for bioparticles enrichment," *Electrophoresis*, vol. 39, no. 3, pp. 445–455, Feb. 2018, doi: 10.1002/elps.201700166.

[39] F. Hossein and P. Angeli, "A review of acoustofluidic separation of bioparticles," *Biophys Rev*, vol. 15, no. 6, pp. 2005–2025, Dec. 2023, doi: 10.1007/s12551-023-01112-2.

[40] M. S. Gerlt, P. Ruppen, M. Leuthner, S. Panke, and J. Dual, "Acoustofluidic medium exchange for preparation of electrocompetent bacteria using channel wall trapping," *Lab Chip*, vol. 21, no. 22, pp. 4487–4497, Nov. 2021, doi: 10.1039/d1lc00406a.

[41] T. P. Forbes and S. P. Forry, "Microfluidic magnetophoretic separations of immunomagnetically labeled rare mammalian cells," *Lab Chip*, vol. 12, no. 8, p. 1471, 2012, doi: 10.1039/c2lc40113d.

[42] A. Munaz, M. J. A. Shiddiky, and N.-T. Nguyen, "Recent advances and current challenges in magnetophoresis based micro magnetofluidics," *Biomicrofluidics*, vol. 12, no. 3, May 2018, doi: 10.1063/1.5035388.

[43] D. Rodoplu, C. S. Chang, C. Y. Kao, and C. H. Hsu, "A simple magnetic-assisted microfluidic method for rapid detection and phenotypic characterization of ultralow concentrations of bacteria," *Talanta*, vol. 230, Aug. 2021, doi: 10.1016/j.talanta.2021.122291.

[44] M. Yang *et al.*, “Optical sorting: past, present and future,” *Light Sci Appl*, vol. 14, no. 1, p. 103, Feb. 2025, doi: 10.1038/s41377-024-01734-5.

[45] T. Tsuji, Y. Matsumoto, R. Kugimiya, K. Doi, and S. Kawano, “Separation of Nano- and Microparticle Flows Using Thermophoresis in Branched Microfluidic Channels,” *Micromachines (Basel)*, vol. 10, no. 5, p. 321, May 2019, doi: 10.3390/mi10050321.

[46] J. Zhang *et al.*, “Fundamentals and applications of inertial microfluidics: A review,” 2016, *Royal Society of Chemistry*. doi: 10.1039/c5lc01159k.

[47] E. S. Asmolov, “The inertial lift on a spherical particle in a plane poiseuille flow at large channel Reynolds number,” *J Fluid Mech*, vol. 381, pp. 63–87, Feb. 1999, doi: 10.1017/S0022112098003474.

[48] A. J. Mach and D. di Carlo, “Continuous scalable blood filtration device using inertial microfluidics,” *Biotechnol Bioeng*, vol. 107, no. 2, pp. 302–311, Oct. 2010, doi: 10.1002/bit.22833.

[49] P. Mukherjee, X. Wang, J. Zhou, and I. Papautsky, “Single stream inertial focusing in low aspect-ratio triangular microchannels,” *Lab Chip*, vol. 19, no. 1, pp. 147–157, Jan. 2019, doi: 10.1039/c8lc00973b.

[50] D. Di Carlo, J. F. Edd, D. Irimia, R. G. Tompkins, and M. Toner, “Equilibrium separation and filtration of particles using differential inertial focusing,” *Anal Chem*, vol. 80, no. 6, pp. 2204–2211, Mar. 2008, doi: 10.1021/ac702283m.

[51] A. P. Sudarsan and V. M. Ugaz, “Multivortex micromixing,” 2006. [Online]. Available: www.pnas.orgcgidoi10.1073pnas.0507976103

[52] D. R. Gossett and D. Di Carlo, “Particle focusing mechanisms in curving confined flows,” *Anal Chem*, vol. 81, no. 20, pp. 8459–8465, Oct. 2009, doi: 10.1021/ac901306y.

[53] J. M. Martel and M. Toner, “Particle focusing in curved microfluidic channels,” *Sci Rep*, vol. 3, Nov. 2013, doi: 10.1038/srep03340.

[54] A. Özbey, M. Karimzadehkhouei, S. Akgönül, D. Gozuacik, and A. Koşar, “Inertial focusing of microparticles in curvilinear microchannels,” *Sci Rep*, vol. 6, Dec. 2016, doi: 10.1038/srep38809.

[55] A. Ozbey *et al.*, “Inertial focusing of cancer cell lines in curvilinear microchannels,” *Micro and Nano Engineering*, vol. 2, pp. 53–63, Mar. 2019, doi: 10.1016/j.mne.2019.01.002.

[56] B. H. Yang, J. Wang, D. D. Joseph, H. H. Hu, T. W. Pan, and R. Glowinski, “Migration of a sphere in tube flow,” *J Fluid Mech*, vol. 540, pp. 109–131, Oct. 2005, doi: 10.1017/S0022112005005677.

[57] J.-P. Matas, J. F. Morris, E. Guazzelli, and B. J. E, “Inertial migration of rigid spherical particles in Poiseuille flow,” *J Fluid Mech*, vol. 515, pp. 171–195, 2003, doi: 10.1017/S0022112004000254ï.

[58] A. A. S. Bhagat, S. S. Kuntaegowdanahalli, and I. Papautsky, “Continuous particle separation in spiral microchannels using dean flows and differential migration,” *Lab Chip*, vol. 8, no. 11, pp. 1906–1914, 2008, doi: 10.1039/b807107a.

[59] N. Modak, A. Datta, and R. Ganguly, “Cell separation in a microfluidic channel using magnetic microspheres,” *Microfluid Nanofluidics*, vol. 6, no. 5, pp. 647–660, May 2009, doi: 10.1007/s10404-008-0343-z.

[60] H. H. Hu and D. D. Joseph, “Direct Simulation of Initial Value Problems for the Motion of Solid Bodies in a Newtonian Fluid Part 1. Sedimentation,” *J Fluid Mech*, vol. 261, pp. 95–134, 1994, doi: 10.1017/S0022112094000285.

[61] J. Feng’, H. H. Huz A N, and D. D. D. Joseph’, “Direct simulation of initial value problems for the motion of solid bodies in a Newtonian fluid. Part 2. Couette and Poiseuille flows,” 1994.

[62] J. N. Krishnan, C. Kim, H. J. Park, J. Y. Kang, T. S. Kim, and S. K. Kim, “Rapid microfluidic separation of magnetic beads through dielectrophoresis and magnetophoresis,” *Electrophoresis*, vol. 30, no. 9, pp. 1457–1463, 2009, doi: 10.1002/elps.200800646.

[63] T. P. Forbes and S. P. Forry, “Microfluidic magnetophoretic separations of immunomagnetically labeled rare mammalian cells,” *Lab Chip*, vol. 12, no. 8, p. 1471, 2012, doi: 10.1039/c2lc40113d.

[64] C. Hale and J. Darabi, “Magnetophoretic-based microfluidic device for DNA isolation,” *Biomicrofluidics*, vol. 8, no. 4, Jul. 2014, doi: 10.1063/1.4893772.

[65] A. Al Amin, “HIGH THROUGHPUT PARTICLE SEPARATION USING DIFFERENTIAL FERMAT SPIRAL MICROCHANNEL WITH VARIABLE CHANNEL WIDTH,” 2014.

[66] H. Cha *et al.*, “Effects of obstacles on inertial focusing and separation in sinusoidal channels: An experimental and numerical study,” *Chem Eng Sci*, vol. 276, Jul. 2023, doi: 10.1016/j.ces.2023.118826.

[67] C. Parrott, “Computational Fluid Dynamics (CFD) Simulation of Microfluidic Focusing in a Low-Cost Flow Cytometer.”

[68] A. Khodayari, S. Ebrahimi, M. Topaheidari, and A. Shamloo, “High-Throughput Microfluidics for Precise Separation and Focusing of Circulating Tumor Cells with Optimized Triangular Microchannel Design,” *Talanta*, p. 128022, Mar. 2025, doi: 10.1016/j.talanta.2025.128022.

[69] Y. Ying and Y. Lin, “Inertial Focusing and Separation of Particles in Similar Curved Channels,” *Sci Rep*, vol. 9, no. 1, Dec. 2019, doi: 10.1038/s41598-019-52983-z.

[70] V. Kumar and P. Rezai, “Multiplex Inertio-Magnetic Fractionation (MIMF) of magnetic and non-magnetic microparticles in a microfluidic device,” *Microfluid Nanofluidics*, vol. 21, no. 5, May 2017, doi: 10.1007/s10404-017-1919-2.

[71] A. Nikdoost and P. Rezai, “Experimental investigation of microparticle focusing in SiO2 nanofluids inside curvilinear microchannels,” *Microfluid Nanofluidics*, vol. 28, no. 1, p. 5, Jan. 2024, doi: 10.1007/s10404-023-02700-0.

[72] B. P. Ho and L. G. Leal, “Migration of rigid spheres in a two-dimensional unidirectional shear flow of a second-order fluid,” *J Fluid Mech*, vol. 76, no. 4, pp. 783–799, 1976, doi: 10.1017/S002211207600089X.

[73] B. P. ho and L. G. Leal, “Inertial migration of rigid spheres in two-dimensional unidirectional flows,” *J Fluid Mech*, vol. 65, no. 2, pp. 365–400, 1974, doi: 10.1017/S0022112074001431.

[74] S. Narayana Iyengar, T. Kumar, G. Mårtensson, and A. Russom, “High resolution and rapid separation of bacteria from blood using elasto-inertial microfluidics,” *Electrophoresis*, vol. 42, no. 23, pp. 2538–2551, Dec. 2021, doi: 10.1002/elps.202100140.

[75] A. Refaei and Rezai Pouya, “Microparticles Focusing Inside Rigid Zigzag Microchannels and Application to Bacteria Enrichment,” *Submitted*, 2025.

[76] J. J. Ezenarro, J. Mas, X. Muñoz-Berbel, and N. Uria, “Advances in bacterial concentration methods and their integration in portable detection platforms: A review,” *Anal Chim Acta*, vol. 1209, May 2022, doi: 10.1016/j.aca.2021.339079.